Mathematical-Mechanical Model of WUF-B Connection Under Monotonic Load

HYUN CHANG YIM and TED KRAUTHAMMER

ABSTRACT

Connections in a steel frame are complex configurations composed of members and elements that contain different geometries, shapes and material properties. Therefore, one needs to take into account the contributions of such individual components to the overall connection behavior characteristics. This study presents a comprehensive mathematical-mechanical model to determine the welded unreinforced flange-bolted web (WUF-B) connection behavior. The model was developed considering nonlinear characteristics and coupling of individual component properties. The parameters in the mathematical expressions were derived based on collected data from numerical simulations, combined with modified and newly developed mechanical component equations. The models were evaluated by comparing them with finite element analysis results of nonlinear three-dimensional connections. The characterization models, (i.e., equations and procedures) introduced in this paper defined the mechanical properties of the WUF-B connections for a fast and accurate frame analysis of blast-oriented progressive collapse.

Keywords: welded unreinforced flange-bolted web connection, WUF-B, moment connections, mathematical modeling, finite element analysis.

Steel moment connections used in lateral load-resistant frames have shown a vulnerability to earthquakes, as observed in the Northridge earthquake (FEMA, 2000). The importance of beam to column connections was shown in progressive collapse studies (Krauthammer et al., 2004; Lim and Krauthammer, 2006). For relatively small local failures, strong connections enable the bridging of loads to undamaged structural columns. However, in the case of severe local damage by an abnormal load such as impact or blast, neighboring portions of the structure become unable to bridge the overloads and consecutive failures might be inevitable. Therefore, an accurate understanding of connection behavior is required for accurate progressive collapse analysis and to provide the necessary combination of ductility and strength in collapse-resistant frame design.

Considering the complexity of interactions between various parts in a connection, a finite element analysis (FEA) has been a viable approach for investigating such relationships.

However, fully dynamic nonlinear FEA require significant computational resources. Analyzing even a single connection would require a sufficiently dense mesh for all components (including also bolts, nuts, welds, etc.), representation of contacts between the components, and representation of their fully nonlinear dynamic behaviors. Furthermore, numerical analyses of a three-dimensional multi-story building will require even more computational resources to derive and collect the structural behavior data. For instance, there are approximately 500 connections in a 10-story building with a plan layout of four bays by four bays. The numerical analyses of the whole structural system would be prohibitively long and expensive. Hence, it is essential to find a fast but reliable approach to characterize the detailed assemblies and to apply the properties for the joints of a frame model.

Moment-rotation ($M - \theta$) curves have been generally used to characterize steel connections and to provide the properties of connector elements of a building frame model. Although, $M - \theta$ curves can be derived either theoretically or numerically, such curves were typically created based on experimental test results. Cyclic tests were performed to determine the welded-unreinforced flange-bolted-web connections (WUF-B) properties (Krawinkler et al., 1971; Engelhardt et al., 1992, 1994). Krawinkler et al. (1971) suggested a trilinear model of the shear moment versus rotation behavior of the panel zone. Mathematical models were proposed using extensive test results (Nethercot, 1985; Kishi and Chen, 1986). Empirical models for several partially restrained connections were also introduced based on the experimental results, applying constant derivation techniques, such as curve fitting and regression analysis (Kishi, 1994; Attiogbe and Morris, 1991). Mathematical expressions for the connection properties were derived for computational frame analysis.

Hyun Chang Yim, Ph.D., Senior Researcher, Research Institute of Industrial Science and Technology (RIST), 79-5 Youngcheon, Dongtang, Hwaseong Gyeonggi-do 445-813 South Korea (corresponding author). E-mail: hcyim@rist.re.kr

Ted Krauthammer, Ph.D., Goldsby Professor of Civil Engineering and Director of the Center for Infrastructure Protection and Physical Security (CIPPS), Department of Civil and Coastal Engineering, University of Florida, 365 Weil Hall, Gainesville, FL 32611. E-mail: tedk@ufl.edu

Accurate representations of the moment-rotation relationships must be addressed, especially for the prediction of overall frame performance. One of the most often used equations for mathematical representations of force-deformation (or stress-strain) for a given structural connection system is the Richard-Abbott model (Richard and Abbott, 1975). Mechanical models are represented by component approaches proposed in Eurocode 3 (European Prestandard, 1997). These spring models were established with a set of components (spring elements) that contain inelastic constitutive properties quantified individually. The spring components are arranged in series or in parallel, and the assemblage can generate appropriate $M - \theta$ curves. The arrangement of springs, deformation contribution, and capacity of the weakest spring determine the initial rotational stiffness and flexural resistance capacity. The effectiveness of this method has been demonstrated by numerous studies (European Prestandard, 1995; Faella et al., 2000; Tamboli, 1999; Ivany and Baniotopoulos, 2000; Tschemmernegg, 1988; Simoes da Silva et al., 2002; Rassati et al., 2004). Some of these studies dealt with the direct flange-to-flange welded joints.

The present study is aimed at characterizing the WUF-B connection behavior via mathematical and mechanical representations. The characterization equations and procedures introduced in this paper define the mechanical properties of the WUF-B connections for a fast and accurate analysis of progressive collapse that could occur after abnormal loading such as blast. If the connection properties are only determined through experimental tests and FEA simulations with detailed and complex modeling, then it would require significant time and effort to investigate the entire frame collapse. Methods using mechanical components (springs) were employed to determine the connection properties, and the component equations were either newly developed in this study or adopted from a previous study and then modified. The equations were used to determine specific parameters in the mathematical model. Based upon the finite element analyses of a full three-dimensional connection model, the developed methods were evaluated for their ability to simplify the feasible configurations for fast-running algorithms used in structural assessment. Furthermore, the modified approach led to a much simplified input for such analyses that are quite feasible even in a design office environment.

MATHEMATICAL MODEL OF NONLINEAR MOMENT-ROTATION CURVE

Richard and Abbott (1975) proposed a mathematical representation for the nonlinear structural systems. The equation has been implemented for the determination of various load-response relationships such as stress-strain, force-deflection, and moment-curvature curves. Using the Richard-Abbott model, the moment-rotation relationship of a steel connection can be expressed, as follows (Richard and Abbott, 1975):

$$M = \frac{\left(K_e - K_p\right)\theta}{\left(1 + \left|\frac{K_e - K_p}{M_o}\right|^n\right)^{1/n}} + K_p\theta \tag{1}$$

where

K_e = rotational elastic stiffness
K_p = plastic stiffness
M_o = reference moment, and
n = shape factor.

The shape factor may be obtained by a two-point analytical expression on the curve, (θ_a, M_a), (θ_b, M_b). The value for n is given by Equation (2), as follows:

$$A^n - \frac{1}{2^n}\left(B^n - 1\right) = 0 \tag{2}$$

where

$A = \dfrac{K_i}{\left(K_a - K_p\right)}$

$B = \dfrac{K_i}{\left(K_b - K_p\right)}$

$K_a = M_a/\theta_a$

$K_b = M_b/\theta_b$

The shape factor, n is then determined by iterations. Therefore, in order to predict a moment-rotation property of an arbitrary connection, one should define four important parameters: elastic stiffness, plastic stiffness, a reference moment, and a shape factor.

CHARACTERIZATIONS OF THE WUF-B CONNECTIONS

Before identifying the parameters, we classified the WUF-B connections into two different types depending on their force transfers (Carter, 2003). In the first case, the total design moment is less than the flexural strength of the girder. This case is generally found in the designs for buildings located in wind and low-seismic zones. Continuity plates and doubler plates are seldom embedded in the column panel zone. The tensile and compressive forces from the girder's top and bottom flanges are transferred through the complete-joint-penetration groove welds into the column flanges and spread into the web. Shear forces are transmitted through a fillet-welded single plate (shear tab) on the girder web into the column web. The rotational behavior of this kind of connection is mostly formed inside the panel zone by the axial and shear deformations of the column web. In the second case—connections designed for high seismic applications—most of the rotation occurs at the end of the girder because the higher strength of the panel zone restrains the deformation.

Subsequently, this induces larger deformations into the weak girder end. The strength enhancement in the panel zone is achieved by selecting a larger size of column or using continuity plates and doubler plates. Such enhancement can shift the plastic hinge location into the girder end, even when the transferred moment is equal to the full flexural strength of the girder. Therefore, the rotation angle should be carefully defined based on the ratio of panel zone strength to girder strength. This study provides the proper definitions of the rotations for these cases and evaluates them by comparing the relationships of moment-connection rotation and moment-girder tip displacements between detailed and simplified numerical models.

The WUF-B connections can be categorized into the aforementioned two groups using the AISC design guideline for stiffening of wide-flange columns (Carter, 2003). In this study, either of two categories is used: a weak panel zone-strong girder (WPZ-SG), or a strong panel zone-weak girder (SPZ-WG). Compressive and tensile forces equivalent to the girder flexural limit moment are determined, as follows:

$$P_u = M_u / h_t \tag{3}$$

where
P_u = tensile or compressive axial force through girder top or bottom flange
M_u = girder flexural strength
h_t = moment arm length

Continuity plates are required if the obtained forces are greater than one of the following resisting strengths (AISC, 2005):

Column flange bending (tension force only),

$$\phi R_n = 0.9\left(6.25 t_{fc}^2 F_{yc}\right) \tag{4}$$

Column web yielding (tension and compression forces),

$$\phi R_n = 1.0\left(5k + t_{fg}\right)F_{yc}t_{wc} \tag{5}$$

Column web crippling (compression force only),

$$\phi R_n = 0.75\left(0.8\right)t_{wc}{}^2 \left[1 + 3\left(N/d_c\right)\left(t_{wc}/t_{fc}\right)^2\right] \\ \times \sqrt{E\,F_{yc}\,t_{fc}\,/t_{wc}} \tag{6}$$

where
t_w = web thicknesses
t_f = flange thicknesses
d = depth of a member
F_y = yield strength
F_u = ultimate strength
E = modulus of elasticity
N = length of bearing
k = distance from outer face of flange to web toe of fillet weld

The subscripts c and g mean column and girder, respectively.

Meanwhile, a doubler plate is required if the transferred forces are greater than the column web shear strength, as follows:

$$\phi R_n = 0.9\left(0.6\right)F_{yc}d_c\,t_{wc} \text{ for } P_u = M_u/h_t < 0.4F_{yc}A_c \tag{7}$$

$$\phi R_n = 0.9\left(0.6\right)F_{yc}d_ct_{wc}\left(1.4 - P_u/F_{yc}A_c\right) \\ \text{for } P_u = M_u/h_t \geq 0.4F_{yc}A_c \tag{8}$$

The rotations of each group are defined, as illustrated in Figure 1. In the WPZ-SG connection, a rotating behavior is mostly observed in the panel zone, while the dominant

$$\theta_{WPZ-SG} = \theta_{girder}$$

(a) WPZ-SG connection

$$\theta_{SPZ-WG} = \theta_{girder} - \theta_{panel\ zone}$$
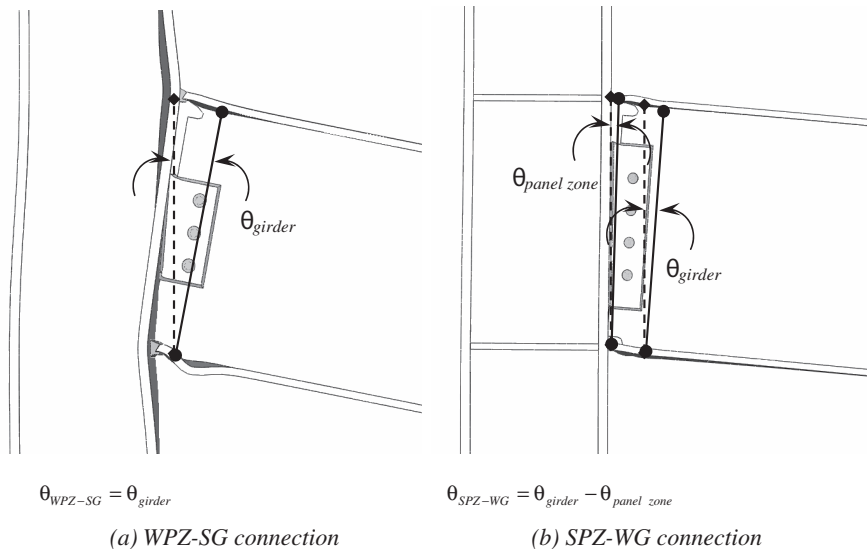
(b) SPZ-WG connection

Fig. 1. Definition of rotations.

angle in the SPZ-WG connection is from the girder. This fact is shown by comparing moment-girder tip displacement relationships obtained from detailed and simplified models, as shown in Figures 2(a) and 2(b), respectively. First, a connection model was built as detailed as possible; i.e., considering full three-dimensional behaviors, bolt-nut pre-loading, contacts, and material and geometrical non-linearity. These numerical studies used the finite element analysis program ABAQUS/Standard (Dassault Systems, 2008), and were validated in previous research (Yim and Krauthammer, 2009). Figure 3 indicate that the finite element models were successfully validated by comparison

(a) Detailed model
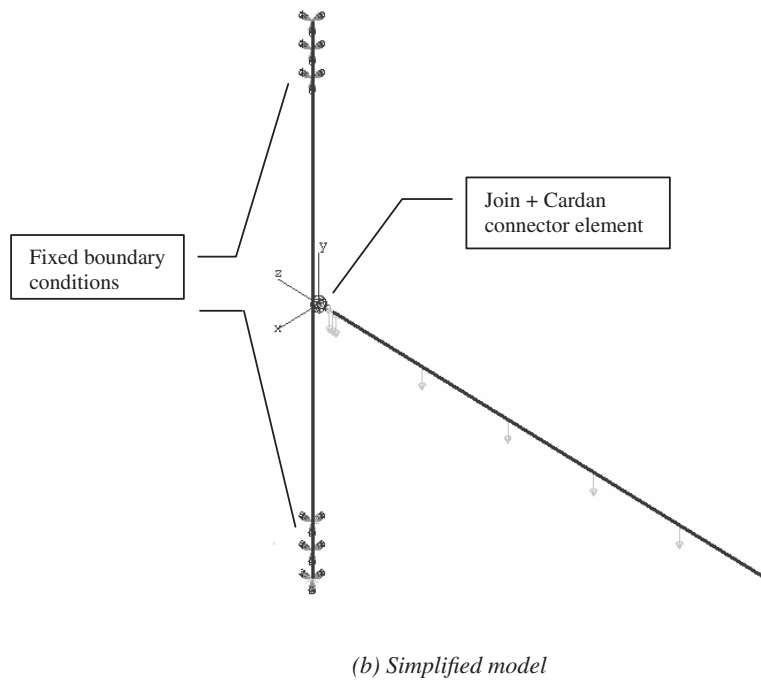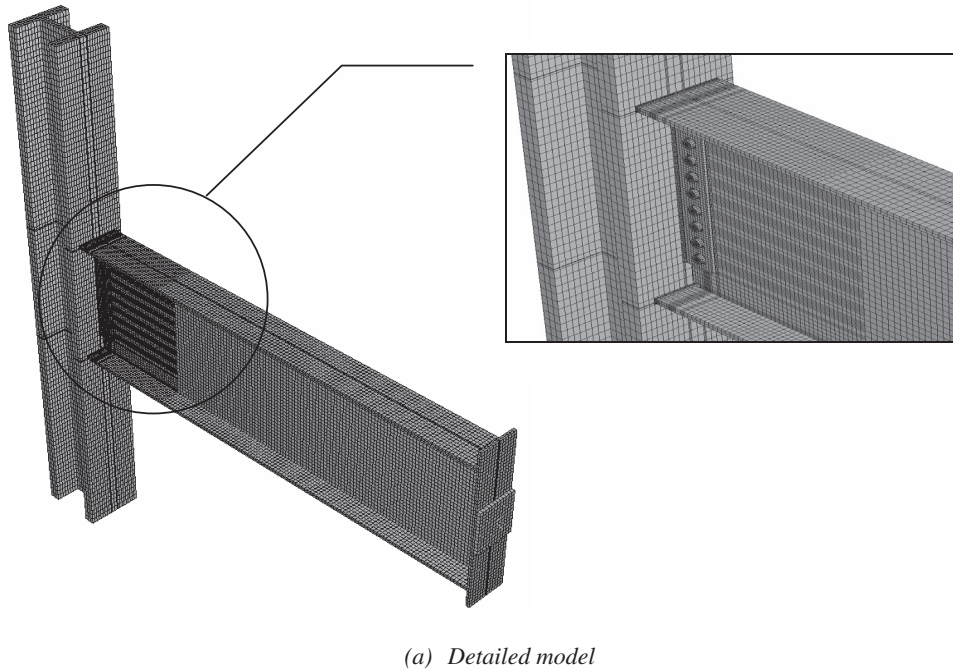
(b) Simplified model

Fig. 2. Detailed and simplified models.

with experimental data (Engelhardt and Sabol, 1994, for Case 16; Engelhardt and Husain, 1992, for Case 17 to Case 19; and Uang and Bondad, 1996, for Case 20). Based on the validated modeling techniques, push-down analyses where the static pressures were monotonically applied to the girders' top flange surfaces were conducted. The moment could be obtained by multiplying the applied pressures on the girder top flange by the lever arm lengths. The connection rotation was calculated from the displacements at the points close to the column flange and on the girder flanges (Figure 1), and the tip displacement was collected from the node of the girder tip in the neutral axis. Then, a finite element
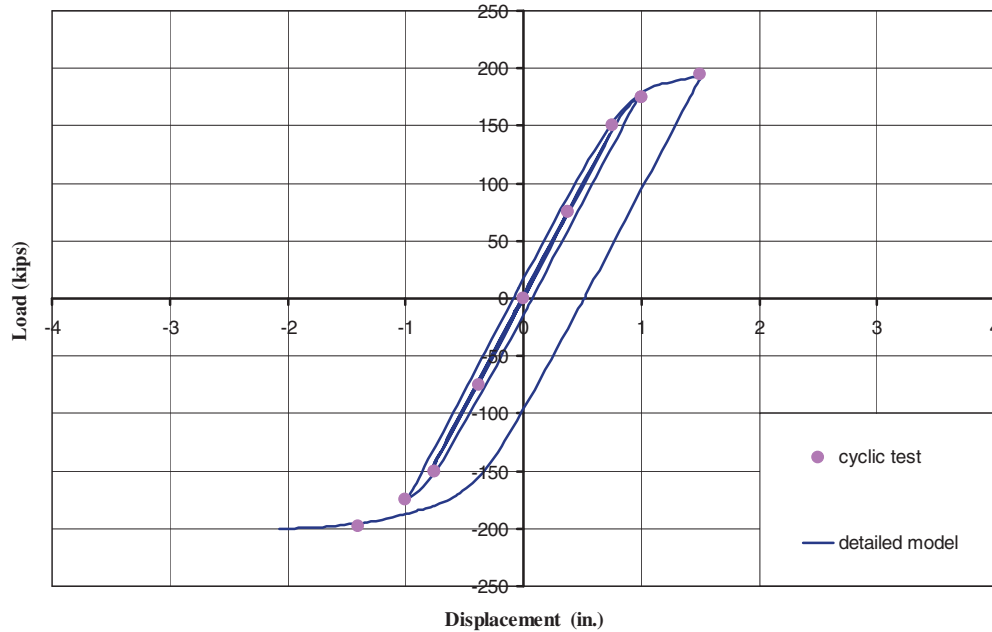
(a) Case 16 (Test result from Engelhardt and Sabol, 1994)
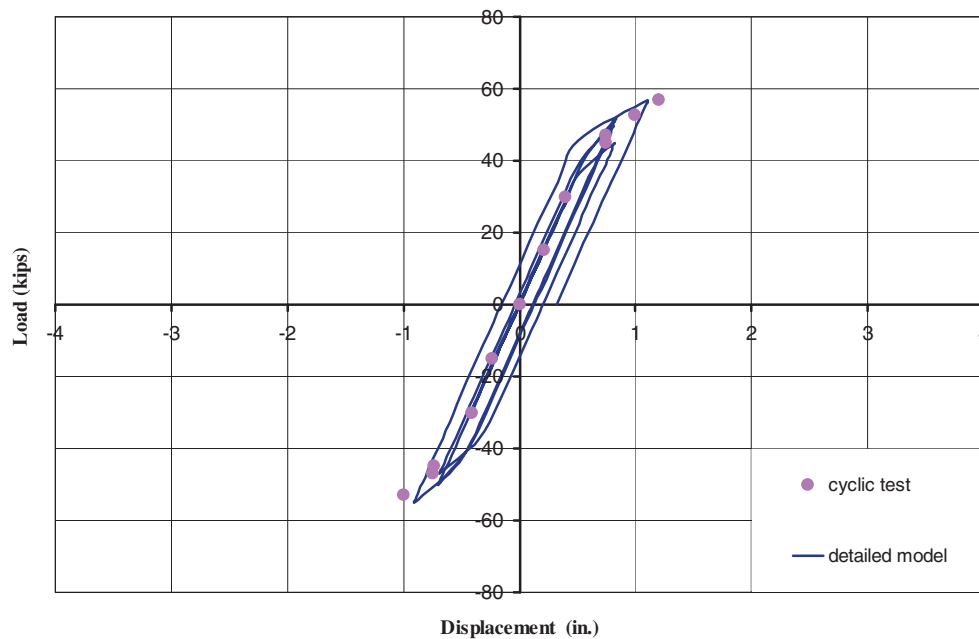
(b) Case 17 (Test result from Engelhardt and Husain, 1992)

Fig. 3. Result comparisons for model validation.

frame analysis was conducted with simpler beam elements and connector elements, as opposed to beam, column, and connection members modeled by 3D elements. All the same geometrical and material properties, boundary conditions, and loading, which had been adopted in the previous simulations for the detailed model, were applied into the simple frame analyses, as shown in Figure 2(b). The moment-rotation relationship extracted from the analysis with the

detailed model was utilized as a mechanical property of the connector element in the simplified frame analyses.

Figures 4 and 5 are comparisons of moment-rotation $(M - \theta)$ and moment-tip displacement $(M - \Delta)$ relationships for detailed and simplified models. According to the comparisons, the simple models using the $M - \theta$ properties for both WPZ-SG and SPZ-WG connections proposed in this study could produce the $M - \Delta$ responses, which were in
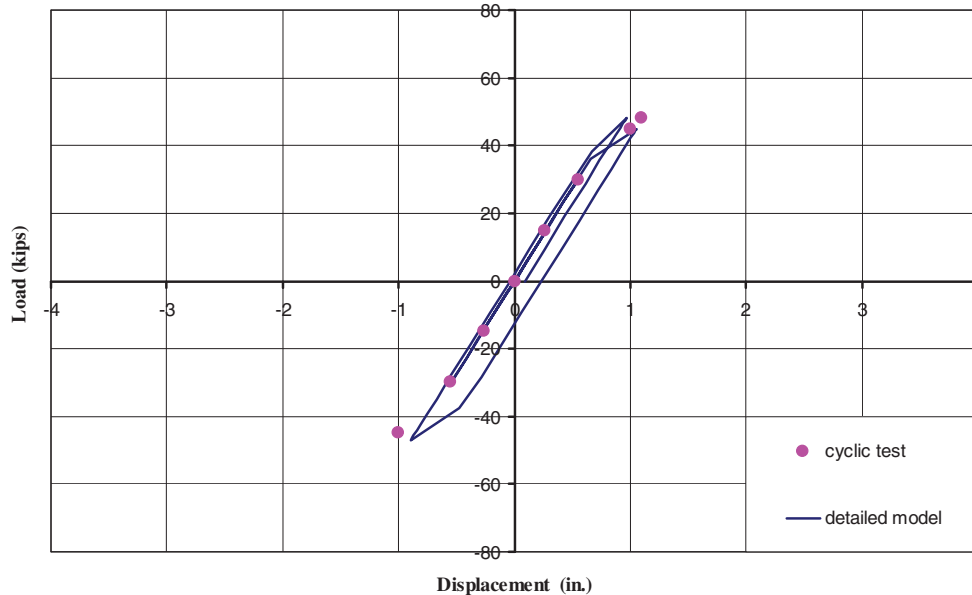
(c) Case 18 (Test result from Engelhardt and Husain, 1992)
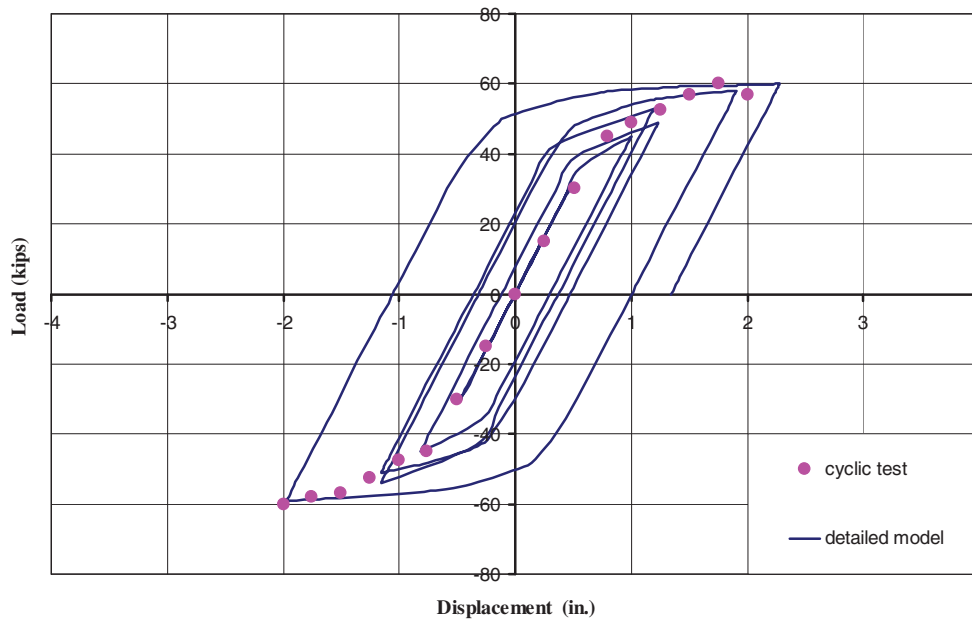
(d) Case 19 (Test result from Engelhardt and Husain, 1992)

Fig. 3. Result comparisons for model validation (continued).

Table 1. Number of Elements for Various Components (Case 16 in Table 3)		
Component	Number of Elements	
	Detailed Model	Simplified Model
Girder	21280	38
Column	39964	31
Bolts	6784	1 (Connector element)
Nuts	1024	
Shear Tabs	16680	
Welds	7158	
End Plate	176	

accord with the detailed model responses. Hence, it can be said that the rotations definition were accurate with respect to the specifically classified WUF-B connections.

In addition, it should be noted that the push-over simulations for the detailed models contained approximately 90,000 elements and required about 24 hours to run. The workstation had two Intel Xeon dual-core processors, operating at 3 GHz, and 3.5 GB of RAM for each CPU. The number of elements of individual members in the detailed and simplified models is defined in Table 1. The displacements from the simplified model were within 5 percent of the detailed model results and showed considerable savings in computation times and output file sizes (e.g., 12 hours run time and

1.20 GB of data, but less than 1 minute run time and 8 MB data for the simplified model). Hence, once the moment-rotation connection properties can be predicted mathematically and mechanically, the simplified models including these properties will be able to provide a good approximation of frame responses with very significant cost savings.

DERIVATION OF THE PARAMETERS IN THE MOMENT-ROTATION CURVES

In this study, the parameters of the mathematical representations were derived by means of a mechanical model, based on the Component Method (European Prestandard, 1997). In
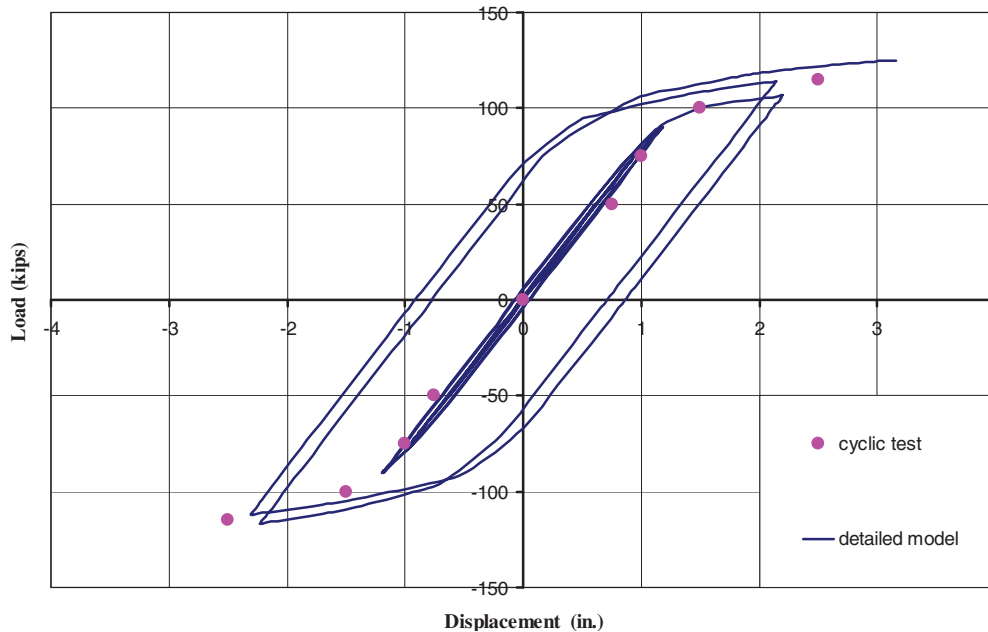
(e) Case 20 (Test result from Uang and Bondad, 1996)

Fig. 3. Result comparisons for model validation (continued).

particular, general approaches and terms presented in this study were adopted from previous research (e.g., Faella et al., 2000). One needs to modify the existing spring models or develop additional components (and those combinations), considering different force distributions in the unreinforced/reinforced panel zone to obtain more sophisticated $M - \theta$ curves.

The first step is the identification of the joint components. Seven basic components characterizing the WUF-B moment connection were considered (Figure 6): column web in shear (*cws*); column web in tension and compression (*cwt* and *cwc*); column flange in bending (*cfb*); girder flange in tension and compression (*gft* and *gfc*); and girder flange in tension/compression combined with shear tab in tension/compression (*gstab*).

As defined by Equation 1, the mathematical $M - \theta$ curve using the Richard-Abbott model is composed of the following four parameters: elastic and plastic stiffnesses, a reference moment, and a shape factor. The reference moment
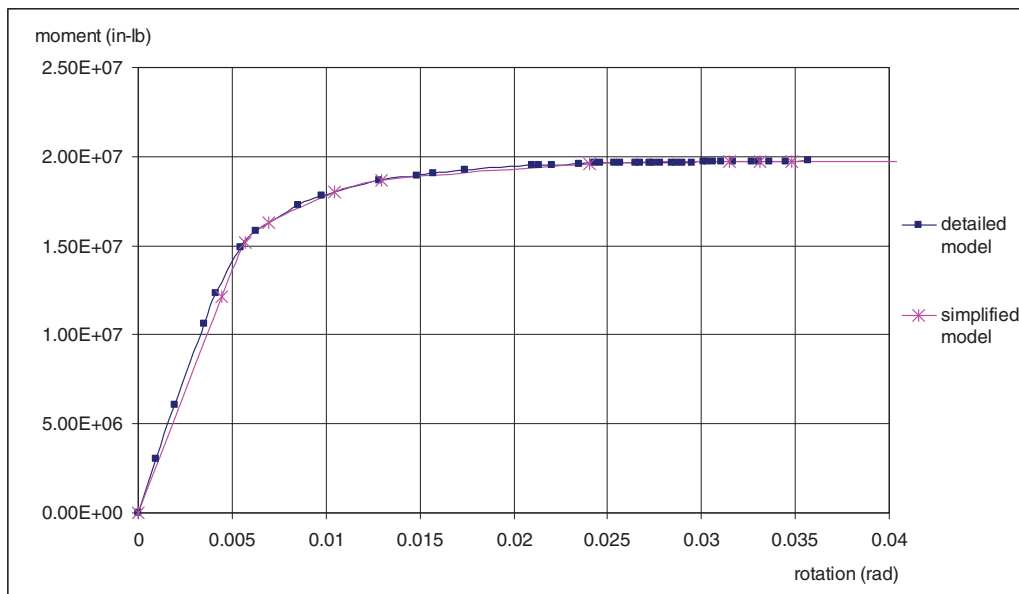
(a) Moment-rotation relationships
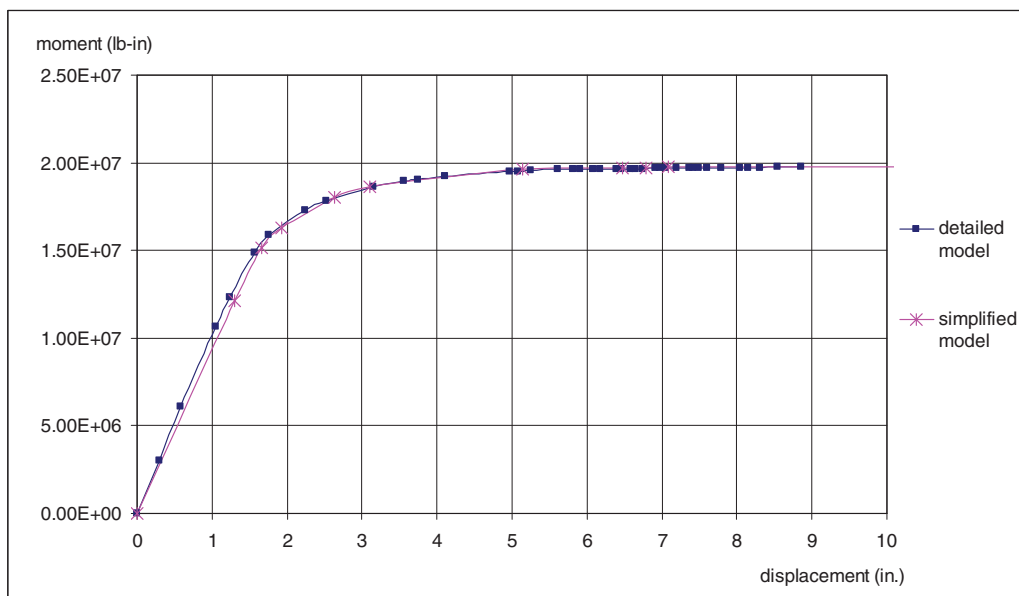
(b) Moment-tip displacement relationships

Fig. 4. WPZ-SG connection (Case 12 in Table 3).

and shape factor can be obtained using yield and ultimate moments. The governing components associated with each parameter are summarized in Table 2.

In the following sections, the component formulations and equation details are introduced in reference to each connection group. Procedures to extract the $M - \theta$ representations will then be presented. Finally, the reliability of the curve prediction will be discussed and demonstrated based on the comparisons with the simulation results.

Group 1: Weak Panel Zone-Strong Girder (WPZ-SG) WUF-B Connection

Elastic Stiffness

Components associated with the column web govern the elastic stiffness in this group. The stiffness component from the column web in shear can be obtained by the following fundamental moment-shear deformation relationship.
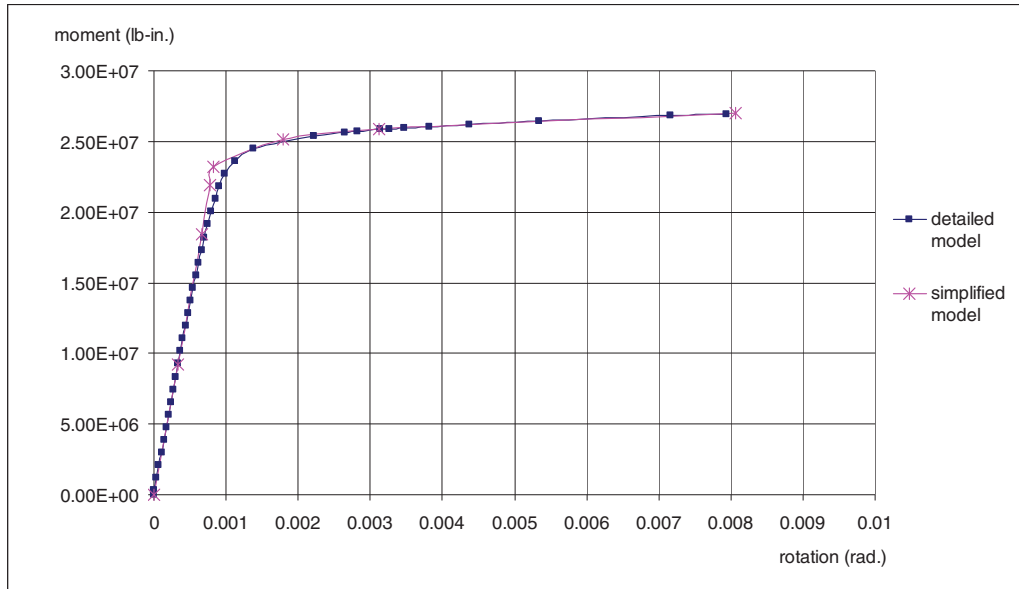
(a) Moment-rotation relationships
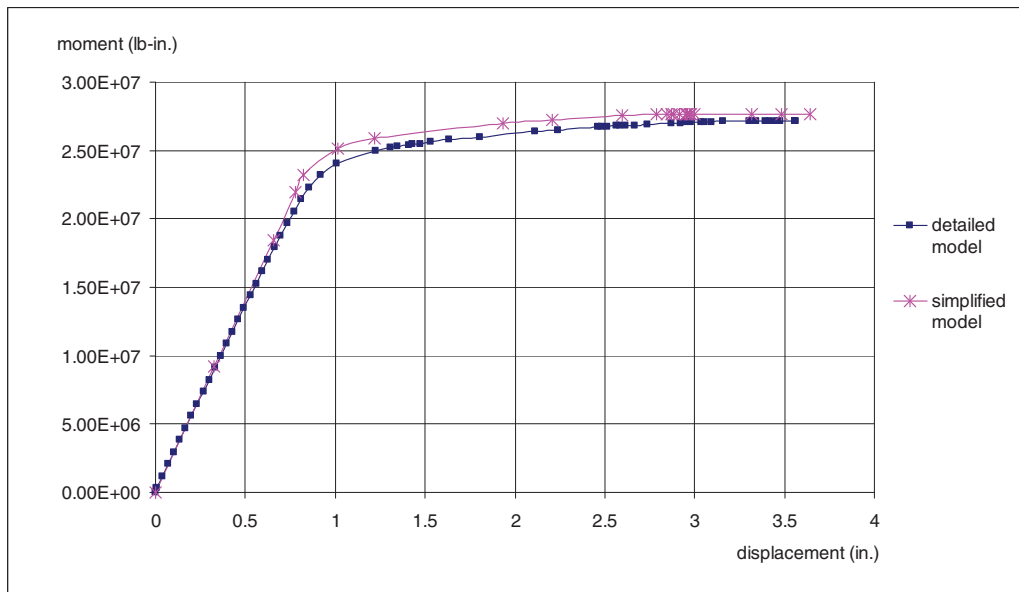
(b) Moment-tip displacement relationships

Fig. 5. SPZ-WG Connection (Case 16 in Table 3).

Parameters	Components	
	WPZ-SG connection	**SPZ-WG connection**
Elastic Stiffness	• column web in shear • column web in tension • column web in compression	• girder flange in tension • girder flange in compression
Yield Moment	• column web in shear • column web in tension • column web in compression • column flange in bending • girder flange in tension • girder flange in compression	• girder flange in tension • girder flange in compression
Plastic Stiffness	• girder web in tension • girder web in compression	• girder flange in tension • girder flange in compression
Ultimate Moment	• column web in tension or compression combined with shear tab force transfer • girder flange in tension/ compression, combined with shear tab in tension/ compression • groove weld failure	• girder flange in tension/ compression, combined with shear tab in tension/ compression • groove weld failure

Table 2. Component List for the Related Parameters
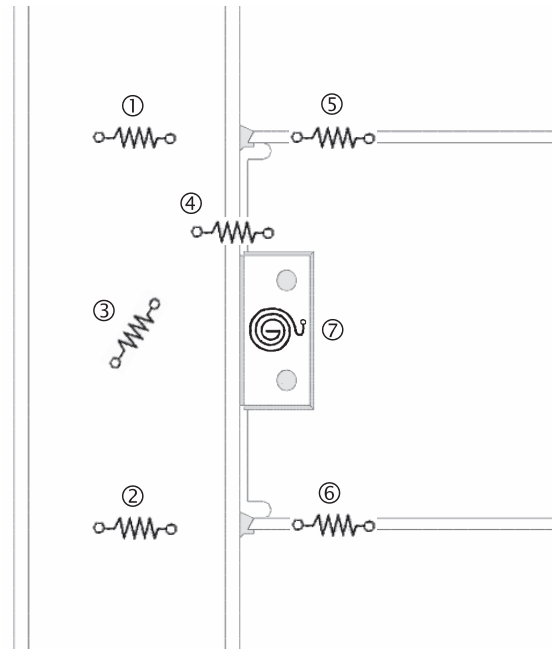
① column web in tension (*cwt*) ⑤ girder flange in tension (*gft*)

② column web in compression (*cwc*) ⑥ girder flange in compression (*gfc*)

③ column web in shear (*cws*) ⑦ shear tab in tension/compression (*gstab*)

④ column flange in bending (*cfb*)

Fig. 6. Components of WUF-B connection.

$$K_{cws} = \frac{GA_{vc}}{h_t} \quad (9)$$

The effective column web area is

$$A_{vc} = A_c - 2b_{fc}t_{fc} + \left(t_{wc} + 2r_c\right)t_{fc}$$

where

A_c = column area
r_c = radius of web-to-flange connection
G = shear modulus of elasticity

The stiffness characterized by the column web in tension and compression are identical, as shown in Equation 10,

$$K_{cwc} = K_{cwt} = \frac{Eb_{eff.cw}\,t_{wc}}{d_{wc}} \quad (10)$$

where

$b_{eff.cw}$ = effective width of the column web in tension and compression
d_{wc} = clear depth of the column web

The effective width $b_{eff.cw}$ is determined considering the action transmitted by the girder compressed flange, as shown in Equation 11 (European Prestandard, 1997):

$$b_{eff.cw} = t_{fg} + 2\sqrt{2}a_g + 5\left(t_{fc} + \sqrt{2}a_c\right) \quad (11)$$

where

t_{fg} = girder flange thickness
a_g = throat thicknesses of flange-to-web in girder
a_c = throat thicknesses of flange-to-web in column

One of the key features of the component method is the coupling of individual components. Since each component has an effect on the others during rotational behavior, a series formulation of the springs should be taken into account to define the constitutive model, as follows:

$$K_e = \frac{h_t^2}{\dfrac{1}{K_{cws}} + \dfrac{1}{K_{cwt}} + \dfrac{1}{K_{cwc}}} \quad (12)$$

Yield Moment

The flexural resistance can be determined from the weakest components, as expressed in Equation 13,

$$\begin{aligned} M_y &= F_{y\,\min}h_t \\ &= \min\left[F_{cws}, F_{cwc}, F_{cwt}, F_{cfb}, F_{gfc}, F_{gft}, F_{gfcb}\right] \cdot h_t \end{aligned} \quad (13)$$

First, the component strength in terms of column web in shear is given by Equation 14,

$$F_{cws} = \frac{f_{y\,pz}A_{vc}}{\sqrt{3}\,h_t\left(1 - h_t/L_c\right)} \quad (14)$$

where

$f_{y\,pz}$ = panel zone strength
L_c = column length

Next, the strength of the column web in compression is the minimum value of crushing or buckling resistance, as shown in Equation 15,

$$F_{cwc} = \min\left[F_{cwc\,crushing}, F_{cwc\,buckling}\right] \quad (15\text{-}1)$$

$$F_{cwc\,crushing} = b_{eff.cw}t_{wc}f_{y.cw} \quad (15\text{-}2)$$

The buckling resistance was determined by the use of the classical Winter formula (Faella et al., 2000). If the slenderness

$\bar{\lambda} = \left(\dfrac{b_{eff.cw}\,t_{wc}f_{y.cw}}{F_{cr}}\right)^{1/2}$ is greater than 0.67, where

$F_{cr} = \dfrac{\pi E t_{wc}^3}{3\left(1 - v^2\right)d_{wc}}$, then

$$F_{cwc\,buckling} = b^{*}_{eff.cwc}t_{wc}f_{y.cw}\frac{1}{\bar{\lambda}}\left(1 - \frac{0.22}{\bar{\lambda}}\right) \quad (15\text{-}3)$$

where

$$b^{*}_{eff.cwc} = t_{fb} + 2\left(t_{fc} + r_c\right)\left[\bar{\psi}\left(\frac{d_{wc}b_{fc}}{3t_{wc}t_{fc}}\right)^{1/4}\right]$$

= effective width for buckling resistance

$\bar{\psi}$ = reduction coefficient on the actual restraining action from column web

If $\bar{\lambda}$ is less than 0.67, $F_{cwc\,buckling} = F_{cwc\,crushing}$.

Equation 16 provides the load carrying capacity of the column web in tension,

$$F_{cwt} = b_{eff.cw}t_{wc}f_{y.cw} \quad (16)$$

Equation 17 can be used for flexural strength by means of a column flange in bending.

$$F_{cwc} = b_{eff.cfb}t_{fg}f_{y.gf} + \frac{t_{wg}d_{wg}f_{y.gw}}{4\left(h_g - t_{fg}\right)} \quad (17)$$

where

d_{wg} = clear depth of girder web
$f_{y\,gw}$ = yield strengths of girder web
$f_{y\,gf}$ = yield strengths of girder flange
$b_{eff.cfb} = t_{wc} + 2r_c + 7kt_{fc}$
= effective width for column flange bending
$k = \dfrac{f_{y.cf}t_{fc}}{f_{y.gf}t_{fg}}$ = coefficient

If the panel zone is relatively stronger than a portion of the girder, plastic behavior of connection initiates at the groove-welded girder flanges. Therefore, the resistance capacity of the girder flange is given by the following:

$$F_{gft} = F_{gfc} = \min\left[f_{cr\,gf}, f_{y\,gf}\right]b_{fg}t_{fg} \quad (18)$$

The $f_{cr\,gf}$ is the flange strength to resist local buckling defined as (AISC, 2005):

$$f_{cr\,gf} = \frac{k\pi^2 E}{12\left(1-\mu^2\right)\left[\dfrac{\left(b_{fg}/2\right)}{t_{fg}}\right]^2} \geq f_{y\,gf} \qquad (19)$$

where
  μ = Poisson's ratio
  k = constant depending on plate conditions (0.7 for flange)

Plastic Stiffness

Once yielding occurs in the panel zone before the girder end reach fully plastic condition, the girder flanges will contribute to the rotational plastic hardening behavior. Therefore,

$$K_{gft} = K_{gfc} = \frac{Eb_{fg}t_{fg}}{\rho b_{stab}} \qquad (20)$$

where
  ρ = coefficient
  b_{stab} = width of shear tab plate

If the panel zone reaches the ultimate condition, ρ is 1.0. When the ultimate stress is found at the girder flange zone, ρ is 1.5. Considering the series of springs and material hardening ratio, $\dfrac{E_h}{E}$, the plastic stiffness can be computed by Equation 21:

$$K_p = \frac{E_h}{E}\left(K_{eg}\right) = \frac{E_h}{E}\left(\frac{h_t^2}{\dfrac{1}{K_{gft}}+\dfrac{1}{K_{gfc}}}\right) \qquad (21)$$

Ultimate Moment

Ultimate flexural resistance can be obtained from the weakest component ultimate strength as expressed in Equation 22:

$$M_u = F_{u\,\min}h_t = \min\left[F_{cw\,stab}, F_{g\,stab}, F_{gweld}\right]h_t \qquad (22)$$

where
  $F_{cw\,stab}$ = force by the column web in compression or tension, adding the forces transferred through shear tab
  $F_{g\,stab}$ = force from the girder in tension/compression combined with shear tab force
  F_{gweld} = force by ultimate strength of groove weld between girder and column

The specific expressions are shown in Equations 23 and 24, respectively:

$$F_{cw\,stab} = t_{wc}f_{u.cw}\left[b_{eff.cwc}+\left(h_{stab}/2\right)^2\right] \qquad (23)$$

$$F_{g\,stab} = \left[f_{y\,gf}+\frac{\left(f_{u\,gf}-f_{y\,gf}\right)}{3}\right]b_{fc}t_{fc}h_t + \left[f_{u\,stab}\,t_{stab}\left(\frac{h_{stab}}{2}\right)^2\right] - \left(f_{u\,stab}-f_{y\,stab}\right)t_{stab}\left(\frac{h_{stab}^2}{8}\right)\right] \qquad (24)$$

where
  h_{stab} = height of shear tab plate
  t_{stab} = thickness of shear tab plate

Also,

$$F_{gweld} = f_{u\,gweld}b_{fg}\,t_{fg} \qquad (25)$$

where $f_{u\,gweld}$ is the ultimate strength of groove weld.

It should be noted that the ultimate moment is produced by means of interactions between the panel zone and the girder. In particular, it will be more complicated if the panel zone yields before the girder and the shear tab plate reaches its ultimate conditions. Therefore, in the WPZ-SG case, the ultimate and yield forces are assumed to be distributed in the shape of concave and convex ellipses on the cross sections on shear tab plates and girder flanges, respectively, as shown in Figure 7.

Strong Panel Zone-Weak Girder (SPZ-WG) WUF-B Connection

Elastic Stiffness

As a panel zone is made stronger by increasing column size or reinforcing, the rotation behavior becomes more concentrated at the girder region. Therefore, the stiffness is obtained on the basis of girder flanges in tension and compression, similar to the plastic hardening stiffness of a WPZ-SG connection. The initial stiffness is given by:

$$K_e = K_{eg} = \frac{h_t^2}{\dfrac{1}{K_{gft}}+\dfrac{1}{K_{gfc}}} \qquad (26)$$

where K_{gft} (equal to K_{gfc}) is the girder flange stiffness introduced in Equation 20. Because the ultimate stress occurs at the girder flange zone, ρ is assumed to be 1.5.

Yield Moment

Since the girder flange zone is weaker than the panel zone, the yield resistance of an SPZ-WG connection can be computed by Equation 18.

Plastic Stiffness

The plastic stiffness of an SPZ-WG case is identical to the WPZ-SG connection, where the ultimate stress is found in the girder flanges (Equation 21).

Ultimate Moment

The ultimate moment of an SPZ-WG connection can be obtained using the approach for a WPZ-SG connection, and the ultimate strength is found in the girder zone, as represented by Equation 24. As shown in Equation 27, the only difference is that the full ultimate stress was applied instead of the elliptical stress distribution. This is because one expects more contribution from the girder region in the case of the strong-panel zone connection.

$$F_{g\,stab} = f_{u\,gf}b_{fc}t_{fc}h_t + \left[f_{u\,stab}\,t_{stab}\left(\frac{h_{stab}}{2}\right)^2 \right.$$

$$\left. -\left(f_{u\,stab} - f_{y\,stab}\right)t_{stab}\left(\frac{h_{stab}^2}{8}\right)\right] \tag{27}$$

COMPARISONS WITH SIMULATION RESULTS

To show the accuracy of the mathematical-mechanical models, this study included extensive comparisons of the $M - \theta$ curves computed by the aforementioned approach with numerical analysis conducted by ABAQUS/Standard (Dassault Systems, 2008). Various girder-column candidates were employed or designed, as summarized in Table 3. For the WPZ-SG and WUF-B connections (from Cases 1 through 12), girder-column combinations and connections were employed from a building assumed to be located in a low-seismic zone, and the connections were designed on the basis of the pre-Northridge design concept. For the SPZ-WG cases, three connections were designed based on the AISC *Manual* (AISC, 2005). The column panel zones were reinforced by continuity plates and doubler plates. Cases 16 to 20 were obtained from seismic test studies (Engelhardt

and Husain, 1992; Engelhardt and Sabol, 1994; and Uang and Bondad, 1996). These eight SPZ-WG connections were designed to have highly stiff panel zones compared to the flexural strength of the joined girders.

The finite element models were established using ABAQUS/Standard, as shown in Figure 2. An elasto-plastic material property with isotropic hardening was selected to simulate the material behavior of all the components of the finite element model. The material models are shown in Table 4. An elastic modulus of 29,000 ksi, Poisson's ratio of 0.3, and ultimate strain of 0.2 were used for all cases. It should be noted that the girder and column properties of Cases 16 to 20 followed the mill certificate strength data reported on the experimental study (Engelhardt and Husain, 1992; Engelhardt and Sabol, 1994; and Uang and Bondad, 1996) while those of Cases 1 to 15 were constructed with ASTM A992 steel. Shear tabs of ASTM A36 steel, A325N bolts, and E70T-7 welds were used for all cases. The element types mainly used for the finite element models in this study were eight-node continuum (brick) elements with reduced integration (C3D8R). Six-node wedge elements (C3D6) were also used to model the curved parts that included the weld access holes, bolt holes and welds (Dassault Systems, 2008).

The numerical simulation results were compared with the results predicted by the proposed models. In Cases 1 through 4, the mechanical model results showed that both initial yield and ultimate moments were found in the panel zones, since the zones were weaker than girder region. Next, in Cases 5 to 8, it was shown that the yield moment occurs in the panel zones first, but the ultimate moment occurs at the girders. In Cases 9 to 12, both yield and ultimate moments were obtained from the girder regions, even though some portion of the panel zones yielded. Meanwhile, as expected before, the rotations were governed by girder deformations

(a) Shear tab (elevation view)   (b) Girder flange (top view)
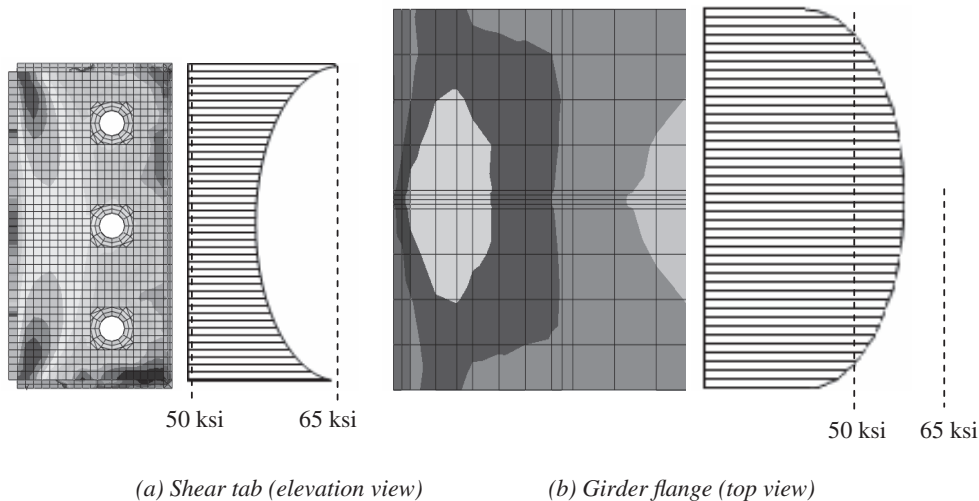
Fig. 7. Stress distributions on the shear tab and girder flange cross sections.

Table 3. Connection Cases																	
	No.	Girder	Column	Shear Tab Plate					Bolt			Weld		Continuity Plate			Doubler Plate	
				b_{stab}	h_{stab}	t_{stab}	L_{ev}	L_{eh}	ϕ	N_b	s	$t_{w\ stab-cflange}$	$t_{w\ stab-gweb}$	b_{stiff}	w_{stiff}	t_{stiff}	t_{dp}	$2-t_{dp}$
WPZ-SG	1	W21×62	W14×74	4½	9	5/16	1.5	1.5	¾	3	3	5/16	3/16	0	0	0	0	0
	2	W21×57	W14×99	4½	9	5/16	1.5	1.5	¾	3	3	5/16	3/16	0	0	0	0	0
	3	W27×94	W14×90	4½	15	5/16	1.5	1.5	¾	4	4	5/16	3/16	0	0	0	0	0
	4	W30×99	W14×90	4½	15	¼	1.5	1.5	¾	4	4	¼	¼	0	0	0	0	0
	5	W24×76	W14×120	4½	9	5/16	1.5	1.5	¾	3	3	5/16	3/16	0	0	0	0	0
	6	W27×94	W14×176	4½	15	5/16	1.5	1.5	¾	4	4	5/16	3/16	0	0	0	0	0
	7	W30×108	W14×132	4½	15	5/16	1.5	1.5	¾	4	4	5/16	¼	0	0	0	0	0
	8	W30×116	W14×159	4½	15	5/16	1.5	1.5	¾	4	4	5/16	¼	0	0	0	0	0
	9	W18×35	W14×74	4½	9	5/16	1.5	1.5	¾	3	3	5/16	3/16	0	0	0	0	0
	10	W18×35	W14×99	4½	9	5/16	1.5	1.5	¾	3	3	5/16	3/16	0	0	0	0	0
	11	W30×116	W14×233	4½	15	5/16	1.5	1.5	¾	4	4	5/16	¼	0	0	0	0	0
	12	W36×135	W14×283	4½	19	3/8	1.5	1.5	1	5	4	5/16	¼	0	0	0	0	0
SPZ-WG	13	W21×44	W12×53	3	12	¼	3	1.5	5/8	3	3	¼	3/16	4 3/16	11	7/16	1	½
	14	W24×62	W14×120	3	15	¼	3	1.5	5/8	4	3	5/16	3/16	7	12 5/8	9/16	1	½
	15	W24×68	W12×252	3	15	5/16	3	1.5	¾	4	3	5/16	¼	0	0	0	1	½
	16	W36×150	W14×455	5	25	5/8	1.5	1.5	1	8	3	5/16	¼	0	0	0	0	0
	17	W24×55	W12×136	4½	18	½	1.5	1.5	7/8	6	3	5/16	0	5¾	10 7/8	½	0	0
	18	W18×60	W12×136	4½	12	½	1.5	1.5	7/8	4	3	5/16	0	5¾	10 7/8	½	0	0
	19	W21×57	W12×136	4½	15	½	1.5	1.5	7/8	5	3	5/16	0	5¾	10 7/8	½	0	0
	20	W30×99	W14×176	4½	24	5/8	1.5	1.5	7/8	8	3	5/16	5/16	7 7/16	12 9/16	3/8	0	0

b_{stab} = width of shear tab plate (in.)
h_{stab} = height of shear tab plate (in.)
t_{stab} = thickness of shear tab plate (in.)
L_{ev} = vertical length from edge to first bolt hole (in.)
L_{eh} = horizontal length from edge to first bolt hole (in.)
ϕ = bolt diameter (in.)
N_b = number of bolts
s = bolt spacing (in.)

$t_{w\ stab-cflange}$ = thickness of weld between shear tab plate and column flange (in.)
$t_{w\ stab-gweb}$ = thickness of weld between shear tab plate and girder web (in.)
b_{stiff} = length of continuity plate (in.)
w_{stiff} = width of continuity plate (in.)
t_{stiff} = thickness of continuity plate (in.)
t_{dp} = thickness of doubler plate (in.)

in the SPZ-WG connections (Cases 13 to 16). Table 5 summarizes the overall results from simulations and mechanical representations.

Once the yield or ultimate moments and elastic or plastic stiffnesses are computed, the next step was to generate the parameters for the mathematical representations (Equation 1). The required parameters, θ_a, M_a, θ_b, M_b, M_o and n are defined by Equations 28-1 through 28-5. The shape factor n is then determined through iteration, as defined by Equation 2.

$$M_a = M_y \qquad (28\text{-}1)$$

$$\theta_a = \theta_y = M_y/K_e \qquad (28\text{-}2)$$

$$M_0 = M_y + \frac{\eta}{3}\left(M_u - M_y\right) \qquad (28\text{-}3)$$

$$\theta_b = 2\theta_a \qquad (28\text{-}4)$$

$$M_b = M_y + \left(M_u - M_y\right)\left(\frac{\theta_b - \theta_a}{\theta_u - \theta_y}\right) \qquad (28\text{-}5)$$

where $\eta = 1$ if the beam web supplemental weld is not provided and $\eta = 2$ if such a weld is provided.

Table 4. Connection Component Yield and Ultimate Strengths						
Case	Strength	Girder	Column	Shear Tabs	Bolt/Nut	Weld
1-15	f_y (ksi)	50.0/50.0	50.0/50.0	36.0	92.0	70.0
	f_u (ksi)	65.0/65.0	65.0/65.0	58.0	120.0	80.0
16[a]	f_y (ksi)	50.0/50.0	62.5/62.5	50.0	92.0	70.0
	f_u (ksi)	64.8/64.8	78.9/78.9	64.8	120.0	80.0
17[b]	f_y (ksi)	41.6/42.3	52.0/54.9	36.0	92.0	58.0
	f_u (ksi)	59.6/63.9	70.4/73.7	58.0	120.0	70.0
18[b]	f_y (ksi)	40.9/43.0	52.0/54.9	36.0	92.0	58.0
	f_u (ksi)	59.9/59.9	70.4/73.7	58.0	120.0	70.0
19[b]	f_y (ksi)	38.4/36.5	52.0/54.9	36.0	92.0	58.0
	f_u (ksi)	56.1/54.7	70.4/73.7	58.0	120.0	70.0
20[c]	f_y (ksi)	46.5/57.1	52.5/51.2	36.0	92.0	58.0
	f_u (ksi)	67.7/72.5	68.2/67.2	58.0	120.0	70.0

[a] Engelhardt and Sabol, 1994
[b] Engelhardt and Husain, 1992
[c] Uang and Bondad, 1996

Table 5. Results from Mathematical-Mechanical Models and Simulations									
	No.	K_e (in.-lb-rad)		M_y (in.-lb)		K_p (in.-lb-rad)		M_u (in.-lb)	
		Simulation	Math.-Mech.	Simulation	Math.-Mech.	Simulation	Math.-Mech.	Simulation	Math.-Mech.
WPZ-SG	1	5.92E+08	6.71E+08	3.34E+06	2.57E+06	1.50E+07	1.85E+07	4.78E+06	5.08E+06
	2	7.40E+08	7.23E+08	3.32E+06	2.96E+06	1.30E+07	1.57E+07	5.46E+06	5.18E+06
	3	2.76E+10	2.67E+10	4.81E+06	3.29E+06	4.56E+07	4.48E+07	6.85E+06	6.36E+06
	4	1.04E+09	1.09E+09	5.05E+06	3.60E+06	4.58E+07	5.22E+07	7.61E+06	7.47E+06
	5	1.10E+09	1.14E+09	3.64E+06	4.65E+06	3.06E+07	1.94E+07	7.82E+06	8.11E+06
	6	1.68E+09	2.12E+09	9.36E+06	9.45E+06	3.25E+07	2.99E+07	1.22E+07	1.12E+07
	7	1.67E+09	1.79E+09	6.38E+06	6.86E+06	4.33E+07	3.95E+07	1.27E+07	1.36E+07
	8	1.91E+09	2.15E+09	8.50E+06	8.92E+06	5.49E+07	4.45E+07	1.56E+07	1.51E+07
	9	4.78E+08	5.10E+08	2.13E+06	2.13E+06	5.66E+06	4.46E+06	2.82E+06	2.76E+06
	10	5.27E+08	5.46E+08	2.13E+06	2.20E+06	5.06E+06	4.46E+06	2.82E+06	2.76E+06
	11	2.54E+09	3.49E+09	1.26E+07	1.30E+07	3.43E+07	4.45E+07	1.55E+07	1.51E+07
	12	3.84E+09	5.58E+09	1.63E+07	1.65E+07	5.54E+07	6.74E+07	1.97E+07	1.95E+07
SPZ-WG	13	5.36E+09	5.80E+09	3.55E+06	2.96E+06	1.06E+07	1.58E+07	3.97E+06	4.27E+06
	14	9.10E+09	1.07E+10	5.16E+06	4.80E+06	2.26E+07	2.93E+07	5.94E+06	6.90E+06
	15	1.21E+10	1.36E+10	6.99E+06	6.06E+06	4.43E+07	3.70E+07	8.27E+06	8.71E+06
	16	2.76E+10	2.67E+10	2.32E+07	1.97E+07	1.38E+08	1.09E+08	2.94E+07	3.12E+07
	17	5.98E+09	4.06E+09	3.42E+06	2.94E+06	1.05E+08	1.01E+08	5.64E+07	5.85E+06
	18	4.36E+09	3.46E+09	3.42E+06	3.31E+06	9.34E+07	9.93E+07	5.69E+06	5.44E+06
	19	3.90E+09	3.83E+09	3.71E+06	3.14E+06	1.14E+08	9.88E+07	5.91E+06	6.12E+06
	20	1.41E+09	1.27E+10	1.19E+07	8.91E+06	1.20E+08	9.37E+07	1.50E+07	1.67E+07

Finally, the $M - \theta$ curves are derived and compared with the curves extracted from the simulations. The comparisons in Figures 8 demonstrate that the theoretical curves were in quite good agreement with those from the finite element analyses.

DISCUSSION

The Richard-Abbott model could be used to describe a nonlinear behavioral model for a moment connection using mechanical parameters and a shape factor. The strong point of the model is that it produces the nonlinear curves if points are defined before and after the point of inflection (i.e., before the curve between proportional limit and strain hardening). The points before the inflection were accurately determined by the initial stiffness and yield strength formulations given in

this study. The connection yielding started at the panel zones in Cases 1 through 8 while the girder regions yielded first in Cases 9 to 20, due to the relatively stronger panel zones that moved the yield initiations into the girder regions. The simulation results for Cases 5 to 8 showed that the yielding initiated in the panel zones, but the girders reached the ultimate conditions earlier. This can happen because the panel zones are the stiffened regions, and they may resist the loads until the unstiffened girder flanges reached ultimate stresses. Stress concentrations around the weld access holes caused the ultimate moment condition at the girder to be reached sooner. In Cases 9 to 12, both yield and ultimate moments were obtained in the girder regions, even though some portion of the panel zones yielded. Meanwhile, as expected, the rotations were governed by girder deformations for the SPZ-WG connections (Cases 13 to 20). The differences in results
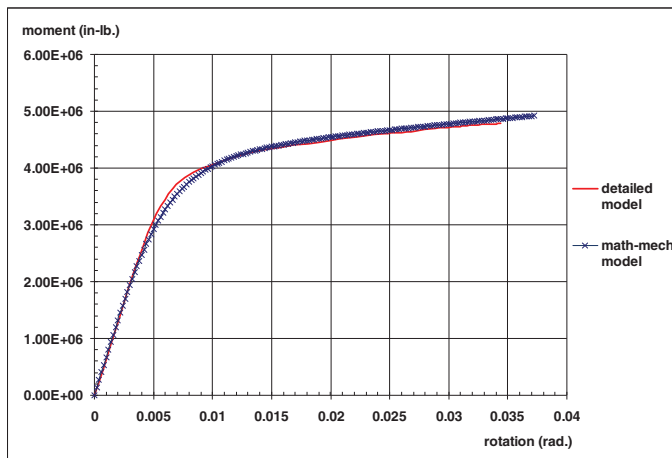
(a) Case 1
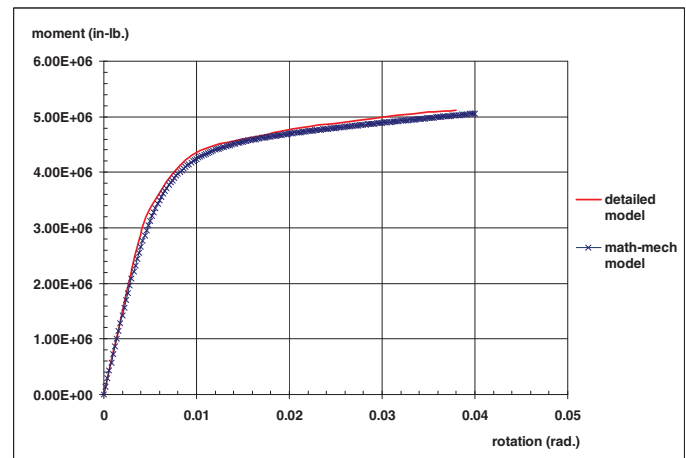
(b) Case 2
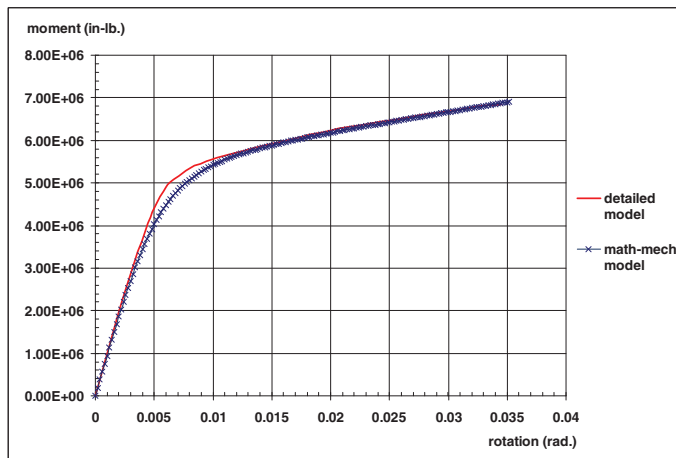
(c) Case 3
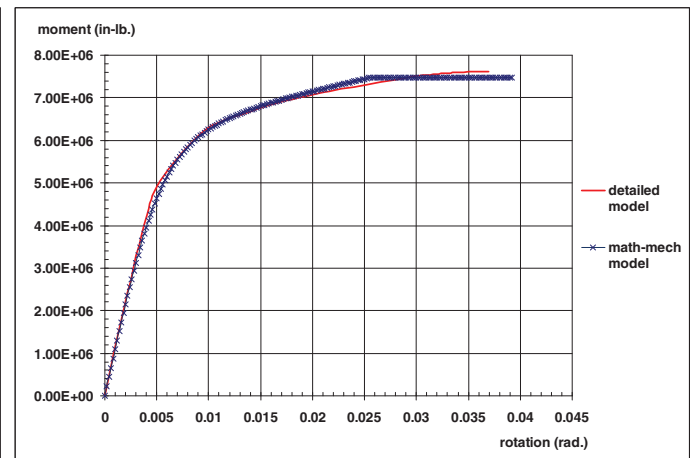
(d) Case 4

Fig. 8. Comparisons of the curves from mathematical-mechanical model with simulation results from detailed model.

(e) Case 5

(f) Case 6

(g) Case 7
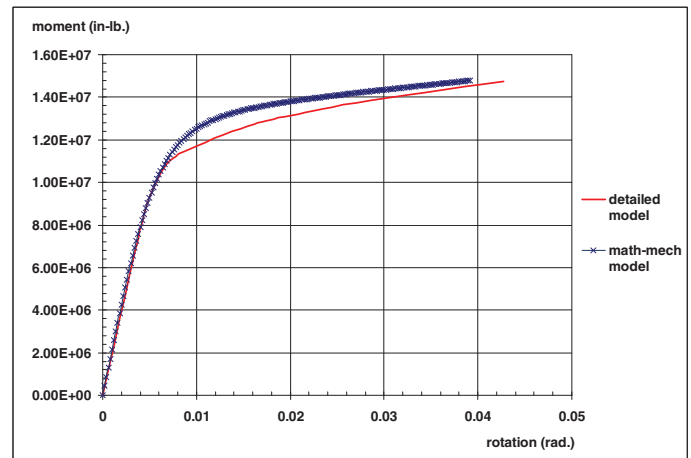
(h) Case 8
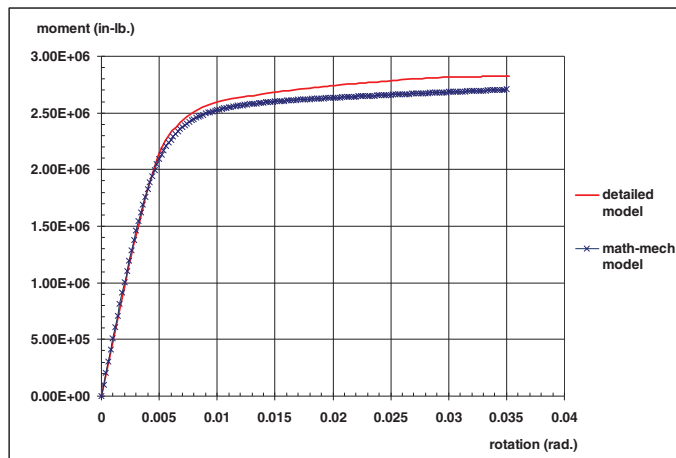
(i) Case 9
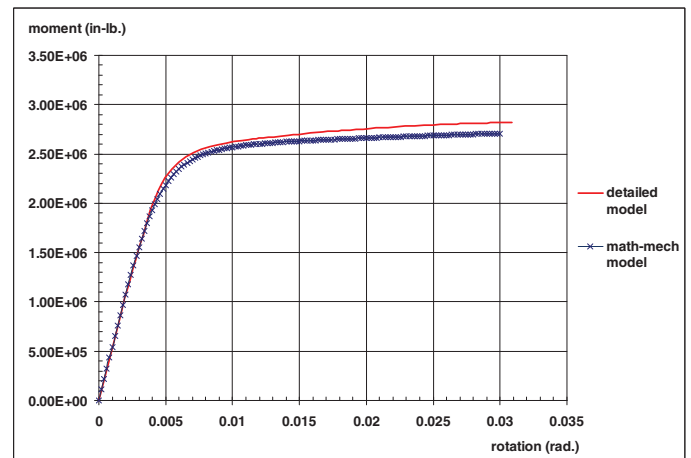
(j) Case 10

Fig. 8. Comparisons of the curves from mathematical-mechanical model with simulation results from detailed model (continued).
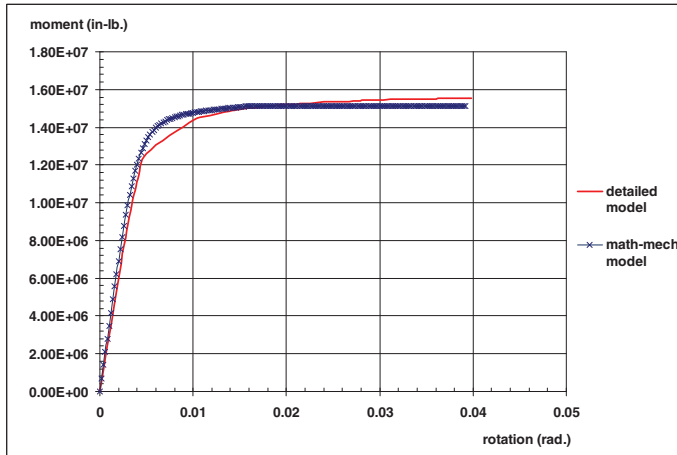
(k) Case 11
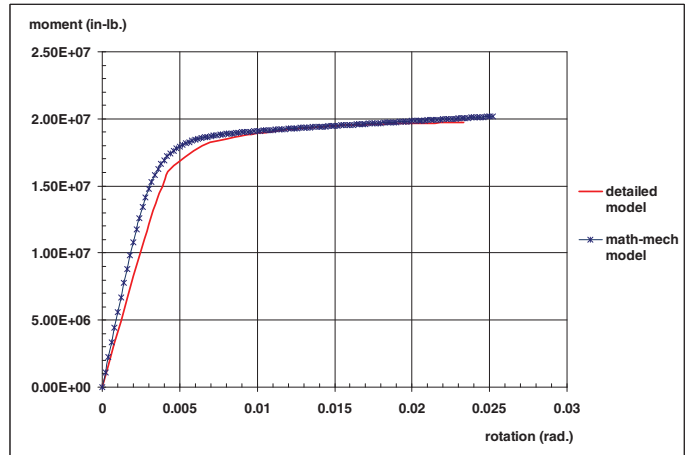
(l) Case 12
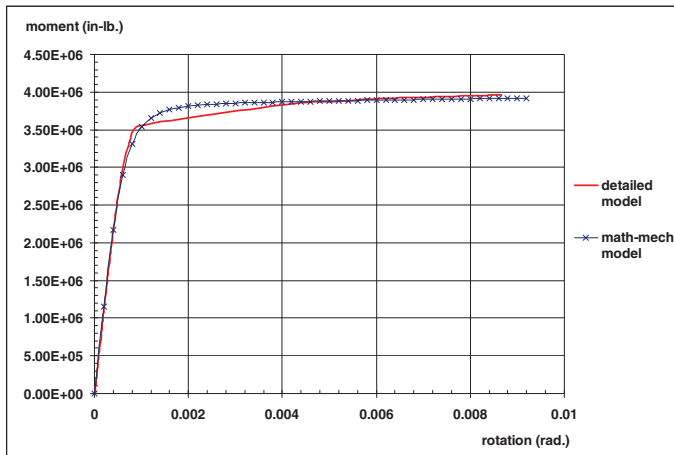
(m) Case 13
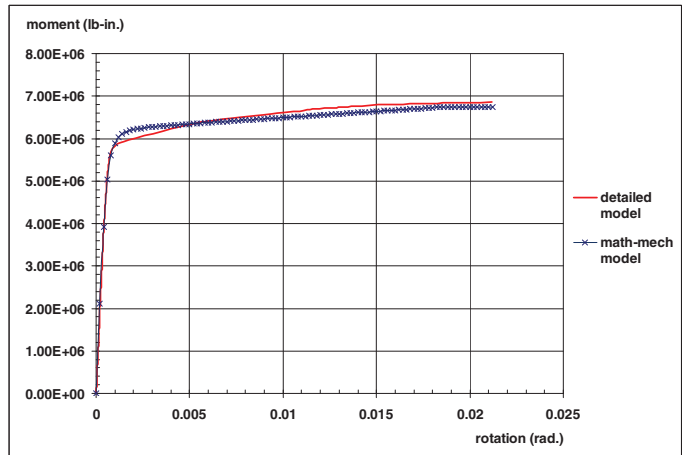
(n) Case 14
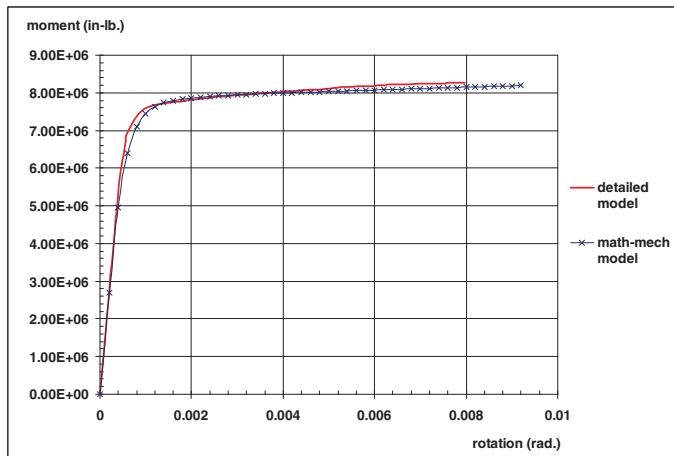
(o) Case 15
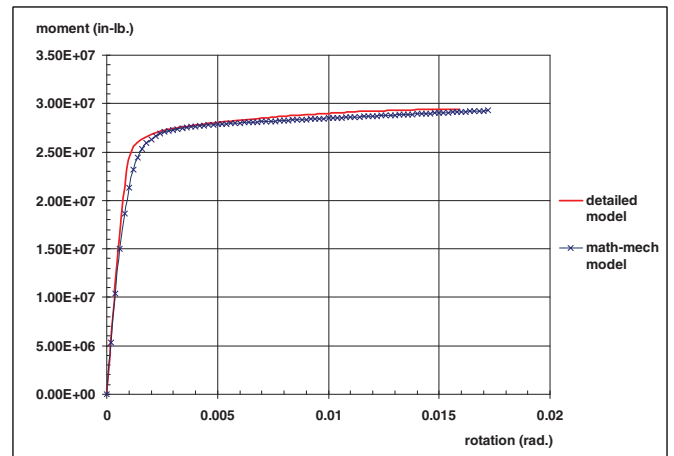
(p) Case 16

Fig. 8. Comparisons of the curves from mathematical-mechanical model with simulation results from detailed model (continued).

between the mathematical-mechanical models and the FEM simulations are less than 10 percent. These differences are probably due to the simplification of the detailed connection assembly. The $M - \theta$ curves produced in the mathematical-mechanical model were determined by mechanically defining the critical yield and ultimate points in terms of spring component behaviors and then mathematically connecting the points. In the FEM simulations, on the other hand, the $M - \theta$ curves were obtained by means of calculations of forces and deformations on a mesh of densely discrete elements, so that they can reflect the precise propagation of yielding and ultimate conditions in the girders and panel zones. Although the transition between pre-yield to post-yield behavior in the mathematical-mechanical model is based on two points and a shape factor, the derived curves compared well with the results from detailed simulations.

CONCLUSIONS

This study presents a comprehensive mathematical-mechanical modeling approach to define the resistance function of the welded unreinforced flange-bolted web (WUF-B) connection. The approach utilized a mathematical model for nonlinear characteristics, and a component method for coupling of individual components. A connection in a steel frame is a configuration of components that contains different geometries, shapes, and material properties. The same connection type may show diverse behavior, depending on the assembled components. Connection yielding will flow through the weakest component and spread to adjacent areas. Based on the hypothesis, this study considered the combined behaviors of individual components, since each of the assembled elements affects the combined behavior. In

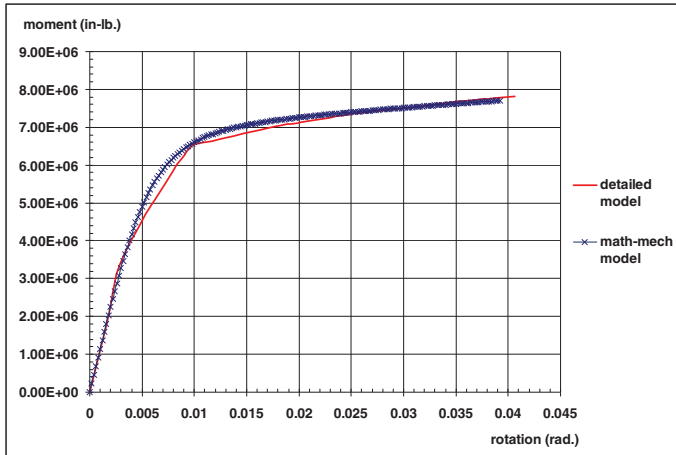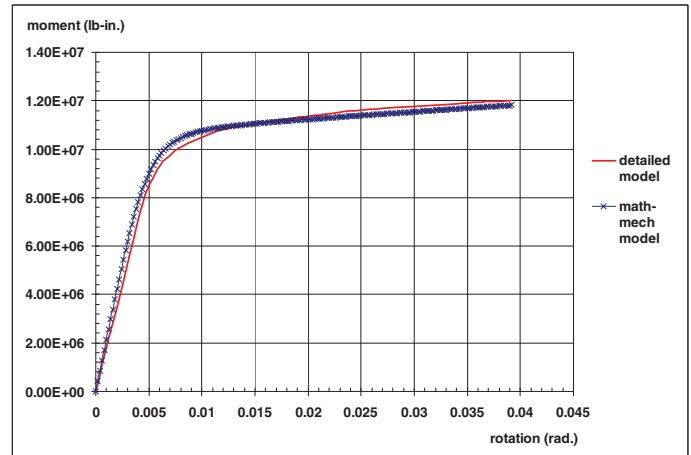*(q) Case 17*

(r) Case 18
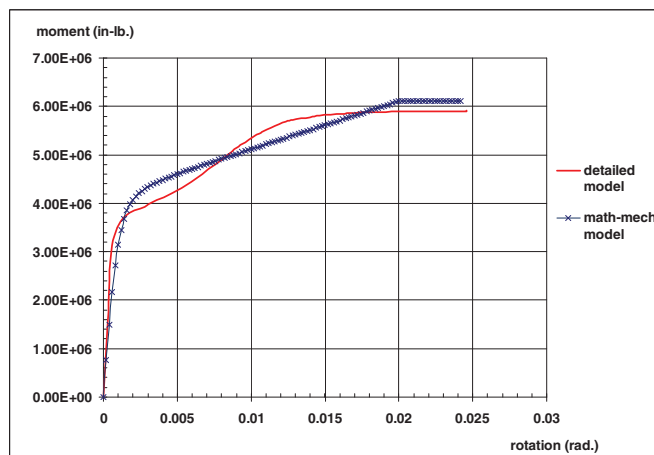
(s) Case 19
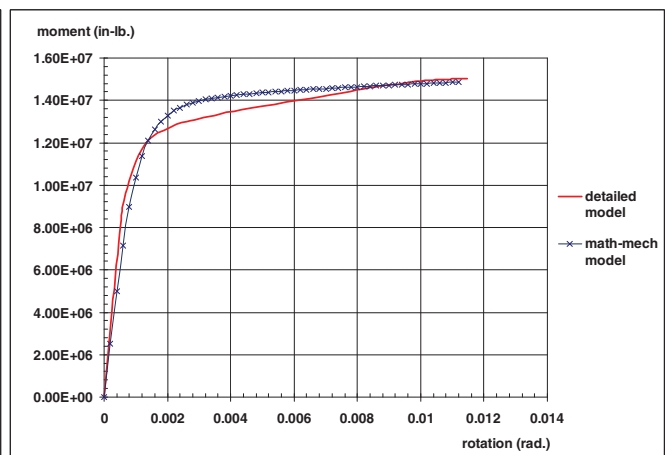
(t) Case 20

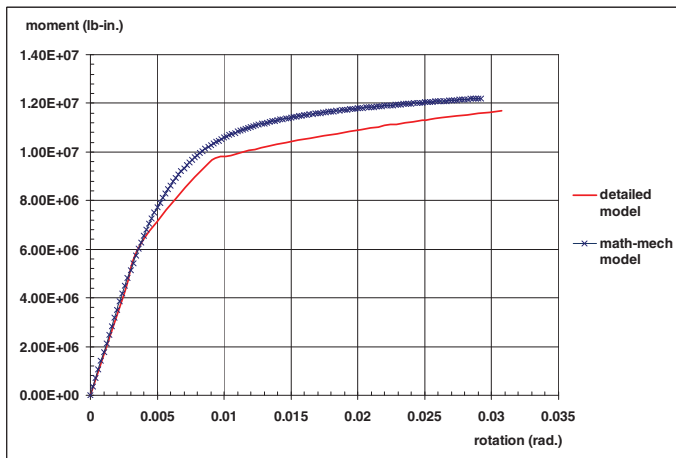*Fig. 8. Comparisons of the curves from mathematical-mechanical model with simulation results from detailed model (continued).*

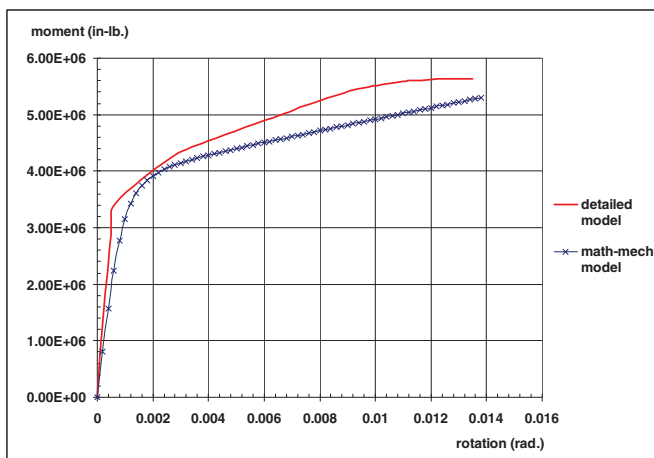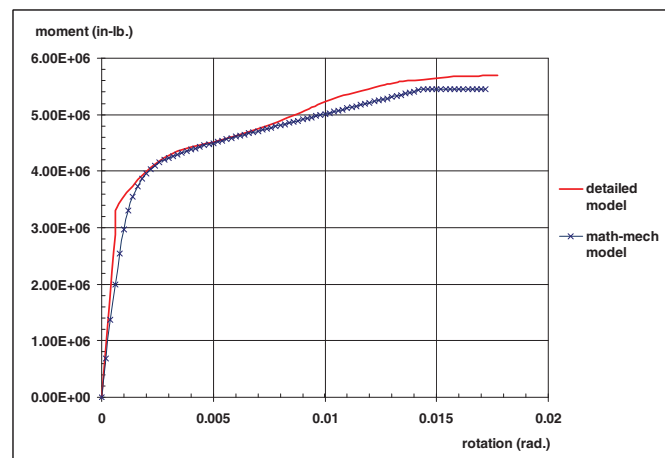order to evaluate the representation approaches proposed in this study, various possible cases were selected that show the yield flows in different directions. Then, by tracing the responses, appropriate equations were collected, modified, and newly developed for each component property. The WUF-B connections were reclassified according to strength comparison of panel zones and girder regions. Comparisons of the $M - \theta$ curves showed that the mathematical-mechanical models developed in this study are able to accurately predict the resistance functions for the selected connections. Since a steel building generally includes a large number of connections, this mathematical-mechanical method is expected to reduce computational effort while providing acceptable levels of accuracy in the frame analysis.

ACKNOWLEDGMENT

REFERENCES

AISC (2005), *Steel Construction Manual,* 13th Edition, American Institute of Steel Construction, Chicago, IL.

Attiogbe, E. and Morris, G. (1991), "Moment-Rotation Functions for Steel Connections," *Journal of Structural Engineering*, ASCE, Vol. 117, pp. 1703–1717.

Carter, C.J. (2003), *AISC Steel Design Guide 13, Stiffening of Wide-Flange Columns at Moment Connections: Wind and Seismic Applications*, American Institute of Steel Construction, Chicago, IL.

Dassault Systems (2008), *ABAQUS User Manual*, Version 6.7-EF, ABAQUS.

Engelhardt, M.D. and Husain, A.S. (1992), "Cyclic Tests on Large Scale Steel Moment Connections," Report No. PMFSEL-92-2, Phil M. Ferguson Structural Engineering Laboratory, Department of Civil Engineering, Universtiy of Texas at Austin.

Engelhardt, M.D. and Sabol, T.A. (1994), "Testing of Welded Steel Moment Connections in Response to the Northridge Earthquake," Progress Report to the AISC Advisory Subcommittee on Special Moment Resisting Frame Research.

European Prestandard (1997), "Eurocode 3—Part 1.1 Revised Annex J: Joint in Building Frames," European Committee for Standardization (CEN), Brussels, Belgium.

Faella, C., Piluso, V. and Rizzano, G. (2000), *Structural Steel Semi-rigid Connections—Theory, Design and Software*, CRC Press.

FEMA (2000), "State of the Art Report on Systems Performance of Steel Moment Frames Subjected to Earthquake Ground Shaking," FEMA 355C, Prepared by the SAC Joint Venture for the Federal Emergency Management Agency, Washington, DC.

Ivany, M. and Baniotopoulos, C.C. (2000), "Semi-Rigid Connections in Structural Steelwork," Springer Wien New York (SPIN).

Kishi, N. and Chen, W.F. (1986), "Database of Steel Beam-to-Column Connections," Structural Engineering Report No. CE-STR-86-26, Vol. 2, School of Civil Engineering, Purdue University, West Lafayette, IN.

Kishi, N. (1994), "Advanced Analysis of Steel Frames," ed. Chen, W.F. and Toma, S., CRC Press.

Krauthammer, T., Lim, J., Choi, H. and Elfahal, M. (2004), *Evaluation of Computational Approaches for Progressive Collapse and Integrated Munitions Effects Assessment*, PTC-TR-002-2004, the Protective Technology Center, Pennsylvania State University, University Park, PA.

Krawinkler, H. (1971), "Inelastic Behavior of Steel Beam-to-Column Subassemblages," Ph.D. dissertation, University of California, Berkeley, CA.

Lim, J.H. and Krauthammer, T. (2006), "Progressive Collapse Analyses of 2D Steel-Framed Structures with Different Connection Models," *Engineering Journal*, AISC, Vol. 43, No. 3, pp. 201–215.

Nethercot, D.A., (1985), "Utilizations of Experimentally Obtained Connection Data in Assessing the Performance of Steel Frames," *Connection Flexibility and Steel Frames*, ed. Chen, W.F., American Society of Civil Engineers, Reston, VA.

Richard, R.M. and Abbott, B.J. (1975), "Versatile Elastic Plastic Stress-Strain Formula," *Journal of Engineering Mechanics*, ASCE, Vol. 101, No. 4, pp. 511–515.

Rassati, G.A., Leon, R.T. and Noe, S. (2004), "Component Modeling of Partially Restrained Composite Joints under Cyclic and Dynamic Loading," *Journal of Structural Engineering,* ASCE, Vol. 130, No. 2, pp. 343–351.

Simoes da Silva, L., Santiago, A. and Real, P.V. (2002), "Post-Limit Stiffness and Ductility of End-Plate Beam to Column Steel Joints," *Computers and Structures*, Vol. 80, No. 5–6, pp. 515–531.

Tamboli, A.R. (1999), *Handbook of Structural Steel Connection Design and Details*, McGraw-Hill Companies, Inc., New York.

Tschemmernegg, F. (1988), "On the Nonlinear Behavior of Joints in Steel Frames," in *Connections in Steel Structures: Behavior, Strength and Design*, ed. R. Bjorhovde et. al., Elsevier Applied Science, London, United Kingdom, pp. 158–165.

Yim, H.C. and Krauthammer, T. (2009), "Load-Impulse Characterization for Steel Connection," *Interntional Journal of Impact Engineering*, Vol. 36, No. 5, pp. 737–745.

Uang, C.M. and Bondad, D. (1996), "Static Cyclic Testing of Pre-Northridge and Haunch Repaired Steel Moment Connections," Report No. SSRP-96/02, Division of Structural Engineering, University of California, San Diego.

Tables for Eccentrically Loaded WT Shapes in Compression

MARK E. GORDON

ABSTRACT

WT shapes are often used for bracing, and they are typically connected to their supports with gusset plates on the flange. This attachment creates an eccentric axial load on the WT, which is not considered by design tables in the 13th edition AISC *Manual of Steel Construction.* This paper demonstrates one method for generating design tables that account for this eccentric loading.

Keywords: WT shapes, compression, eccentric loading.

Horizontal WT braces commonly connect to their supports with gusset plates to the WT flange. This connection creates an eccentric axial loading. The axial compression tables in Section 4 of the 13th edition of the AISC *Steel Construction Manual* do not consider connection eccentricity. An Excel spreadsheet was developed to generate allowable stress design (ASD) and load and resistance factor design (LRFD) tables to assist engineers in considering these eccentric connections using the 13th edition *Manual*. Tables are located at the end of this paper. The available strengths in Table 1 (ASD) and Table 2 (LRFD) for WTs were determined by inputting different lengths and loads until a maximum load was found for which the WT still passed. The reduction factors in Table 3 (ASD) and Table 4 (LRFD) were developed by taking the maximum allowable P load with the eccentric connection and dividing by the maximum allowable P load without the eccentric connection. These factors are useful in reducing the allowable stresses in analysis and design programs, instead of having to check the WTs with eccentricities by hand. The tables were developed with the following assumptions:

1. ASD and LRFD, 2005 AISC *Specification for Structural Steel Buildings*.
2. WT member yield strength, F_y, of 50 ksi.
3. The WT members are horizontal, connected to a gusset plate at the flange, with the gusset plate on top.
4. Gusset plates are ½ in. thick.
5. The ends of the WT are pinned ($K = 1$).
6. Eccentricity taken from centroid of WT to the centroid of the gusset plate.

7. Design moment includes self-weight of WT.
8. For the LRFD method, a dead load factor of 1.2 is applied to the self-weight of the member.

The following examples demonstrate the procedure that is incorporated in the spreadsheet that was used to make the tables. Equation numbers refer to the 2005 AISC *Specification*.

EXAMPLE 1

Slender WT in Compression Using ASD
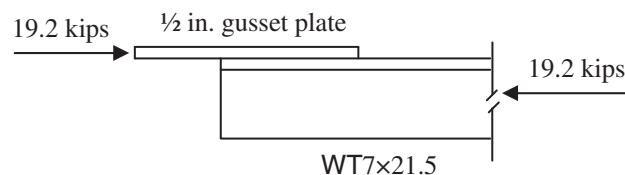
Given:
A 25 ft. horizontal WT7×21.5 brace with an axial compression load of 19.2 kips that is connected on top of the flange with a ½-in. gusset plate.

WT7×21.5 properties from Table 1-8 of the AISC *Manual* and from the AISC Shapes Database:

$A_g = 6.31$ in.^{2}
$d\ \ = 6.83$ in.
$t_w = 0.305$ in.
$b_f = 8.00$ in.
$t_f\ = 0.530$ in.
$I_x = 21.9$ in.^{4}
$S_x = 3.98$ in.^{3}
$r_x = 1.86$ in.
$\bar{y}\ = 1.31$ in.
$Z_x = 7.05$ in.^{3}
$I_y = 22.6$ in.^{4}

Mark E. Gordon, P.E., Senior Structural Engineer, Southern Company, 42 Inverness Center Parkway, Bin B453, Birmingham, AL 35242. E-mail: megordon@southernco.com

Table 1 (ASD)
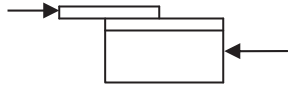
Horizontal WT Shapes

Available Strength (P_n/Ω_c)
for Compression Loads* with Connection Eccentricity
(kips)

$F_y = 50$ ksi

Shape	Span Length (ft)															
	2.5	5.0	7.5	10.0	12.5	15.0	17.5	20.0	22.5	25.0	27.5	30.0	32.5	35.0	37.5	40.0
WT4×9	27.1	24.0	19.9	15.4	11.4	8.64	6.62									
WT5×11	31.7	30.0	26.8	22.6	18.3	14.3	11.3	9.00								
WT5×13	38.4	36.1	31.8	26.7	21.5	16.9	13.3	10.6	8.49							
WT5×15	47.1	43.2	37.6	31.4	25.2	19.7	15.6	12.4	10.0							
WT6×11	30.0	27.3	22.2	16.2	11.6											
WT6×13	31.6	30.7	29.0	26.4	23.2	19.8	16.5	13.5	11.0	9.04						
WT6×15	40.9	39.5	36.8	32.8	28.3	23.7	19.3	15.6	12.8	10.5						
WT6×17.5	52.6	50.5	46.4	40.7	34.6	28.5	23.0	18.6	15.2	12.5						
WT6×20	58.1	55.7	51.1	44.1	37.0	30.3	24.3	19.5	15.8	12.9						
WT6×22.5	68.7	65.6	59.4	51.1	42.6	34.7	27.7	22.4	18.2	14.8						
WT6×25	78.0	73.3	65.5	56.4	47.2	38.5	30.9	25.0	20.3	16.6						
WT7×11	23.1	22.3	20.6	18.0	14.9	11.7										
WT7×13	31.3	30.1	27.4	23.5	19.2	14.8	11.6									
WT7×15	37.8	36.9	35.1	32.2	28.4	24.4	20.3	16.5	13.6							
WT7×17	45.7	44.5	42.0	38.2	33.5	28.6	23.7	19.3	15.9	13.1						
WT7×19	54.6	53.0	49.6	44.6	38.8	32.8	26.8	21.9	18.0	14.9						
WT7×21.5	61.7	59.9	56.6	51.6	45.6	39.5	33.7	28.1	23.2	19.3	16.0	13.4				
WT7×24	73.0	70.7	66.3	59.9	52.7	45.4	38.3	31.7	26.2	21.8	18.2	15.2				
WT7×26.5	82.9	80.0	74.6	67.1	58.8	50.3	42.2	34.8	28.8	24.0	20.0	16.8				
WT7×30.5	93.0	89.9	84.4	74.8	64.5	54.5	45.0	36.8	30.3	25.1	20.8					
WT7×34	108	103	94.1	83.3	71.9	60.8	50.2	41.2	33.9	28.1	23.3	19.4				
WT7×45	138	130	117	102	85.9	70.9	57.3	46.4	37.8	30.8	25.3					
WT8×33.5	102	99.3	95.6	90.1	82.5	73.4	64.3	55.6	47.5	40.1	34.0	28.9	24.6	21.0		
WT8×38.5	123	121	116	108	97.6	86.4	75.4	64.8	54.9	46.5	39.5	33.6	28.7	24.5		
WT8×44.5	148	143	135	125	113	100	87.6	75.6	64.2	54.5	46.4	39.6	33.8	29.0	24.8	
WT8×50	164	159	150	139	126	112	97.9	84.6	72.1	61.3	52.2	44.6	38.2	32.7	28.1	
WT9×38	114	112	109	104	98.0	90.2	81.6	73.0	64.5	56.2	48.5	41.7	36.0	31.1	26.9	23.3
WT9×43	137	135	130	124	116	106	95.0	84.3	73.8	64.0	55.0	47.4	40.9	35.4	30.6	26.5
WT9×48.5	164	159	152	143	132	120	108	95.5	83.5	72.1	62.1	53.5	46.3	40.0	34.7	30.1
WT9×53	179	174	166	156	144	131	118	105	91.8	79.6	68.6	59.2	51.3	44.4	38.6	33.5
WT9×59.5	199	194	185	174	161	147	132	117	103	89.4	77.1	66.7	57.8	50.2	43.6	37.9
WT9×65	214	208	199	187	173	157	141	125	109	94.9	81.8	70.7	61.2	53.1	46.0	39.9
WT9×71.5	232	226	216	203	188	171	154	137	120	105	90.4	78.2	67.8	58.8	51.1	44.4
WT10.5×83	278	272	262	250	235	219	201	183	165	148	131	115	101	88.9	78.2	68.9

*Based on the following:
- Horizontal WT member attached to a ½-in. gusset plate
- $K = 1$ (pinned ends)
- $\Omega_c = 1.67$

Note: Strength values only shown for $KL/r_{min} < 200$.

Table 2 (LRFD)

Horizontal WT Shapes

Available Strength ($\phi_c P_n$)
for Compression Loads* with Connection Eccentricity
(kips)

$F_y = 50$ ksi

Shape	Span Length (ft)															
	2.5	5.0	7.5	10.0	12.5	15.0	17.5	20.0	22.5	25.0	27.5	30.0	32.5	35.0	37.5	40.0
WT4×9	40.8	36.3	30.3	23.6	17.7	13.5	10.4									
WT5×11	47.7	45.3	40.6	34.5	28.1	22.1	17.5	14.1								
WT5×13	57.8	54.5	48.3	40.7	33.1	26.0	20.7	16.6	13.4							
WT5×15	70.9	65.2	57.1	47.9	38.8	30.5	24.2	19.5	15.8							
WT6×11	45.1	41.1	33.5	24.4	17.5											
WT6×13	47.5	46.3	43.9	40.0	35.3	30.4	25.5	20.9	17.2	14.2						
WT6×15	61.6	59.6	55.7	49.8	43.2	36.3	29.8	24.3	19.9	16.5						
WT6×17.5	79.2	76.2	70.2	61.9	52.9	43.8	35.5	28.9	23.8	19.7						
WT6×20	87.4	84.1	77.5	67.3	56.9	46.9	37.8	30.7	25.1	20.6						
WT6×22.5	103	99.0	90.2	78.0	65.5	53.6	43.2	35.1	28.7	23.7						
WT6×25	117	111	99.3	86.1	72.5	59.6	48.1	39.1	32.1	26.5						
WT7×11	34.8	33.6	31.0	27.1	22.5	17.7										
WT7×13	47.1	45.3	41.3	35.6	29.1	22.5	17.6									
WT7×15	56.8	55.5	52.9	48.7	43.2	37.1	31.0	25.4	21.0							
WT7×17	68.8	67.0	63.5	57.9	51.0	43.6	36.3	29.7	24.5	20.4						
WT7×19	82.1	79.8	74.9	67.6	59.0	50.0	41.1	33.6	27.8	23.1						
WT7×21.5	92.8	90.3	85.6	78.3	69.7	60.8	52.1	43.8	36.4	30.4	25.6	21.6				
WT7×24	110	107	100	91.1	80.5	69.8	59.3	49.4	41.2	34.5	29.0	24.5				
WT7×26.5	125	121	113	102	89.8	77.3	65.2	54.2	45.2	37.9	31.9	27.0				
WT7×30.5	140	136	128	114	98.8	83.9	69.8	57.5	47.7	39.8	33.3					
WT7×34	163	155	142	127	110	93.6	77.9	64.3	53.4	44.6	37.4	31.5				
WT7×45	207	195	177	155	132	110	89.2	72.8	59.8	49.4	41.0					
WT8×33.5	153	150	144	137	126	112	99.1	86.2	74.0	63.0	53.8	46.1	39.6	34.1		
WT8×38.5	186	182	175	164	149	132	116	100	85.5	72.9	62.3	53.5	46.0	39.7		
WT8×44.5	222	215	204	190	172	153	135	117	100	85.4	73.2	62.9	54.3	46.9	40.6	
WT8×50	247	239	227	210	191	171	151	131	112	95.9	82.3	70.9	61.2	52.9	45.9	
WT9×38	171	169	164	158	149	138	125	112	100	87.7	76.1	66.0	57.3	49.9	43.6	38.1
WT9×43	206	203	197	188	176	161	146	130	115	99.8	86.3	74.9	65.2	56.8	49.6	43.4
WT9×48.5	247	240	230	216	200	183	166	147	129	112	97.3	84.5	73.6	64.2	56.1	49.2
WT9×53	269	262	250	236	219	200	181	162	142	124	108	93.5	81.5	71.2	62.3	54.6
WT9×59.5	299	291	279	263	244	224	203	181	160	139	121	105	91.8	80.3	70.3	61.7
WT9×65	321	313	300	282	262	239	216	192	170	148	128	112	97.4	85.1	74.5	65.3
WT9×71.5	349	340	326	308	286	261	236	211	186	163	142	123	108	94.3	82.7	72.5
WT10.5×83	418	409	396	378	356	333	307	281	255	229	204	180	159	141	125	111

*Based on the following:
- Horizontal WT member attached to a ½-in. gusset plate
- $K = 1$ (pinned ends)
- $\phi_c = 0.90$

Note: Strength values only shown for $KL/r_{min} < 200$.

Table 3 (ASD)
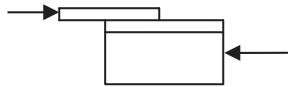
Horizontal WT Shapes

Reduction Factor for Compression Loads*
with Connection Eccentricity
$P_r/(P_n/\Omega_c)$

$F_y = 50$ ksi

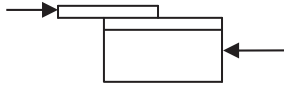| Shape	Span Length (ft)															
	2.5	5.0	7.5	10.0	12.5	15.0	17.5	20.0	22.5	25.0	27.5	30.0	32.5	35.0	37.5	40.0
WT4×9	0.391	0.389	0.398	0.439	0.501	0.545	0.568									
WT5×11	0.479	0.468	0.466	0.481	0.512	0.558	0.593	0.613								
WT5×13	0.435	0.425	0.428	0.445	0.479	0.527	0.562	0.582	0.590							
WT5×15	0.390	0.394	0.406	0.428	0.468	0.520	0.556	0.578	0.587							
WT6×11	0.539	0.563	0.624	0.709	0.776											
WT6×13	0.581	0.573	0.563	0.559	0.562	0.572	0.589	0.613	0.628	0.634						
WT6×15	0.519	0.511	0.504	0.508	0.521	0.543	0.575	0.604	0.620	0.626						
WT6×17.5	0.463	0.455	0.454	0.466	0.488	0.521	0.563	0.593	0.611	0.618						
WT6×20	0.436	0.421	0.408	0.416	0.432	0.458	0.495	0.520	0.533	0.536						
WT6×22.5	0.403	0.389	0.383	0.395	0.417	0.451	0.491	0.517	0.531	0.535						
WT6×25	0.376	0.372	0.378	0.390	0.411	0.445	0.485	0.512	0.527	0.532						
WT7×11	0.663	0.665	0.676	0.700	0.733	0.772										
WT7×13	0.606	0.609	0.626	0.658	0.701	0.749	0.783									
WT7×15	0.588	0.584	0.580	0.584	0.598	0.619	0.649	0.679	0.699							
WT7×17	0.550	0.545	0.543	0.549	0.565	0.589	0.622	0.654	0.675	0.687						
WT7×19	0.510	0.505	0.505	0.516	0.537	0.568	0.608	0.642	0.664	0.676						
WT7×21.5	0.487	0.477	0.465	0.459	0.458	0.463	0.473	0.493	0.515	0.528	0.532	0.529				
WT7×24	0.447	0.438	0.428	0.426	0.430	0.440	0.459	0.486	0.509	0.523	0.528	0.526				
WT7×26.5	0.419	0.410	0.403	0.404	0.411	0.427	0.452	0.484	0.507	0.520	0.526	0.524				
WT7×30.5	0.415	0.403	0.387	0.393	0.405	0.425	0.455	0.486	0.506	0.517	0.519					
WT7×34	0.378	0.373	0.376	0.384	0.397	0.418	0.450	0.482	0.502	0.513	0.516	0.511				
WT7×45	0.361	0.361	0.366	0.376	0.395	0.424	0.462	0.489	0.503	0.508	0.503					
WT8×33.5	0.472	0.464	0.452	0.439	0.433	0.437	0.445	0.457	0.475	0.495	0.508	0.514	0.514	0.508		
WT8×38.5	0.429	0.421	0.410	0.401	0.403	0.412	0.425	0.444	0.470	0.491	0.504	0.511	0.512	0.507		
WT8×44.5	0.397	0.396	0.393	0.391	0.396	0.404	0.418	0.436	0.462	0.483	0.498	0.505	0.507	0.503	0.495	
WT8×50	0.389	0.388	0.386	0.386	0.391	0.400	0.413	0.432	0.458	0.480	0.495	0.503	0.505	0.502	0.495	
WT9×38	0.499	0.493	0.483	0.472	0.462	0.457	0.455	0.456	0.461	0.471	0.486	0.498	0.504	0.505	0.501	0.494
WT9×43	0.456	0.450	0.441	0.431	0.426	0.424	0.427	0.434	0.447	0.464	0.483	0.495	0.502	0.503	0.500	0.493
WT9×48.5	0.412	0.411	0.409	0.408	0.408	0.410	0.414	0.424	0.440	0.461	0.480	0.493	0.500	0.501	0.499	0.492
WT9×53	0.407	0.406	0.405	0.405	0.405	0.407	0.411	0.420	0.435	0.455	0.475	0.488	0.496	0.498	0.496	0.490
WT9×59.5	0.399	0.398	0.397	0.397	0.398	0.400	0.406	0.417	0.432	0.452	0.472	0.486	0.494	0.498	0.496	0.490
WT9×65	0.388	0.387	0.386	0.386	0.386	0.391	0.399	0.411	0.426	0.447	0.466	0.480	0.487	0.490	0.488	0.482
WT9×71.5	0.381	0.381	0.380	0.380	0.382	0.387	0.395	0.406	0.421	0.441	0.461	0.475	0.483	0.487	0.485	0.479
WT10.5×83	0.395	0.395	0.395	0.396	0.397	0.399	0.403	0.409	0.417	0.429	0.443	0.460	0.473	0.482	0.486	0.487

*Based on the following:
- Horizontal WT member attached to a ½-in. gusset plate
- $K = 1$ (pinned ends)
- $\Omega_c = 1.67$

Note: Strength values only shown for $KL/r_{min} < 200$.

Table 4 (LRFD)

Horizontal WT Shapes

Reduction Factor for Compression Loads*
with Connection Eccentricity
$P_u/(\phi_c P_n)$

F_y = 50 ksi

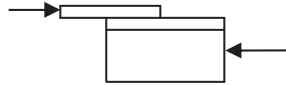| Shape	Span Length (ft)															
	2.5	5.0	7.5	10.0	12.5	15.0	17.5	20.0	22.5	25.0	27.5	30.0	32.5	35.0	37.5	40.0
WT4×9	0.391	0.392	0.404	0.448	0.515	0.564	0.594									
WT5×11	0.479	0.470	0.470	0.488	0.523	0.573	0.612	0.637								
WT5×13	0.435	0.427	0.432	0.452	0.490	0.542	0.581	0.607	0.621							
WT5×15	0.390	0.396	0.410	0.435	0.478	0.534	0.575	0.603	0.618							
WT6×11	0.539	0.564	0.626	0.713	0.781											
WT6×13	0.582	0.574	0.566	0.564	0.570	0.584	0.605	0.632	0.652	0.663						
WT6×15	0.520	0.512	0.507	0.513	0.529	0.554	0.590	0.623	0.644	0.656						
WT6×17.5	0.463	0.456	0.457	0.471	0.496	0.532	0.578	0.612	0.634	0.647						
WT6×20	0.437	0.423	0.412	0.422	0.441	0.472	0.513	0.543	0.562	0.571						
WT6×22.5	0.403	0.390	0.387	0.401	0.426	0.464	0.508	0.539	0.559	0.569						
WT6×25	0.376	0.373	0.381	0.395	0.420	0.457	0.502	0.534	0.555	0.565						
WT7×11	0.663	0.666	0.678	0.703	0.738	0.779										
WT7×13	0.606	0.610	0.628	0.661	0.706	0.756	0.792									
WT7×15	0.589	0.585	0.582	0.588	0.604	0.628	0.660	0.694	0.717							
WT7×17	0.551	0.546	0.545	0.553	0.571	0.598	0.634	0.670	0.694	0.710						
WT7×19	0.510	0.506	0.507	0.520	0.544	0.577	0.620	0.657	0.683	0.699						
WT7×21.5	0.487	0.478	0.468	0.463	0.466	0.473	0.487	0.511	0.538	0.556	0.565	0.568				
WT7×24	0.448	0.439	0.431	0.431	0.437	0.450	0.472	0.504	0.531	0.550	0.560	0.563				
WT7×26.5	0.420	0.412	0.406	0.409	0.419	0.437	0.465	0.501	0.529	0.547	0.558	0.562				
WT7×30.5	0.415	0.404	0.390	0.398	0.413	0.436	0.470	0.505	0.530	0.546	0.553					
WT7×34	0.378	0.374	0.379	0.389	0.404	0.429	0.464	0.500	0.526	0.542	0.550	0.551				
WT7×45	0.361	0.362	0.369	0.382	0.403	0.436	0.478	0.510	0.531	0.541	0.543					
WT8×33.5	0.473	0.465	0.454	0.443	0.439	0.445	0.456	0.472	0.493	0.517	0.534	0.545	0.550	0.549		
WT8×38.5	0.429	0.422	0.412	0.404	0.409	0.420	0.436	0.458	0.487	0.512	0.530	0.541	0.547	0.547		
WT8×44.5	0.398	0.397	0.395	0.395	0.401	0.412	0.428	0.449	0.478	0.504	0.523	0.535	0.541	0.543	0.539	
WT8×50	0.389	0.389	0.388	0.390	0.397	0.408	0.423	0.445	0.474	0.500	0.519	0.532	0.539	0.541	0.538	
WT9×38	0.499	0.493	0.485	0.475	0.467	0.464	0.464	0.468	0.475	0.489	0.508	0.524	0.534	0.540	0.541	0.538
WT9×43	0.456	0.450	0.442	0.434	0.430	0.431	0.435	0.445	0.461	0.481	0.504	0.520	0.531	0.537	0.539	0.536
WT9×48.5	0.412	0.411	0.411	0.411	0.413	0.416	0.422	0.435	0.454	0.478	0.501	0.517	0.529	0.535	0.537	0.535
WT9×53	0.407	0.407	0.407	0.408	0.409	0.413	0.420	0.431	0.449	0.472	0.495	0.513	0.524	0.531	0.534	0.532
WT9×59.5	0.399	0.399	0.399	0.400	0.402	0.406	0.414	0.428	0.446	0.469	0.492	0.510	0.523	0.530	0.533	0.532
WT9×65	0.388	0.388	0.388	0.389	0.391	0.398	0.408	0.421	0.440	0.463	0.487	0.504	0.516	0.523	0.525	0.524
WT9×71.5	0.381	0.381	0.382	0.383	0.386	0.393	0.403	0.416	0.434	0.457	0.481	0.499	0.511	0.519	0.522	0.521
WT10.5×83	0.395	0.396	0.397	0.398	0.400	0.404	0.410	0.418	0.428	0.442	0.459	0.479	0.496	0.508	0.517	0.521

*Based on the following:
- Horizontal WT member attached to a ½-in. gusset plate
- K = 1 (pinned ends)
- ϕ_c = 0.90

Note: Strength values only shown for KL/r_{min} < 200.

r_y = 1.89 in.
Q_s = 0.776
J = 0.522 in.^{4}
$\bar{r}_o$ = 2.86 in. (Equation E4-7, $\bar{r}_o^2$)
H = 0.865 (Equation E4-8)

$S_{xc} = I_x/y_c = 21.9/1.31 = 16.72$ in.^{3}

Check for slender elements:

From Table B4.1 Case 8,

$$\frac{d}{t_w} = \frac{6.83}{0.305} = 22.4 > \lambda_r = 0.75\sqrt{\frac{E}{F_y}} = 0.75\sqrt{\frac{29,000}{50}} = 18.1$$

Therefore, the web is slender.

From Table B4.1 Case 3,

$$\frac{b_f}{2t_f} = \frac{8.00}{2(0.530)} = 7.5 < \lambda_r = 0.56\sqrt{\frac{E}{F_y}} = 0.56\sqrt{\frac{29,000}{50}} = 13.5$$

Therefore, the flange is noncompact.

There are slender elements. Specification Section E7 is applicable.

The cross section is composed of only unstiffened compression elements. Therefore, $Q_a = 1.0$.

$Q = Q_s Q_a = (0.776)(1.0) = 0.776$

Flexural buckling about the x-x axis:

$$\frac{KL}{r_x} = \frac{1.0(25\text{ft})(12 \text{ in./ft})}{1.86 \text{ in.}} = 161.3$$

$$4.71\sqrt{\frac{E}{QF_y}} = 4.71\sqrt{\frac{29,000}{(0.776)50}} = 128.8 < 161.3$$

Therefore, Equation E7-3 applies.

From Equation E3-4,

$$F_e = \frac{\pi^2 E}{\left(\dfrac{KL}{r_x}\right)^2} = \frac{\pi^2(29,000)}{(161.3)^2} = 11.0 \text{ ksi}$$

From Equation E7-3,

$F_{cr} = 0.877F_e = 0.877(11.0) = 9.6$ ksi; **controls**

Flexural buckling about the y-y axis:

$$\frac{KL}{r_y} = \frac{1.0\left(25 \text{ ft}\right)\left(12 \text{ in./ft}\right)}{1.89 \text{ in.}} = 158.7$$

$$4.71\sqrt{\frac{E}{QF_y}} = 4.71\sqrt{\frac{29,000}{(0.776)50}} = 128.8 < 158.7$$

Therefore, Equation E7-3 applies.

From Equation E3-4,

$$F_e = \frac{\pi^2 E}{\left(\dfrac{KL}{r_y}\right)^2} = \frac{\pi^2(29,000)}{(158.7)^2} = 11.4 \text{ ksi}$$

From Equation E7-3,

$F_{cr} = 0.877F_e = 0.877(11.4) = 10.0$ ksi; **does not control**

Torsional and flexural-torsional buckling of members with slender elements:

From Equation E4-11,

$$F_{ez} = \left[\frac{\pi^2 E C_w}{\left(K_z L\right)^2} + GJ\right]\frac{1}{A_g \bar{r}_o^2}$$

Omit term with C_w per User Note at end of Section E4.

$$F_{ez} = \frac{GJ}{A_g \bar{r}_o^2} = \frac{11,200(0.522)}{6.31(2.86)^2} = 113.3 \text{ ksi}$$

Calculate F_e using Equation E4-5,

$$F_e = \left(\frac{F_{ey} + F_{ez}}{2H}\right)\left[1 - \sqrt{1 - \frac{4F_{ey}F_{ez}H}{\left(F_{ey} + F_{ez}\right)^2}}\right]$$

$$= \left(\frac{11.4 + 113.3}{2(0.865)}\right)\left[1 - \sqrt{1 - \frac{4(11.4)(113.3)(0.865)}{\left(11.4 + 113.3\right)^2}}\right]$$

$$= 11.2 \text{ ksi}$$

$0.44QF_y = 0.44(0.776)(50) = 17.1 > 11.2$ ksi

Therefore, use equation E7-3.

$F_{cry} = 0.877F_e = 9.8$ ksi; **does not control**

Nominal compressive strength:

$P_n = F_{cr}A_g = (9.6)(6.31) = 60.9$ kips

Calculate the required flexural strength:

Moment due to axial load, $M_{ecc} = P(y + y')$ where $y' = \frac{1}{4}$ in., half of $\frac{1}{2}$-in.-thick gusset plate.

$$M_{ecc} = (19.2)(1.31 + 0.25)$$
$$= 30.0 \text{ kip-in.}$$

Moment due to weight of WT, $M_0 = wL^2/8$

$M_0 = 20.2$ kip-in.

$M_{nt} = M_{ecc} + M_0 = 30.0 + 20.2 = 50.1$ kip-in. (ASD)

Second-order effects with C_m based on Section C2.1b,

$\alpha = 1.6$ (ASD)

$C_m = 1$

From Equation C2-5,

$$P_{e1} = \frac{\pi^2 EI}{\left(K_1 L\right)^2} = \frac{\pi^2 (29,000)(21.9)}{\left[(25)(12)\right]^2} = 69.6 \text{ kips}$$

From Equation C2-2,

$$B_1 = \frac{1}{1 - \alpha P_r / P_{e1}} \geq 1.0$$

$$B_1 = \frac{1}{1 - 1.6(19.2)/69.6} = 1.79 \text{ (ASD)}$$

$M_1 = B_1 M_{nt} = (1.79)(50.1) = 89.7$ kip-in (ASD)

Calculate the nominal flexural strength:

Flexural yielding limit state is $M_p = F_y Z_c < 1.6 M_y$

Using Equation F9-2,

$M_p = F_y Z_x < 1.6 M_y$, for stems in tension

$1.6 M_y = 1.6 F_y S_x = 1.6(50)(3.98) = 318.4$ kip-in.

$M_p = F_y Z_x = (50)(7.05) = 352.5$ kip-in.

From Equation F9-1,

$M_n = M_p = 318.4$ kip-in.; **controls**

Flange local buckling limit state:

Check flange compactness using Table B4.1 Case 7,

$$\lambda = \frac{b_f}{2t_f} = \frac{8.0}{2(0.530)} = 7.5$$

$$\lambda_p = 0.38 \sqrt{\frac{E}{F_y}} = 0.38 \sqrt{\frac{29,000}{50}} = 9.2 > 7.5$$

Therefore, the flange is compact.

Check flange slenderness using Table B4.1 Case 7,

$$\lambda_r = 1.0 \sqrt{\frac{E}{F_y}} = 1.0 \sqrt{\frac{29,000}{50}} = 24.08 > 7.5$$

Therefore, the flange is not slender.

Calculate critical flange local buckling stress (only applicable if noncompact or slender),

For noncompact sections (Equation F9-7),

$$F_{cr} = F_y \left(1.19 - 0.50 \left(\frac{b_f}{2t_f} \right) \sqrt{\frac{F_y}{E}} \right)$$

For slender sections (Equation F9-8),

$$F_{cr} = 0.69 \frac{E}{\left(\dfrac{b_f}{2t_f} \right)^2}$$

Calculate the nominal flexural strength (Equation F9-6),

$M_n = F_{cr} S_x$ not applicable

Lateral-torsional buckling:

From Equation F9-4,

$$M_n = M_{cr} = \pi \frac{\sqrt{EI_y GJ}}{L_b} \left[B + \sqrt{\left(1 + B^2\right)} \right]$$

From Equation F9-5,

$$B = \pm 2.3 \left(\frac{d}{L_b} \right) \sqrt{\frac{I_y}{J}}$$

$$= +2.3 \left(\frac{6.83}{25(12)} \right) \sqrt{\left(\frac{22.6}{0.522} \right)}$$

$$= +0.345$$

$$B + \sqrt{\left(1 + B^2\right)} = \left[+0.345 + \sqrt{1 + \left(+0.345 \right)^2} \right]$$

$$= 1.403$$

$$M_n = M_{cr} = \pi \frac{\sqrt{(29,000)(22.6)(11,200)(0.522)}}{25(12)} (1.403)$$

$M_n = 909.0$ k-in.; **does not control**

Design of WT member for combined forces:

Since $I_{yc}/I_y \approx 1.0 > 0.9$, use H2-1.

From Equation H2-1,

$$\frac{f_a}{F_a} + \frac{f_{bw}}{F_{bw}} \leq 1.0$$

Which can be rewritten for ASD as,

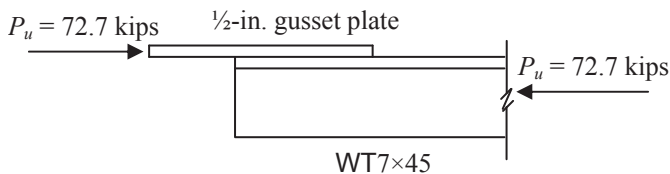$$\frac{P_r}{\left(P_n/\Omega_c\right)} + \frac{M_r}{\left(M_n/\Omega_b\right)} \leq 1.0$$

$$\frac{19.2}{\left(60.9/1.67\right)} + \frac{89.7}{\left(318.4/1.67\right)} = 1.0 \leq 1.0$$

Calculate the reduction factor for the compression load with connection eccentricity:

$$\frac{P_r}{\left(P_n/\Omega_c\right)} = \frac{19.2}{\left(60.9/1.67\right)} = 0.528$$

EXAMPLE 2

Nonslender WT in Compression and Noncompact in Bending Using LRFD

WT7×45

Given:
A 20-ft. horizontal WT7×45 brace with an ultimate axial compression load of 72.7 kips that is connected on top of the flange with a ½-in. gusset plate.

WT7×45 Properties from Table 1-8 of the AISC *Manual* and the AISC Shapes Database:

A_g = 13.20 in.^{2}
d = 7.01 in.
t_w = 0.440 in.
b_f = 14.50 in.
t_f = 0.710 in.
I_x = 36.5 in.^{4}
S_x = 6.16 in.^{3}
r_x = 1.66 in.
$\bar{y}$ = 1.09 in.
Z_x = 11.50 in.^{3}
I_y = 181 in.^{4}
r_y = 3.70 in.
Q_s = 1.0
J = 2.030 in.^{4}
$\bar{r}_o$ = 4.12 in. (Equation E4-7, $\bar{r}_o^2$)
H = 0.968 (Equation E4-8)

$S_{xc} = I_x/y_c = 36.5/1.09 = 33.49$ in.^{3}

Check for slender elements:

From Table B4.1 Case 8,

$$\frac{d}{t_w} = \frac{7.01}{0.440} = 15.9 < \lambda_r = 0.75\sqrt{\frac{E}{F_y}} = 0.75\sqrt{\frac{29,000}{50}} = 18.1$$

Therefore, the web is noncompact.

From Table B4.1 Case 3,

$$\frac{b_f}{2t_f} = \frac{14.50}{2(0.710)} = 10.2 < \lambda_r = 0.56\sqrt{\frac{E}{F_y}} = 0.56\sqrt{\frac{29,000}{50}} = 13.5$$

Therefore, the flange is noncompact.

There are no slender elements. AISC *Specification* Sections E3 and E4 apply.

Flexural buckling about the x-x axis:

$$\frac{KL}{r_x} = \frac{1.0(20\text{ ft})(12\text{ in./ft})}{1.66\text{ in.}} = 144.6$$

$$4.71\sqrt{\frac{E}{F_y}} = 4.71\sqrt{\frac{29,000}{50}} = 113.4 < 144.6$$

Therefore, Equation E3-3 applies.

From Equation E3-4,

$$F_e = \frac{\pi^2 E}{\left(\dfrac{KL}{r_x}\right)^2} = \frac{\pi^2(29,000)}{\left(144.6\right)^2} = 13.7\text{ ksi}$$

From Equation E3-3,

$F_{cr} = 0.877F_e = 0.877(13.7) = 12.0$ ksi; **controls**

Flexural buckling about the y-y axis:

$$\frac{KL}{r_y} = \frac{1.0(20\text{ ft})(12\text{ in./ft})}{3.70\text{ in.}} = 64.9$$

$$4.71\sqrt{\frac{E}{F_y}} = 4.71\sqrt{\frac{29,000}{50}} = 113.4 > 64.9$$

Therefore, Equation E3-2 applies.

From Equation E3-4,

$$F_e = \frac{\pi^2 E}{\left(\dfrac{KL}{r_y}\right)^2} = \frac{\pi^2(29,000)}{\left(64.9\right)^2} = 68.0\text{ ksi}$$

From Equation E3-2,

$$F_{cry} = \left[0.658^{\frac{F_y}{F_e}}\right]F_y = \left[0.658^{\frac{50}{68.0}}\right]50$$

$F_{cry} = 36.8$ ksi; **does not control**

Torsional and flexural-torsional buckling of members without slender elements:

From Equation E4-3,

$$F_{crz} = \frac{GJ}{A_g \bar{r}_o^2} = \frac{11,200(2.030)}{13.20(4.12)^2} = 101.5\,\text{ksi}$$

From Equation E4-2,

$$F_{cr} = \left(\frac{F_{cry} + F_{crz}}{2H}\right)\left[1 - \sqrt{1 - \frac{4F_{cry}F_{crz}H}{\left(F_{cry} + F_{crz}\right)^2}}\right]$$

$$= \left(\frac{36.8 + 101.5}{2(0.968)}\right)\left[1 - \sqrt{1 - \frac{4(36.8)(101.5)(0.968)}{\left(36.8 + 101.5\right)^2}}\right]$$

$F_{cr} = 36.1$ ksi; **does not control**

Nominal compressive strength:

$P_n = F_{cr}A_g = (12.0)(13.20) = 158.5$ kips

Calculate the required flexural strength:

Moment due to axial load, $M_{ecc} = P(y + y')$ where $y' = \frac{1}{4}$ in., half of ½-in.-thick gusset plate.

$M_{ecc} = (72.7)(1.09 + 0.25)$

$\quad = 97.4$ kip-in.

Moment due to weight of WT, $M_0 = wL^2/8$

$M_0 = 27.0$ kip-in.

$M_{nt} = 1.2M_0 + M_{ecc}$
$\quad = 1.2(27.0) + 97.4 = 129.8$ kip-in. (LRFD)

Second-order effects with C_m based on section C2.1b,

$\alpha \quad = 1.0$ (LRFD)

$C_m \quad = 1$

From Equation C2-5,

$$P_{e1} = \frac{\pi^2 EI_x}{\left(K_1 L\right)^2} = \frac{\pi^2 (29,000)(36.5)}{\left[(20)(12)\right]^2} = 181.4\,\text{kips}$$

From Equation C2-2,

$$B_1 = \frac{1}{1 - \alpha P_r / P_{e1}} \geq 1.0$$

$$B_1 = \frac{1}{1 - 1.0(72.7)/181.4} = 1.67 \quad \text{(LRFD)}$$

$M_1 = B_1 M_{nt} = (1.67)(129.8) = 216.7$ kip-in (LRFD)

Calculate the nominal flexural strength:

Flexural yielding limit state is $M_p = F_y Z_x < 1.6M_y$

Using Equation F9-2,

$M_p = F_y Z_x < 1.6\,M_y$ for stems in tension

$1.6M_y = 1.6F_y S_x = 1.6(50)(6.16) = 492.8$ kip-in.

$M_p = F_y Z_x = (50)(11.50) = 575$ kip-in.

From Equation F9-1,

$M_n = M_p = 492.8$ kip-in.; **controls**

Flange local buckling limit state:

Check flange compactness using Table B4.1 Case 7,

$$\lambda = \frac{b_f}{2t_f} = \frac{14.5}{2(0.710)} = 10.2$$

$$\lambda_p = 0.38\sqrt{\frac{E}{F_y}} = 0.38\sqrt{\frac{29,000}{50}} = 9.2 < 10.2$$

Therefore, the flange is noncompact.

Check flange slenderness using Table B4.1 Case 7,

$$\lambda_r = 1.0\sqrt{\frac{E}{F_y}} = 1.0\sqrt{\frac{29,000}{50}} = 24.1 > 10.2$$

Therefore, the flange is noncompact.

Calculate critical flange local buckling stress:

For noncompact sections (Equation F9-7),

$$F_{cr} = F_y\left(1.19 - 0.50\left(\frac{b_f}{2t_f}\right)\sqrt{\frac{F_y}{E}}\right)$$

$$= 50\left(1.19 - 0.50\left(\frac{14.5}{2(0.71)}\right)\sqrt{\frac{50}{29000}}\right)$$

$$= 48.9\,\text{ksi}$$

Calculate the nominal flexural strength (Equation F9-6),
$M_n = F_{cr}S_{xc} = (48.9)(33.49)$

$M_n = 1637.5$ kip-in.; **does not control**

Lateral-torsional buckling:

From Equation F9-4,

$$M_n = M_{cr} = \pi \frac{\sqrt{EI_y GJ}}{L_b}\left[B + \sqrt{\left(1 + B^2\right)}\right]$$

From Equation F9-5,

$$B = \pm 2.3\left(\frac{d}{L_b}\right)\sqrt{\frac{I_y}{J}}$$

$$= +2.3\left(\frac{7.01}{20(12)}\right)\sqrt{\left(\frac{181}{2.03}\right)}$$

$$= +0.634$$

$$B + \sqrt{\left(1 + B^2\right)} = \left[+0.634 + \sqrt{\left(1 + \left(+0.634\right)^2\right)}\right]$$

$$= 1.818$$

$$M_n = M_{cr} = \pi \frac{\sqrt{\left(29,000\right)\left(181\right)\left(11,200\right)\left(2.03\right)}}{20(12)}\left(1.818\right)$$

$M_n = 8223.7$ k-in.; **does not control**

Design of WT member for combined forces:

Since $I_{yc}/I_y \approx 1.0 > 0.9$ use H2-1.

From Equation H2-1,

$$\frac{f_a}{F_a} + \frac{f_{bw}}{F_{bw}} \leq 1.0$$

which can be rewritten for LRFD as,

$$\frac{P_u}{\left(\phi_c P_n\right)} + \frac{M_u}{\left(\phi_b M_n\right)} \leq 1.0$$

$$\frac{72.7}{(0.9)(158.5)} + \frac{216.7}{(0.9)(492.8)} = 1.0 \leq 1.0$$

Calculate the reduction factor for the compression load with connection eccentricity:

$$\frac{P_u}{\left(\phi_c P_n\right)} = \frac{72.7}{(0.9)(158.5)} = 0.510$$

REFERENCES

AISC (2005), *Specification for Structural Steel Buildings*, American Institute of Steel Construction, Chicago, IL.

Stiffener Requirements to Prevent Edge Buckling

BO DOWSWELL

This paper was presented at the 2009 Annual Stability Conference of the Structural Stability Research Council.

ABSTRACT

Steel connection elements such as gusset plates and coped beam webs feature unsupported edges that are sometimes stiffened to prevent buckling. The stiffener requirements for structural elements with large aspect ratios are well established. However, for typical connections with an aspect ratio of ½ to 2, the existing requirements may not provide accurate results. The results from 123 elastic finite element models were analyzed to determine the stiffness requirements for edge stiffeners with smaller aspect ratios. A design procedure based on a simplified model is proposed as a starting point for stiffener design.

Keywords: edge stiffeners, coped beams, gusset plates.

In steel connection elements such as gusset plates and coped beam webs, unsupported edges are sometimes stiffened to prevent buckling. The top edges of coped beam webs are subjected to compressive flexural stresses as shown in Figure 1, which can cause a local instability. The AISC *Steel Construction Manual* (AISC, 2005) provides equations to determine the buckling capacity. To increase the critical stress of the coped section, the edge can be stiffened as shown in Figure 2.

In seismic applications, Nast et al. (1999), and Rabinovitch and Cheng (1993) showed that the addition of gusset plate edge stiffeners results in significantly improved energy absorption capability and a more stable post-buckling response. The AISC *Seismic Design Manual* (AISC, 2006) recommends stiffening the edge when the unsupported length exceeds

$$L_{fg} = 0.75t\sqrt{\frac{E}{F_y}} \qquad (1)$$

where

L_{fg} = free length of the gusset plate at the edge, in., as shown in Figure 3
t = gusset plate thickness, in.
E = modulus of elasticity, ksi
F_y = yield stress of the material, ksi

Design limits for the maximum unsupported length of the free edge of gusset plates are also provided by AASHTO (2004), Astaneh (1998), Reno and Duan (1997), and Caltrans (2001). When these limits are not met, the edge can be stiffened as shown in Figure 4.

For the stiffener to be effective, it must be stiff enough to alter the buckled shape of the plate. The stiffener requirements for structural elements with large aspect ratios are well established (AISI, 1997). In this paper, the aspect ratio is defined as the length-to-width ratio of the plate, *a/b*, as shown in Figure 5. For typical connections, the aspect ratio varies from ½ to 2, and the existing requirements may not provide accurate results. This paper will examine the effect of the aspect ratio on the stiffener requirements to prevent edge buckling.

The results from 123 elastic finite element models were used to determine the critical flexural stiffness of edge stiffeners. The effects of width-to-thickness ratio and aspect ratio of the braced element were studied, resulting in a simple equation that can be used to predict the minimum moment of inertia required to force the plate to buckle in a stiffened mode.
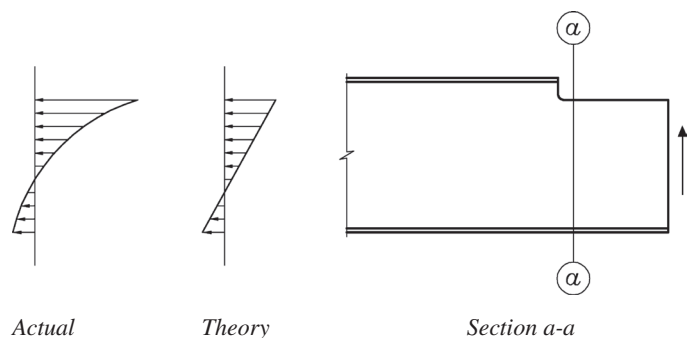
Bo Dowswell, Principal, SDS Resources, LLC, 300 Cahaba Park Circle, Suite 116, Birmingham, AL 35242. E-mail: bo@sdsresources.com

Actual　　　*Theory*　　　*Section a-a*

Fig. 1. Flexural stress at a beam cope.

BACKGROUND

Plate Buckling

For infinitely long plates, the well known plate buckling equation is (Galambos, 1998)

$$\sigma_c = k \frac{\pi^2 E}{12\left(1 - v^2\right)\left(b/t\right)^2} \qquad (2)$$

where

σ_c = critical stress, ksi
k = buckling coefficient
E = modulus of elasticity, ksi
v = Poisson's ratio
b = plate width, in.
t = plate thickness, in.

For plates in pure compression with both non-loaded edges simply supported, $k = 4.00$. For plates in pure compression with one non-loaded edge simply supported and one free, $k = 0.425$.

Gerard and Becker (1957) presented equations for plates of finite length with simple supports at the loaded edges. For plates with one non-loaded edge simply supported and one free,

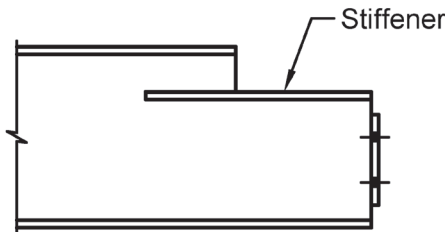$$k = \frac{6}{\pi^2}\left[1 - v + \frac{\left(\pi b / \lambda\right)^2}{6}\right] \qquad (3)$$

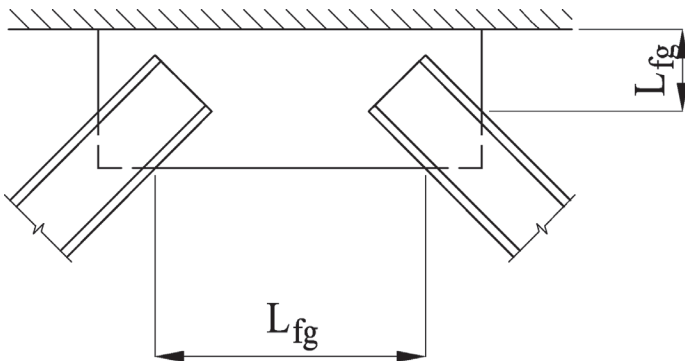Fig. 2. Coped beam with a stiffened edge.

Fig. 3. Free length of gusset plate edges.

where

λ = a/m
a = plate length, in.
m = integer that gives the lowest k

For plates with both non-loaded edges simply supported

$$k = \left(\frac{\lambda}{b} + \frac{b}{\lambda}\right)^2 \qquad (4)$$

Stiffener Requirements

Timoskenko and Gere (1961) solved the differential equation for a plate supported on both non-loaded edges by an elastic beam and provided a graphical solution for various values of beam stiffness. The CRC *Handbook of Structural Stability* (CRC, 1971) provides graphical solutions for plates simply supported on three edges and stiffened on one non-loaded edge. The curves indicate that the stiffener requirements increase as the aspect ratio of the plate increases.
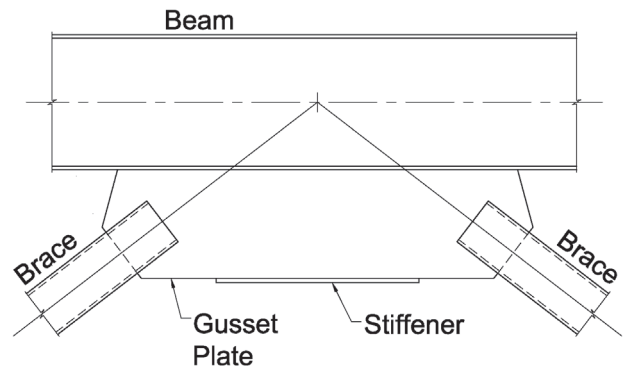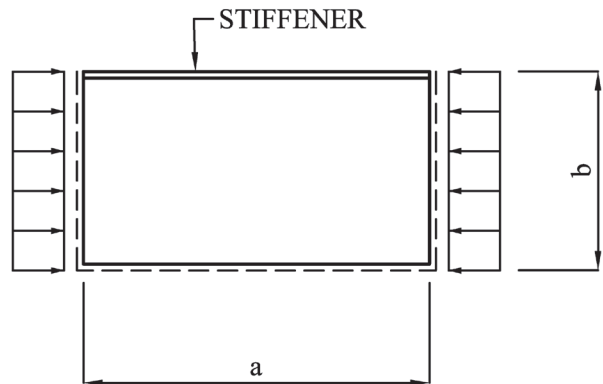

Fig. 4. Gusset plate with a stiffened edge.

Fig. 5. Model used for finite element analysis.

Table 1. Critical Stress for Models with b = 25 in., ksi												
Model	a, in.	Stiffener Moment of Inertia, I, in.⁴										
		0	1.254	2.508	5.017	10.03	15.05	20.07	30.10	40.14	60.20	Infinite
25-1	12.50	187.6	253.6	268.1	274.6	278.1	279.5	280.2	281.1	281.6	282.2	286.0
25-2	18.75	91.56	140.4	162.3	178.1	187.4	190.9	192.9	–	–	–	185.4
25-3	25.00	59.04	91.68	115.8	141.6	161.2	169.0	173.3	178.0	180.6	183.5	195.0
25-4	50.00	27.96	35.46	45.36	63.28	93.44	117.9	138.4	170.0	184.0	187.7	212.1

Table 2. Critical Stress for Models with b = 35 in., ksi												
Model	a, in.	Stiffener Moment of Inertia, I, in.⁴										
		0	1.880	3.760	7.521	15.04	22.56	30.08	45.13	60.17	90.25	Infinite
35-1	17.50	94.49	129.5	134.5	137.3	139.0	139.6	140.0	140.5	140.7	141.0	142.8
35-2	26.25	46.57	73.49	82.37	90.69	94.89	96.51	97.40	–	–	–	93.83
35-3	35.00	30.06	49.11	61.34	73.60	82.40	85.94	87.89	90.03	91.26	92.69	102.3
35-4	70.00	14.28	19.27	25.01	35.37	52.23	65.66	76.40	91.14	92.57	94.29	105.7

Table 3. Critical Stress for Models with b = 45 in., ksi												
Model	a, in.	Stiffener Moment of Inertia, I, in.⁴										
		0	2.480	4.961	9.921	19.84	29.76	39.68	59.53	79.37	119.1	Infinite
45-1	22.50	56.78	77.93	80.76	82.38	83.33	83.71	83.93	84.18	84.36	84.53	85.56
45-2	33.75	28.09	44.87	50.64	54.64	57.04	57.98	58.49	–	–	–	56.47
45-3	45.00	18.16	30.36	37.69	44.76	49.78	51.78	52.87	54.11	54.82	55.64	61.09
45-4	90.00	8.644	12.04	15.74	22.40	33.16	41.49	47.93	54.62	55.42	56.40	62.84

According to Caltrans (2001), the moment of inertia of a gusset plate stiffener should be the largest of:

$$I_s = 1.83t^4 \sqrt{(b/t)^2 - 144} \qquad (5)$$

$$I_s = 9.2t^4 \qquad (6)$$

These equations were originally specified in the 1962 edition of the *Specification for the Design of Light Gage Cold-Formed Steel Structural Members* (AISI, 1962) to provide a minimum stiffness for bracing the edge of an infinitely-long plate element within a member. The 1996 AISI *Specification* (AISI, 1997) has a more refined approach which is based on the research of Desmond et al. (1981), and Pekoz (1986). The newer provisions account for the post-buckling strength as well as the critical buckling capacity, and provide a method to calculate the effect of partially effective stiffeners.

FINITE ELEMENT MODELS

The study consisted of 123 models with width-to-thickness ratios, b/t, of 25, 35 and 45. The aspect ratios, a/b, were 0.50, 0.75, 1.00 and 2.00, and each of the 12 base model geometries were modeled with various stiffener sizes as shown in Tables 1, 2 and 3.

Figure 5 shows the loading and edge conditions for the finite element models. The simply supported edges, designated with dashed lines in Figure 5, were modeled with out-of-plane translation fixed and all three rotational degrees of freedom free. The stiffener was centered on the plate and a uniform axial stress was applied parallel to the stiffened edge. The modulus of elasticity was 29,000 ksi, and Poisson's ratio was 0.3.

The finite element program used for the buckling analysis is BASP, which was developed at the University of Texas at

Austin. The program uses a two-dimensional idealization. The analysis is performed in two steps. First, the in-plane analysis is performed to calculate the stresses arising from the applied loading. Using these stresses, an out-of-plane analysis is performed to solve for the critical buckling load. The program provides an elastic solution and does not account for pre-buckling deformations or initial out-of-flatness of the plate. The program is described in more detail in Akay et al. (1977).

The accuracy of the models were verified by comparing the critical loads from the program to the theoretical critical loads for the case where the plate has one non-loaded edge free and the remaining edges simply supported. The theoretical critical loads were calculated using Equation 2 with the buckling coefficient, k, from Equation 3. The critical loads from the finite element models were obtained using a 2.5-in. square mesh. Calculations were carried out for each of the 12 base model geometries used in this study and the ratio of BASP load to theoretical load varied from 0.98 to 1.01. Therefore, the 2.5-in. mesh size is adequate to capture the critical loads in sufficient accuracy and the remaining models used a maximum mesh size of 2.5-in.

RESULTS

The effect of stiffener moment of inertia on the critical load of the plates is shown in Tables 1, 2 and 3. The results are plotted in Figures 6, 7 and 8 for the models with plate width-to-thickness ratios, b/t, of 25, 35 and 45, respectively. The critical stress versus stiffener moment of inertia curves are nonlinear, and in each case, the plots show that the stiffener moment of inertia reaches a critical value where a further increase in stiffness provides only marginal gains in the critical buckling stress of the plate.
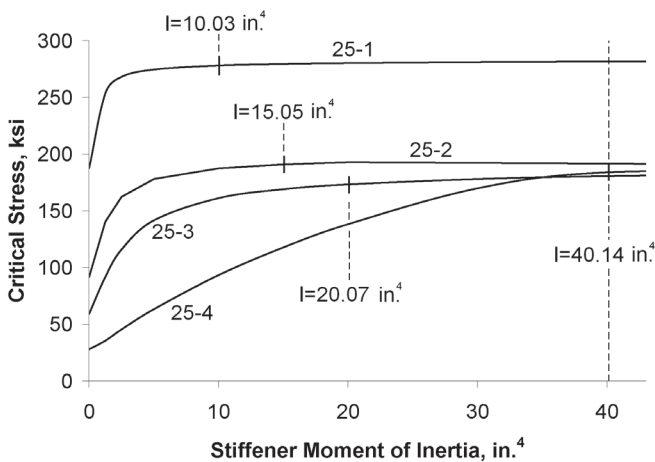
The sharp knee on the curves in Figures 6, 7 and 8 indicate the point where the plate buckling shape changed from the classical unstiffened mode to the stiffened mode. This can be seen by observing the buckled shapes of model 35-4 in Figures 9, 10 and 11, which show the effect of the stiffener moment of inertia on the buckled shape. Figure 9 shows that a stiffener with a moment of inertia of 1.88 in.[4] does not restrain the lateral translation at the stiffened edge adequately. In Figure 10, the model with $I = 60.17$ in.[4], shows some lateral translation at the stiffened edge, but the stiffener's moment of inertia was large enough to alter the buckled shape. When the moment of inertia of the stiffener is increased to 90.25 in.[4], Figure 11 shows the lateral translation at the stiffened edge is very small; however, the critical stress was only about 2% higher than for the specimen with $I = 60.17$ in.[4]
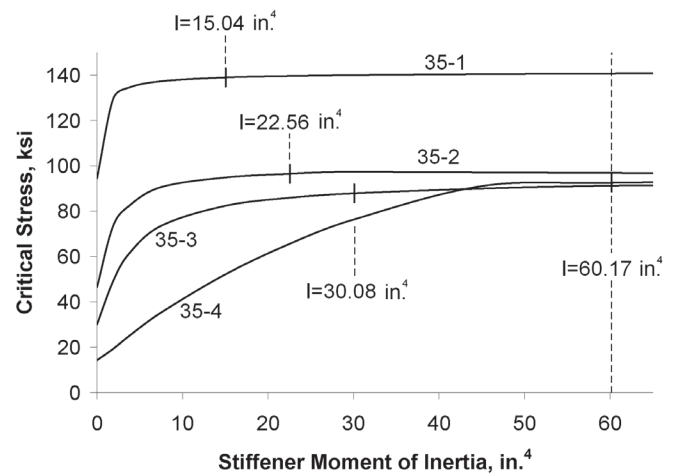

Fig. 7. Critical stress versus stiffener moment of inertia for models with b/t = 35.

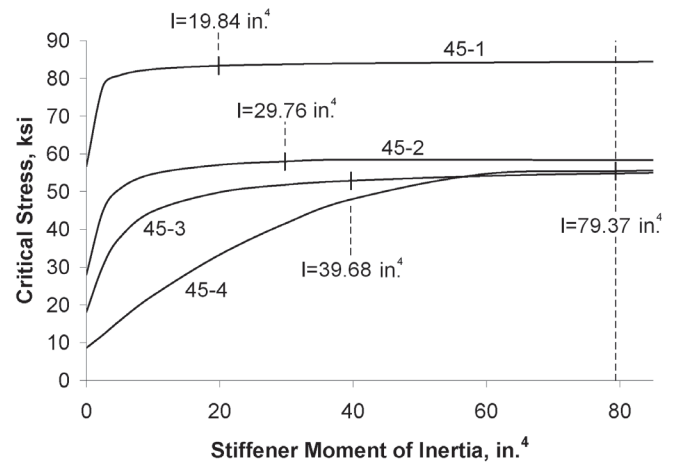Fig. 6. Critical stress versus stiffener moment of inertia for models with b/t = 25.

Fig. 8. Critical stress versus stiffener moment of inertia for models with b/t = 45.

PROPOSED DESIGN METHOD

For use in design, a critical stiffener moment of inertia must be determined that, if exceeded, will be adequate to brace the plate against buckling in an unstiffened mode. Proposed stiffness requirements should produce critical loads in the plate approximately equal to the case of infinite stiffness. This occurs at the transition point where the plate buckling shape changes from the classical unstiffened mode to the stiffened mode. To meet this objective, the Caltrans (2001) requirements can be modified to account for the plate aspect ratio. A simple design equation can be obtained by multiplying I_s from Equation 5 by the aspect ratio, and dividing by 2, which gives

$$I_c = \left(\frac{a}{b}\right)\left(\frac{I_s}{2}\right) \tag{7}$$

Equation 6 controls the design only for connections with $b/t < 13$, which is much stockier than most connection elements; therefore, it will not be considered further in this paper. Substituting Equation 5 into Equation 7, the final equation is

$$I_c = 0.92\left(\frac{a}{b}\right)t^4\sqrt{\left(\frac{b}{t}\right)^2 - 144} \tag{8}$$

This equation should only be used for aspect ratios between ½ and 2. For an aspect ratio of 2, it gives the same results as Equation 5.

The critical moment of inertia calculated with Equation 8 is indicated in Figures 6, 7 and 8 with a vertical line for each of the 12 base model geometries. In each case, the calculated critical moment of inertia is at a location on the curve beyond the sharp knee, where the rate of change is low, indicating
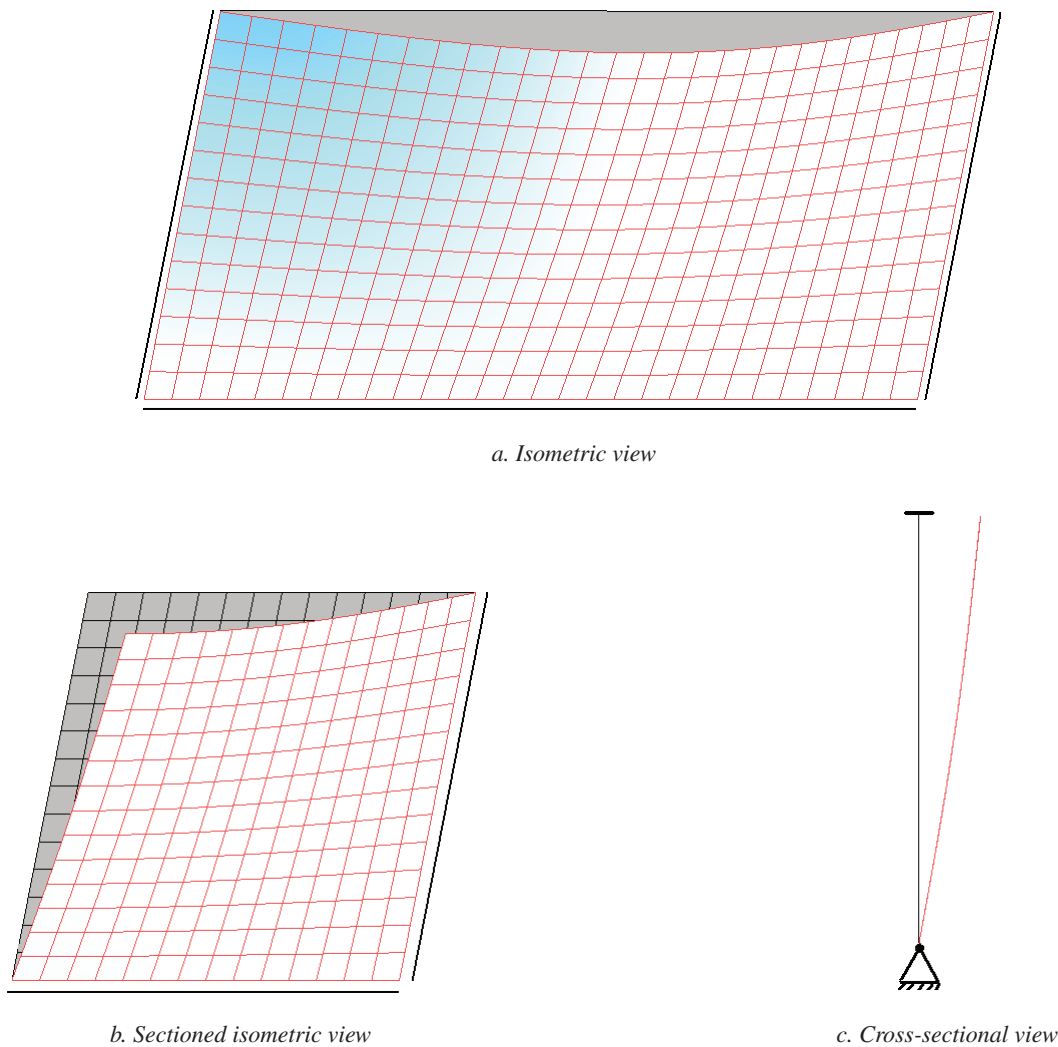

a. Isometric view

b. Sectioned isometric view

c. Cross-sectional view

Fig. 9. Buckled shape for Model 35-4 with stiffener I = 1.880 in.⁴.

that the buckled shape has transitioned from an unstiffened mode to a stiffened mode. Once the stiffener critical moment of inertia is reached, additional stiffness provides only very small gains in the critical stress of the plate. In Tables 1, 2 and 3, the values to the right of the heavy line are for models with stiffeners that meet or exceed the stiffness requirements of Equation 8.

CONCLUSION

For an edge stiffener to be effective, it must have adequate flexural stiffness to alter the buckled shape of the plate. The results from 123 elastic finite element models were analyzed to determine the stiffness requirements for edge stiffeners with aspect ratios between ½ and 2. The parameters studied were the width-to-thickness ratio and the aspect ratio of the braced element.

Equation 8 was proposed as a simple method to calculate the minimum stiffener moment of inertia required to brace connection elements against buckling in an unstiffened mode. Use of the proposed equation should be limited to the range of aspect ratios studied. At aspect ratios larger than two, Equation 5 should be used.

The design procedure outlined in this paper was based on a simplified model that does not include many factors that are present in real structures. Some of these factors are initial out-of-flatness of the element/stiffener assembly, residual stresses and inelastic material behavior, non-idealized boundary conditions, and non-uniform stress distribution in the braced element. Further research is needed to quantify the effects of these items; therefore, sound judgment is required when applying the proposed design procedure.

ACKNOWLEDGMENTS

a. Isometric view

b. Sectioned isometric view

c. Cross-sectional view

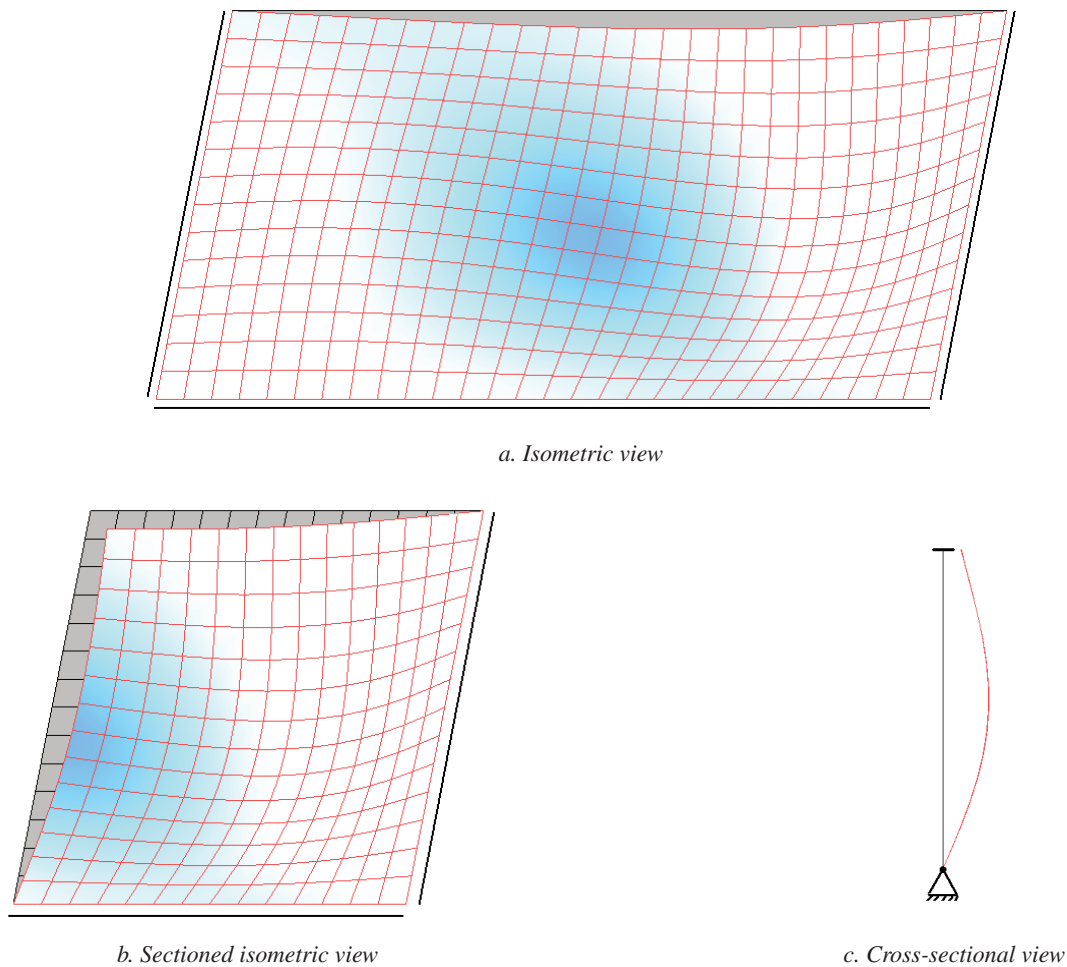*Fig. 10. Buckled shape for Model 35-4 with stiffener* $I = 60.17$ in.^{4}.

REFERENCES

AASHTO (2004), *LRFD Bridge Design Specifications*, 3rd Ed., American Association of State Highway and Transportation Officials, Washington, DC.

AISC (2006), *Seismic Design Manual*, American Institute of Steel Construction, Chicago, IL.

AISC (2005), *Steel Construction Manual*, American Institute of Steel Construction, Chicago, IL.

AISI (1997), *Specification for the Design of Cold-Formed Steel Structural Members*, American Iron and Steel Institute, Washington, DC.

AISI (1962), *Specification for the Design of Light Gage Cold-Formed Steel Structural Members*, American Iron and Steel Institute, New York, NY.

Akay, H.U., Johnson, C.P. and Will, K.M. (1977), "Lateral and Local Buckling of Beams and Frames," *Journal of the Structural Division*, ASCE, Vol. 103, No. ST9, September, pp. 1821–1832.

Astaneh, A. (1998), "Seismic Behavior and Design of Gusset Plates," *Steel Tips*, Structural Steel Educational Council, December.

Caltrans (2001), *Guide Specifications for Seismic Design of Steel Bridges*, State of California Department of Transportation, December.

CRC (1971), *Handbook of Structural Stability*, Column Research Committee of Japan, Corona Publishing Company, Tokyo.
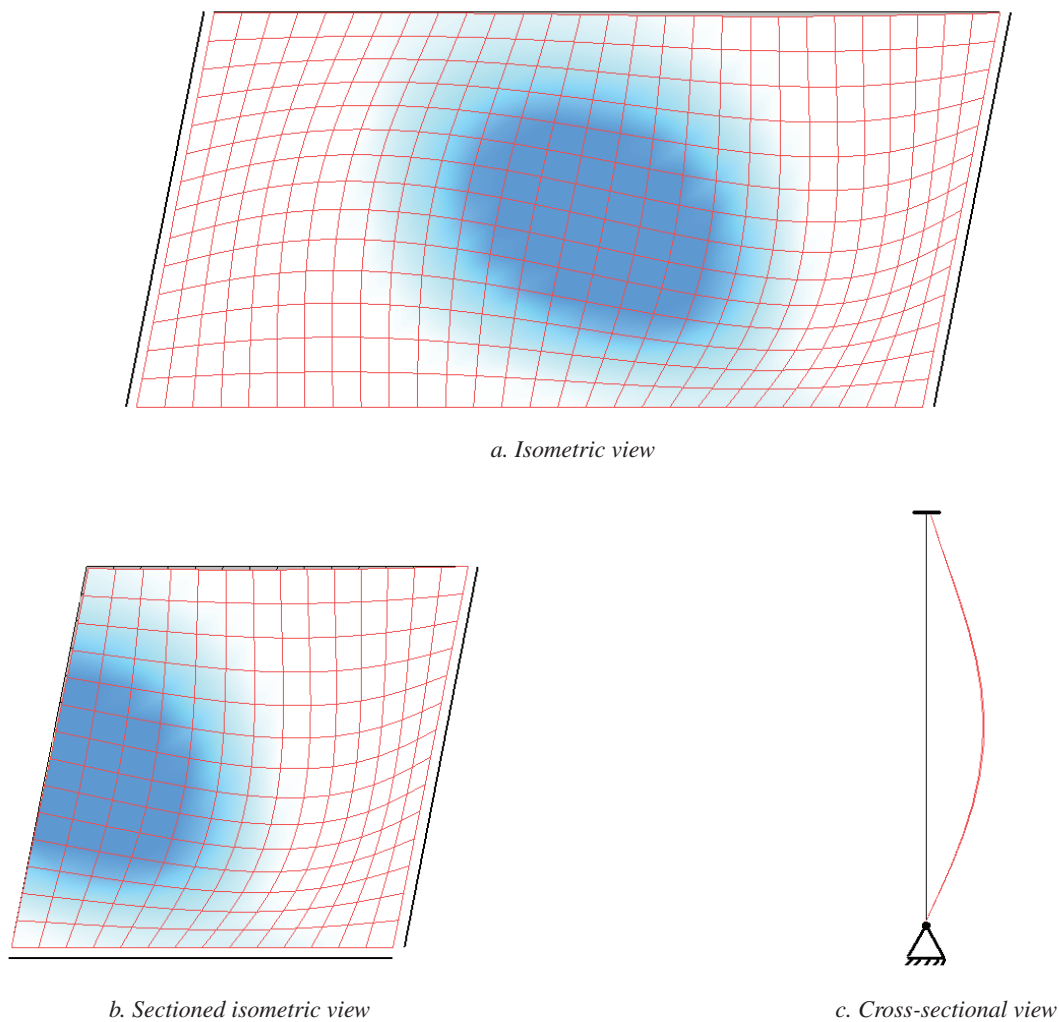
a. Isometric view

b. Sectioned isometric view

c. Cross-sectional view

Fig. 11. Buckled shape for Model 35-4 with stiffener $I = 90.25$ in.^{4}.

Desmond, T.P., Pekoz, T. and Winter, G. (1981), "Edge Stiffeners for Thin-Walled Members," *Journal of the Structural Division*, ASCE, Vol. 107, No. ST2, February, pp. 329–353.

Galambos, T.V. (1998), *Guide to Stability Design Criteria for Metal Structures*, 5th Ed., John Wiley and Sons.

Gerard, G. and Becker, H. (1957), *Handbook of Structural Stability: Part I—Buckling of Flat Plates*, Technical Note 3781, National Advisory Committee for Aeronautics, Washington, DC.

Nast, T.E., Grondin, G.Y. and Cheng, J.J.R. (1999), "Cyclic Behavior of Stiffened Gusset Plate Brace Member Assemblies," University of Alberta, Department of Civil and Environmental Engineering, Structural Engineering Report No. 229, December.

Pekoz, T. (1986), *Development of a Unified Approach to the Design of Cold-Formed Steel Members*, Report SG 86-4, American Iron and Steel Institute, Washington, DC.

Rabinovitch, J. and Cheng, J.J.R. (1993), "Cyclic Behavior of Steel Gusset Plate Connections," University of Alberta Department of Civil Engineering, Structural Engineering Report No. 191, August.

Reno, M. and Duan, L. (1997), *San Francisco—Oakland Bay Bridge West Spans Seismic Retrofit Design Criteria,* State of California Department of Transportation, January 31.

Timoshenko, S.P. and Gere, J.M. (1961), *Theory of Elastic Stability*, McGraw-Hill, New York, NY.

Behavior of Vertical Boundary Elements in Steel Plate Shear Walls

BING QU and MICHEL BRUNEAU

ABSTRACT

The AISC *Seismic Provisions* and CSA S-16 Standard require a minimum moment of inertia for the vertical boundary elements (VBEs) in steel plate shear walls (SPSWs) to avoid undesirable VBE behaviors. The equation limiting VBE flexibility has been derived from a flexibility factor, ω_t, developed in plate girder theory and the limit on VBE flexibility has been empirically specified based on previous test results. This paper reviews the derivations of the flexibility factor and how that factor was incorporated into current code design requirements for SPSWs. Then, analytical models to prevent VBE shear yielding and to estimate the out-of-plane buckling strength of VBE are developed, followed by a review of past experimental data to investigate if the significant inward VBE inelastic deformation and out-of-plane buckling observed in some instances were due to excessive VBE flexibilities or other causes such as shear yielding at the ends of the VBEs. It is shown that the existing limit on ω_t is uncorrelated to satisfactory in-plane and out-of-plane VBE performance. The proposed analytical models predict performance of previously tested SPSWs that correlates well with the experimental observations.

Keywords: steel plate shear walls, vertical boundary elements, shear yielding, out-of-plane buckling.

A typical steel plate shear wall (SPSW) such as the one shown in Figure 1 consists of infill steel panels surrounded by columns, called vertical boundary elements (VBEs), on each side, and beams, called horizontal boundary elements (HBEs), above and below. These infill panels are allowed to buckle in shear and subsequently form diagonal tension fields when resisting lateral loads. Energy dissipation of SPSW during seismic events is principally achieved through yielding of the panels along the diagonal tension fields (Sabelli and Bruneau, 2007). Consistent with capacity design principles, the Canadian Standard S16 on *Limit States Design of Steel Structures* (CSA, 2001) and the AISC *Seismic Provisions for Structural Steel Buildings* (AISC, 2005c) require HBEs and VBEs to be designed to remain elastic when the infill panels are fully yielded, with the exception of plastic hinges at the ends of HBEs and at the VBE bases that are needed to develop the expected plastic mechanism of the wall when rigid HBE-to-VBE and VBE-to-ground connections are used. The procedures to achieve capacity design of the boundary frame of SPSWs have been presented by Berman and Bruneau (2008), Vian and Bruneau (2005),

Qu and Bruneau (2008). Using the knowledge on capacity design, as well as building on findings from a recent study of HBEs that provided new insights on the design demands and capacities to consider for their design (Qu and Bruneau, 2008), a study was undertaken to reassess demands on VBEs, and the relevance in that context of existing provisions that limit VBE flexibility.

The early Canadian provisions for SPSWs (i.e., CSA Standard S16-94 [CSA, 1994]) required VBEs to be designed as beam-column using a conventional strength-based approach. This approach was challenged by the results of tests on quarter-scale SPSW specimens by Lubell et. al (2000), in which the VBEs designed using the strength-based approach

Bing Qu, Ph.D., Assistant Professor, Department of Civil and Environmental Engineering, California Polytechnic State University, One Grand Ave., San Luis Obispo, CA 93407 (corresponding author). E-mail: bqu@calpoly.edu

Michel Bruneau, Ph.D., P.Eng., Professor, Department of Civil, Structural and Environmental Engineering, University at Buffalo, 130 Ketter Hall, Buffalo, NY 14260. E-mail: bruneau@buffalo.edu

Fig. 1. Typical steel plate shear wall and analogous vertical cantilever plate girder.

exhibited significant "pull-in" deformation or undesirable premature out-of-plane buckling. In a subsequent discussion of the Lubell et al. SPSW specimens, Montgomery and Medhekar (2001) attributed this poor performance to insufficient VBE stiffness, and that rationale was accepted in the development of CSA-S16 provisions. If VBEs deform excessively, they may be unable to anchor the infill panel yield forces. A non-uniform diagonal tension field may then develop and affect the VBEs inconsistently to the design assumptions.

To ensure adequately stiff VBEs, CSA S16-01 (CSA, 2001) introduced the flexibility factor, ω_t, proposed in previous analytical work of plate girder theory, as an index of VBE flexibility. Please note that this flexibility factor, ω_t, is different from the other symbol, ω, which is used in the later sections of this paper for denoting the distributed infill panel forces. Noting that the Lubell et al. specimens had flexibility factors of 3.35, and that all other known tested SPSWs that behaved in a ductile manner had flexibility factors of 2.5 or less, CSA S16-01 empirically specified an upper bound of 2.5 on ω_t. Note that this requirement can be converted into the VBE flexibility requirement presented in the current design codes as demonstrated later.

In design, the intent is that the aforementioned flexibility limit prevents excessively slender VBE. However, beyond the empirical observations and analogy to plate girder theory, no work has investigated whether the significant inward inelastic deformations of VBEs observed in past tests were directly caused by excessive VBE flexibilities or due to other causes, such as shear yielding at the ends of VBEs. In addition, no theoretical research has established a relationship between ω_t and the out-of-plane buckling strength of VBE as part of SPSW behavior.

To better understand the preceeding issues, in this paper, derivation of the flexibility factor in plate girder theory is first reviewed, followed by the description of how that factor was incorporated into the current design codes. Then, analytical models for preventing VBE shear yielding and for estimating the out-of-plane buckling strength of VBEs are developed. Finally, results from some previously tested SPSWs are revisited and assessed to validate the proposed analytical models.

REVIEW OF FLEXIBILITY FACTOR IN PLATE GIRDER THEORY

In the SPSW literature, SPSWs are often described like cantilever vertical plate girders. Using this analogy, the story height and bay width of a SPSW are analogous to the stiffener spacing and the depth of a plate girder, respectively, as shown in Figure 1. Note that this analogy has only qualitative merits in providing a conceptual understanding of the VBE behavior in a SPSW. Berman and Bruneau (2004) have identified that many significant differences exist in the strengths and behavior of these two systems.

Nonetheless, plate girder studies provided the theoretical framework from which Equation 1 that will be introduced in detail later was originally derived. The CSA S16-01 and the AISC *Seismic Provisions* reference Wagner's analytical studies (Wagner, 1931) on the elastic behavior of girders with thin metal webs subjected to transverse shear, where a method for determining the minimum moments of inertia of flanges to ensure a sufficiently uniform tension field across the web plate has been developed. Since that method is the one underlying the current flexibility limit for VBE design, a brief review of that study is presented here. The symbols used in the original work have been changed to fit the nomenclatures used for SPSW design.

Wagner's analysis postulated that the deformation of a cantilever plate girder of elastic behavior under transverse load can be schematically shown as in Figure 2. The subscripts o and u are assigned to the variables corresponding to the top and bottom flanges, respectively. As shown in Figure 2, plate girder flange deformation is obtained by superposing two effects, namely, global deflection of the plate girder due to transverse load, represented by δ, and local deflections of the flanges between neighboring stiffeners due to elastic web tension actions, represented by η_u and η_o. In Figure 2, L is the depth of the plate girder; and α is the inclination of infill tension actions.

Uniformity of the tension field across the web plate of the girder depends on the flexibility of flanges. To better understand this, consider the effect of a single tension diagonal, which is denoted by line "*uo*" in Figure 2. When the flanges are flexible and develop inward deflections (i.e., η_u and η_o shown in Figure 2) due to the web plate forces, the elongation of *uo* decreases, compared to the case when rigid flanges would be present, as a result of deformation compatibility. Note that this effect varies along the flanges (i.e., the elongations of tension diagonals at different locations are different), resulting in uneven tension fields across the web plate.
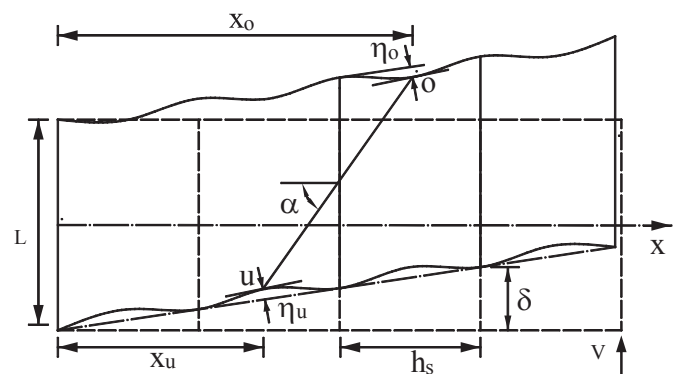

Fig. 2. Deformation of a cantilever plate girder under transverse load (adapted from Wagner, 1931).

For flanges infinitely rigid in bending, there would be no local deflections of flanges between neighbouring stiffeners, resulting in a uniform tension field across the web plate.

Modeling each flange of the plate girder as a continuous beam on elastic foundations, and accounting for the real load distribution along each flange, which can be determined by superposing the uniform load obtained assuming that the flanges are infinitely rigid and the loss of this uniform load due to flange flexibility, Wagner (1931) derived the following governing equation for the local flange deflections:

$$\frac{d^4(\eta_u - \eta_o)}{dx^4} = \left(\frac{1}{I_u} + \frac{1}{I_o}\right) t_{wi} \sin^2 \alpha \varepsilon_g$$
$$- \left(\frac{1}{I_u} + \frac{1}{I_o}\right) \frac{t_{wi} \sin^4 \alpha}{L} (\eta_u - \eta_o)$$

(1)

where
  η_u = deflection of the bottom flange due to web tension actions
  η_o = deflection of the top flange due to web tension actions
  I_u = moment of inertia of the bottom flange
  I_o = moment of inertia of the top flange
  α = inclination angle of the web plate tension action
  t_{wi} = web plate thickness
  L = depth of the plate girder which corresponds by analogy to the width of a SPSW
  ε_g = strain in the tension diagonals assuming that the flanges are rigid

Equation 1 is a fourth-order ordinary differential equation and can be solved for $(\eta_u - \eta_o)$ using classic procedures. The maximum value of $(\eta_u - \eta_o)$, which corresponds to the maximum loss of the of tension diagonal elastic elongation (i.e., an index of the maximum loss of the elastic uniform load along the flanges), is:

$$(\eta_u - \eta_o)_{max} =$$

(2)

$$\frac{\varepsilon_g L}{\sin^2 \alpha} \left(1 - \frac{\sin\left(\frac{\omega_t}{2}\right)\cosh\left(\frac{\omega_t}{2}\right) + \cos\left(\frac{\omega_t}{2}\right)\sinh\left(\frac{\omega_t}{2}\right)}{\sin\left(\frac{\omega_t}{2}\right)\cos\left(\frac{\omega_t}{2}\right) + \sinh\left(\frac{\omega_t}{2}\right)\cosh\left(\frac{\omega_t}{2}\right)} \right)$$

where
  ω_t = flexibility factor, defined as:

$$\omega_t = h_{si} \sin \alpha \sqrt[4]{\left(\frac{1}{I_u} + \frac{1}{I_o}\right) \frac{t_{wi}}{4L}}$$

(3)

where
  h_{si} = spacing between neighboring stiffeners in a plate girder (which corresponds by analogy to story height of a SPSW).

As explicitly expressed in Equation 3, increasing the flange stiffness of a plate girder (i.e., increasing I_u and I_o) would decrease the corresponding flexibility factor for given values of the other terms.

To assess the uniformity of the web tension field, a stress uniformity ratio, $\sigma_{mean}/\sigma_{max}$, was proposed and calculated as:

$$\frac{\sigma_{mean}}{\sigma_{max}} = \left(\frac{2}{\omega_t}\right) \left[\frac{\cosh(\omega_t) - \cos(\omega_t)}{\sinh(\omega_t) + \sin(\omega_t)}\right]$$

(4)

where
  σ_{mean} = mean of the web tension force components parallel with the stiffener
  σ_{max} = maximum of the web tension force components parallel with the stiffener

The relationship between the stress uniformity ratio (i.e., $\sigma_{mean}/\sigma_{max}$) and the flexibility factor (i.e., ω_t) is shown in Figure 3. As shown on that curve, for smaller values of ω_t (e.g., in the range $0 \le \omega_t \le 1$), for which the plate girder has relatively stiff flanges, the stress uniformity ratio approximately equals 1 (which physically means that the maximum stress is close to the average stress), indicating development of a uniform web tension field. However, with increases in the flexibility factor, the stress uniformity ratio decreases, indicating formation of a less uniform web tension field in plate girders having more flexible flanges.
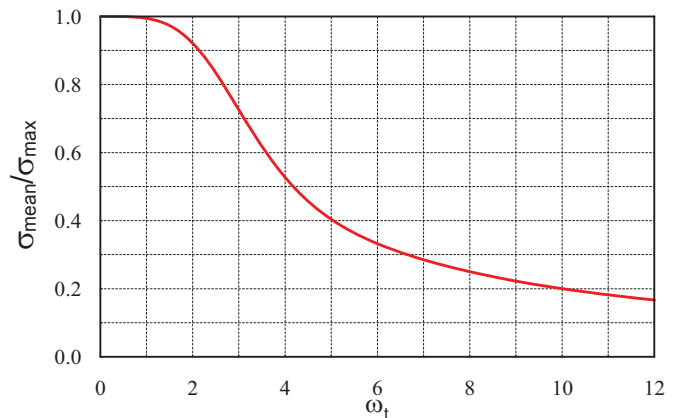

Fig. 3. Relationship between flexibility factor and stress uniformity ratio.

For simplicity, Kuhn, Peterson and Levin (1952) simplified Equation 3, by assuming $\alpha = 45°$, for which $\sin \alpha = 0.7$, and by substituting the approximate equivalency $\left(\dfrac{1}{I_u} + \dfrac{1}{I_o} \right) = \dfrac{4}{\left(I_u + I_o \right)}$, to obtain:

$$\omega_t \approx 0.7 h_s \sqrt[4]{\frac{t_{wi}}{\left(I_u + I_o \right) L}} \qquad (5)$$

Kuhn et al. (1952) proposed the stress amplification factor, C_2, which can be determined from the following equation, to characterize the uniformity of elastic web tension field:

$$\sigma_{max} = (1 + C_2)\sigma_{mean} \qquad (6)$$

As expressed in Equation 6, the stress amplification factor, C_2, captures the difference between σ_{max} and σ_{mean}. Large value of C_2 corresponds to a significant difference between σ_{max} and σ_{mean}, indicating the formation of a less uniform web tension field. Solving for C_2 with respect to the stress uniformity ratio (i.e., $\sigma_{mean}/\sigma_{max}$) from Equation 6 and recalling Equation 4, the relationship between C_2 and ω_t can be obtained and is illustrated in Figure 4. Consistent with Figure 3, the curve shown in Figure 4 indicates that a less uniform tension field (which corresponds to greater C_2) will develop in a plate girder with more flexible flanges (which corresponds to greater ω_t).

FLEXIBILITY LIMIT FOR VBE DESIGN

To quantify the minimum flexural stiffness of VBE needed to ensure uniformity of elastic infill tension fields in SPSWs and avoid the undesirable VBE behaviors described previously, CSA S16-01 adopted Equation 5. Provided that each VBE has the same moment of inertia, I_c, as normally the case in SPSWs, Equation 5 becomes:

$$\omega_t = 0.7 h_{si} \sqrt[4]{\frac{t_{wi}}{2 I_c L}} \qquad (7)$$

For the reasons described earlier, and on the strength of the information provided by Montgomery and Medhekar (2001), the CSA S16 limited this factor to a maximum value of 2.5. This limit of 2.5 was also selected on the assumption that tension fields should be sufficiently uniform for ductile behavior to develop. In Figure 4, limiting the flexibility factor to a value of 2.5 is shown to correspond to a maximum stress not exceeding by more than 20% the average stress of the web tension field. Imposing the upper bound of 2.5 on Equation 7 and solving for I_c leads to the following requirement, first implemented in the CSA S16-01:

$$I_c \geq \frac{0.00307 t_{wi} h_{si}^{\;4}}{L} \qquad (8)$$

The requirement was subsequently adopted in the National Earthquake Hazards Reduction Program (NEHRP) *Provisions for Seismic Regulations for New Buildings and Other Structures,* also known as FEMA 450 (FEMA, 2003), and then the AISC *Seismic Provisions* (AISC, 2005c).

Note that the analytical work by Wagner (1931) and Kuhn et al. (1952) for plate girders, which was used for determination of the VBE flexibility limit, assumed elastic behavior. Although at the onset of the tension field action, the maximum stress in an infill panel may be significantly greater than the average due to VBE deflections, this difference could decrease upon greater story drifts, provided that the boundary frame members are able to allow infill panel stress redistribution after the first yielding of tension diagonals. To better understand this, stress distributions across the first-story web plates (i.e., along the direction perpendicular to the tension diagonals) are shown in Figure 5 for two tested specimens, namely, the specimen tested by Driver et al. (1998) and the specimen tested by Lee and Tsai (2008). Note that these two specimens have different flexibility factors and will be introduced in more detail in a later section. Figure 5 shows that, as drift levels progressively increase, both specimens will ultimately develop uniform tension fields, although the specimen tested by Lee and Tsai (which had more flexible VBEs) develops less uniform tension fields at lower drift levels. Since identical uniform stress distribution ultimately develop in the panels of SPSW, the issue of initial stress distribution seems irrelevant to the performance of SPSW. By inference, this raises questions about the relevance of considering a flexibility factor altogether, ω_t, in SPSW design. Therefore, different models are investigated in the next sections to rationalize desirable and undesirable VBE behaviors.
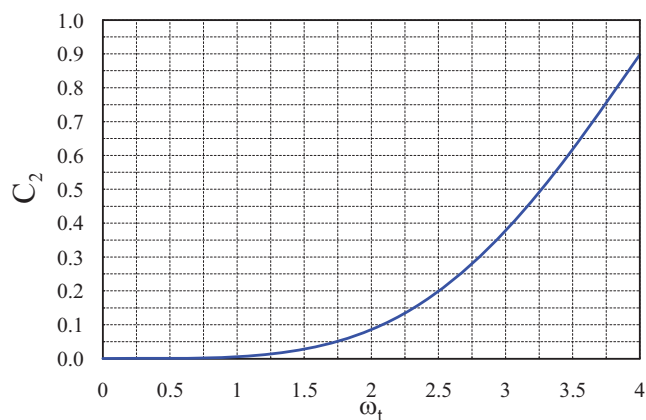

Fig. 4. Relationship between flexibility factor and stress amplification factor.

PREVENTION OF VBE IN-PLANE SHEAR YIELDING

As mentioned earlier, the significant "pull-in" deformation of VBE observed during the tests on single-story SPSWs by Lubell et al. (2000) as shown in Figure 6 was a milestone event that led to the current limit specified for the flexibility of VBEs in SPSWs (AISC, 2005c; CSA, 2001). This undesirable performance was ascribed to the insufficient VBE stiffness (Montgomery and Medhekar, 2001). However, VBE shear yielding is another important factor that may result in significant inelastic VBE deflections. At the

time of this writing, no literature has reported or checked whether the previously tested specimens have encountered VBE shear yielding.

To have a better understanding of the observed significant inward deformations in VBEs, an analytical model for estimating VBE shear demand is proposed in this section followed by assessment on the previously tested SPSWs using the proposed analytical model. For comparison purpose, results from pushover analysis on strip models of those considered SPSWs are also provided. Predictions are compared with the observed behavior.
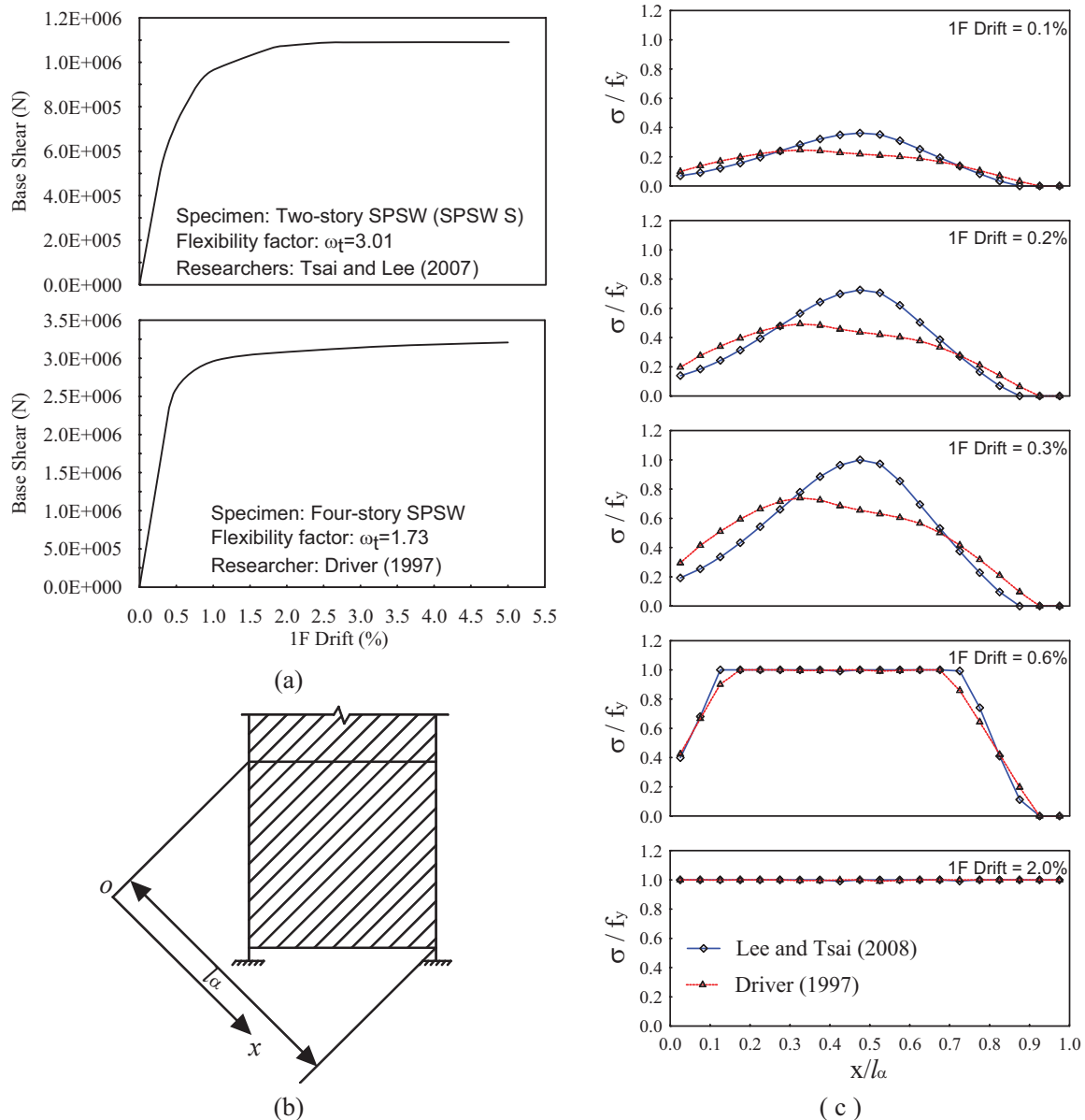

Fig. 5. Uniformity of tension fields: (a) pushover curves; (b) schematic of tension fields; (c) uniformity of panel stresses in strip models.

SHEAR DEMAND AND STRENGTH OF VBE

According to the current design codes, VBEs of a SPSW, which are sized as beam-column members (i.e., considering the P-M interaction demands), are required to remain elastic when the webs are fully yielded, with exception of plastic hinges at the VBE bases when VBEs are fixed to ground. Although not explicitly stated, those plastic hinges should be flexural-plastic hinges (i.e., as opposed to shear-yielding hinges) for the infill panels to be effectively anchored and consequently allow development of the expected tension fields. Note that the shear demands in VBEs can be of significant magnitude. One major contribution to the shear demands is due to yielding of the infill plate (incidentally this contribution produces equal and opposite shears in the opposing VBEs and thus do not contribute to the total story shear resisted). The free-body diagram of Figure 9 (explained later in this paper) for which equilibrium is explained in Berman and Bruneau (2008) is typically used to calculate these shear forces. When the resulting VBE shear demands are greater than their shear strengths, VBEs exhibit undesirable shear yielding behavior resulting in the significant pull-in deformation in VBEs as observed in some prior experimental research.

As shown in Figure 7, the free body diagram of the right-hand-side VBE at the ith story in a uniformly yielded single-bay SPSW under rightward lateral forces is used to determine the maximum VBE shear demand here. Note that the same VBE design shear force can be obtained for left-hand-side VBE based on the procedure presented later. Conservatively, assuming that the moments applied at the top and bottom ends of the VBE are equal to their expected nominal plastic moments, one can obtain the following estimate of VBE shear demand from equilibrium:

$$V_{u-design} = \frac{2R_y f_y Z_c}{h_{si}} + \frac{\omega_{xci} h_{si}}{2} + \frac{\omega_{yci} d_{ci}}{2} \qquad (9)$$
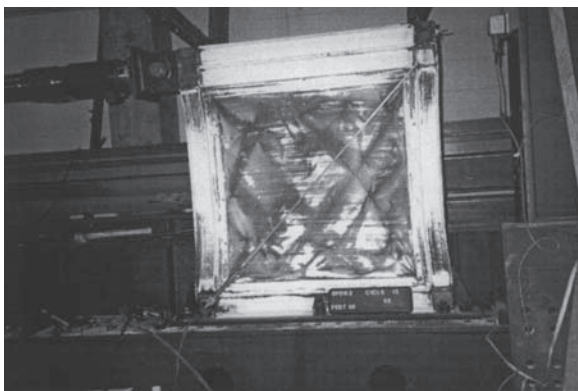
where

d_{ci}	=	VBE depth
Z_c	=	plastic section modulus of VBE
ω_{xci}	=	horizontal component of infill panel yield forces along VBE
ω_{yci}	=	vertical component of infill panel yield forces along VBE
f_y	=	yield stress of boundary frame
R_y	=	ratio of expected to nominal yield stress

Note that equations for calculating ω_{xci}, and ω_{yci} are available in Berman and Bruneau (2008).

It is recognized that Equation 9 overestimates the VBE shear design force for two reasons: (1) the plastic moments at the VBE ends may be reduced due to the presence of axial force, shear force and vertical stresses in the VBE (i.e., similar to the reduction of HBE plastic moments presented in Qu and Bruneau 2008); and (2) plastic hinges in properly designed SPSWs may develop in the HBEs, not in the VBEs. Note that for this case, the plastic moment of HBE may not necessarily distribute equally (½ and ½) between the columns above and below the connection due to higher mode effects. For expediency, it is conservative to design the columns to resist the shear force given by Equation 9, and acting concurrently with the corresponding axial force and moment. However, the true shear demand on columns may be less than given by Equation 9, and predicting the adequacy existing in SPSW VBEs using this procedure may incorrectly predict failure due to shear yielding (as will be the case for some tested SPSWs discussed in the following section).

In design, the shear demand obtained from Equation 9 should be compared to the VBE shear strength, V_n, which, when the VBE web is compact (i.e., when $h_{wci}/t_{wci} \leq 2.24\sqrt{E/f_y}$ per ANSI/AISC 360-05), is calculated as:
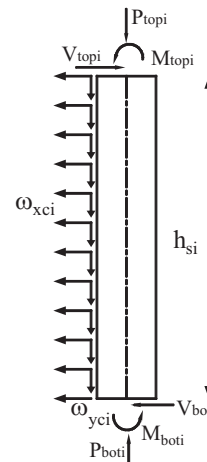

Fig. 6. Deformation and yield patterns of SPSW2 after $6\delta_y$ (Lubell et al., 2000).

Fig. 7. In-plane free body diagram of the VBE at the ith story for determination of shear demand.

								V_n	$V_{pushover}$	$V_{u-design}$	Shear
Case	Researcher	Specimen Identification	Number of Stories	Scale	Aspect Ratio[c] (L/h)	α (°)	ω_t	(kN)	(kN)	(kN)	Yielding
				(i) single-story specimen							
1	Lubell et al. (2000)	SPSW2	1	1:4	1.00	37.4	3.35	75	108	113	Yes
2	Berman and Bruneau (2005)	F2	1	1:2	2.00	44.8	1.01	932	259	261[d]	No
				(ii) multi-story specimen[a]							
3	Driver et al. (1998)	[b]	4	1:2	1.58	43.4	1.73	766	1361	1458	Yes
4	Park et al. (2007)	SC2T	3	1:3	1.46	44.4	1.24	999	676	1064	No
5		SC4T	3	1:3	1.46	44.1	1.44	999	984	1383	No
6		SC6T	3	1:3	1.46	43.9	1.58	999	1218	1622	Yes
7		WC4T	3	1:3	1.46	45.0	1.62	560	920	1210	Yes
8		WC6T	3	1:3	1.46	45.0	1.77	560	1151	1461	Yes
9	Qu et al. (2008)	[b]	2	1:1	1.00	41.3	1.95	2881	1591	2341	No
10	Lee and Tsai (2007)	SPSW N	2	1:1	0.66	38.8	2.53	968	776	955	No
11		SPSW S	2	1:1	0.66	36.5	3.01	752	675	705	No

Table 1. Evaluation of VBE Shear Demand and Strength[a]

[a] For multi-story specimens, VBEs at the first story are evaluated.
[b] Not applicable.
[c] Using the first-story height.
[d] The plastic moments applied at the VBE ends are equal to the strength of web–angle beam-to-column flexible connections.

$$V_n = 0.6 f_y d_{ci} t_{wci} \qquad (10)$$

where

h_{wci} = VBE web depth
t_{wci} = VBE web thickness
E = young's modulus

It should be noted that, for simplicity here, Equation 10 does not take into account the reduction effects on the VBE shear resistance due to the presence of other internal forces in VBEs and such a simplification may lead to a VBE design that is not conservative. However, when necessary, the interaction of these effects can be considered using a more rigorous procedure provided in Qu and Bruneau (2008).

OBSERVATION OF VBE SHEAR YIELDING IN PAST TESTING

To check whether VBE shear yielding had occurred in previous tests, a selection of SPSWs for which the experimental data are available is assessed in Table 1. Those examples include both single-story and multi-story SPSWs. Using the analytical model proposed in prior section, the shear demands (i.e., $V_{u-design}$) and strengths (i.e., V_n), respectively calculated using Equations 9 and 10, are presented in Table 1. Using published information on SPSW geometries and member sizes, strip models for those considered SPSWs were devel-

oped, and the corresponding maximum VBE shears obtained from the pushover analysis using SAP2000 (i.e., $V_{pushover}$) are also provided in Table 1. Note that 20 strips were used for the infill plates at each story in all specimens. Steel was modeled as an elasto–perfectly plastic material using the yield strength provided in each relevant reference. Plastic hinges accounting for the interaction of axial force and flexure were defined at the ends of HBEs and the VBE bases. The vertical distributions of lateral forces used in the pushover analyses were determined according to the loading conditions reported for each actual test. For comparison purposes, specimen scale, aspect ratio and tension field inclination angle of those considered SPSWs are provided in Table 1.

Comparing $V_{pushover}$ to $V_{u-design}$, Table 1 confirms that Equation 9 gives conservative VBE design shear forces (as expected since it assumes plastic hinges at both ends of the VBE). The level of conservation varies from 0.7% to 57%, and is, on average, 25% for the cases considered.

On the other hand, comparing V_n to $V_{pushover}$ reveals that the VBEs in cases 1, 3, 6, 7 and 8 should have experienced shear yielding during their tests while the VBEs in other cases would not. This prediction is consistent with experimental observations. For a better understanding, the following will focus on the observed VBE behaviors in cases 1, 3, 6, 7 and 8.

For the SPSW of case 1 [i.e., the single-story SPSW (SPSW2) tested by Lubell et al. (2000)], significant inward deformations were observed in the VBEs as shown in Figure 6. Montgomery and Medhekar (2001) ascribed this undesirable VBE behavior to: (1) the small infill panel width-to-height aspect ratio compared to other specimens for which the VBEs exhibited desirable behavior, (2) relative small tension field inclination angle calculated per the equation provided in the AISC *Seismic Provisions* and CSA S16-01, and (3) excessive VBE flexibility.

The fact that the single-story specimen had a width-to-height infill panel aspect ratio of approximately 1.0, by itself, should not be a concern contrary to the claim by Montgomery and Medhekar (2001). This is because the VBEs of the MCEER/NCREE full-scale two-story SPSW specimen, which had the same width-to-height aspect ratio of 1.0, exhibited desirable VBE performance (Qu et al., 2008), and others have also tested narrow SPSWs that exhibited equally satisfactory behavior (e.g., Lee and Tsai, 2008, used an aspect ratio of 0.66).

In addition, the tension field inclination angle of the single-story specimen calculated per the AISC *Seismic Provisions* (AISC, 2005c) and CSA S16-01 is 37.4°. That, by itself, should not be a reason for the observed undesirable VBE behavior. As presented in Table 1, the two-story SPSW (specimen SPSW S) recently tested by Lee and Tsai (2008) had an even smaller inclination angle of 36.5° and exhibited satisfactory VBE performance up to story drifts greater than 5%.

As to whether the undesirable VBE inward deformation observed in the single-story specimen can be attributed to excessive VBE flexibility, even though this specimen had a flexibility factor of 3.35 (i.e., greater than the code specified limit of 2.5), the results in Table 1 demonstrate that VBE shear yielding occurred in that specimen during the tests, resulting in the significant in-plane VBE deflection due to inelastic shear deformations. Yielding pattern of the VBE webs further confirms this point. As indicated by the flaked whitewash shown in Figure 6, the VBE web yielded uniformly at the VBE ends as opposed to the yielding pattern usually observed in flexural plastic hinges, indicating significant inelastic shear deformations. Note that the axial force in the VBEs can also affect the yielding pattern of VBE webs. However, the axial force developed in the VBEs is insignificant in this single-story case.

For the SPSW of case 3 (i.e., the four-story SPSW tested by Driver et al., 1997), deformations at the first story of the wall are shown in Figure 8. Note that this specimen had a code-compliant flexibility factor of 1.73. Incidentally, plastic strength of the wall predicted using the procedure proposed by Berman and Bruneau (2003), which has been verified by numerous other experimental results, is substantially greater than the strength obtained during the test. Sabouri-Ghomi (2005) alleged that the reduced plastic strength of

the wall could be due to overall bending effects. However, results shown in Table 1 unequivocally show that VBE shear yielding occurred in the first-story of that specimen. This may have resulted in incomplete development of the expected VBE plastic moments and infill tension field at the first story, and thus the lower plastic base shear compared to the predictions from plastic analysis. Interestingly, fractures were observed to penetrate into the VBE web at the column bases during tests, which may also be related to the significant shear force acting there.

Cases 6, 7 and 8 are three-story specimens from a series of tests on SPSWs by Park et al. (2007). For comparison purpose, case 6 is first compared against cases 4 and 5. Specimens of cases 4, 5 and 6 (i.e., SC2T, SC4T and SC6T, respectively, in Park et al., 2007) have flexibility factors of 1.24, 1.44 and 1.58, respectively, which all satisfied the code-specified limit of 2.5. These specimens had identical boundary frame members and constant infill panels along the height of each wall [with thicknesses of 2 mm, 4 mm and 6 mm in SC2T, SC4T and SC6T, respectively (0.08 in., 0.16 in. and 0.24 in.)]. These specimens had the same VBE members and thus the same shear strength per Equation 10. However, the shear demands on the first-story VBEs of SC2T, SC4T and SC6T increased directly as a function of the infill panel yield forces, which are determined from the infill panel thicknesses. As shown from the results in Table 1, the first-story VBEs of SC6T are expected to yield in shear while those of SC2T and SC4T would not. This prediction agrees with the observed yielding patterns shown in the photos presented in Park et al. (2007).

For the specimens in cases 7 and 8 [i.e., WC4T and WC6T in Park et al. (2007), respectively], the VBEs were wide flange members with noncompact flanges. WC4T and WC6T have code-compliant flexibility factors of 1.62 and
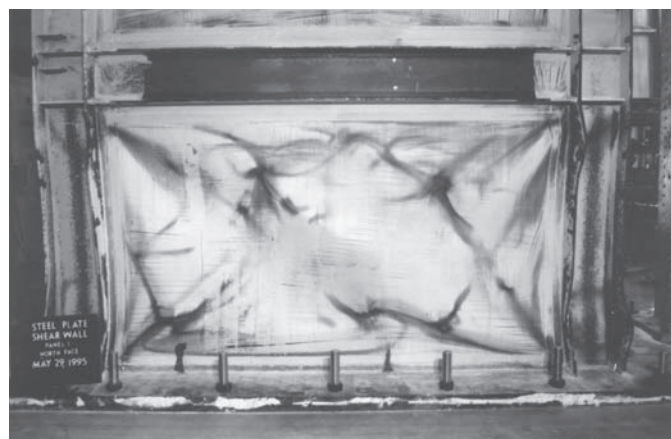

Fig. 8. First story of Driver's SPSW (photo courtesy of R.G. Driver).

1.77, respectively. However, significant pull-in deformations were observed in the VBEs of these two specimens. Local buckling due to flange noncompactness is an important factor that contributed to the VBE deflections during these tests, but the results in Table 1 indicate that shear yielding also developed in those VBEs. The observed VBE yielding pattern and deformation further confirm this point. As shown in the photos published by Park et al. (2007), yield lines gradually developed in the VBE web with the increases of story drift, indicating the development of VBE shear yielding, which finally resulted in significant inward deflections in the VBEs.

As discussed earlier, undesirable inward VBE deflections were observed in SPSW specimens with and without code-compliant flexibility factors. There is no correlation between flexibility factor and significant VBE pull-in deformations. Based on the analytical work conducted in this section, the observed undesirable VBE deflections were mainly caused by VBE shear yielding.

VBE Out-of-Plane Buckling

Besides the aforementioned excessive pull-in deformations, another undesirable behavior of VBE is out-of-plane buckling, which has been observed during the tests on a quarter-scale four-story SPSW specimen by Lubell et al. (2000). Confusion exists at whether this undesirable performance was also ascribed to the insufficient VBE stiffness; the AISC 341-05 commentary is not clear in this regard. At the time of this writing, no theoretical work has been conducted to establish the correlation between ω*t* and out-of-plane buckling strength of VBEs.

This section will investigate whether the available database of test results sustain the use of flexibility limit for VBE design to successfully prevent the out-of-plane buckling of VBE, or whether different methods are necessary for that purpose. To be able to do such comparisons, analytical models to estimate the out-of-plane buckling strength of VBEs are provided based on simple free body diagrams and the energy method taking into account representative boundary conditions of VBEs. Using the proposed analytical models, the out-of-plane behaviors of VBEs in a few representative tested SPSWs that have various values of flexibility factor are reviewed.

ANALYTICAL MODELS FOR OUT-OF-PLANE BUCKLING STRENGTH OF VBES

Free Body Diagrams of VBEs

Figure 9 shows free body diagrams of the left and right VBEs in a typical single-bay multi-story SPSW when the expected plastic mechanism of the wall develops under the rightward lateral forces. In the free body diagrams, ω_{xci} and ω_{yci} represent horizontal and vertical components of the

infill plate yield force along the VBE; P_{bli} and P_{bri} represent the axial forces at the left and right ends of HBE; V_{li} and V_{ri} represent the shear forces at the left and right VBE faces; M_{li} and M_{ri} represent the moments at the left and right VBE faces; R_{xl}, R_{xr}, R_{yl}, R_{yr}, M_{cl} and M_{cr} represent the reaction forces at VBE bases; and F_i represents the applied lateral forces to develop the expected plastic mechanism. Note that the free body diagrams of Figure 9 are only for illustration purpose and the forces shown in the figure may have a different direction depending on the equilibrium of the free body.

Free body diagram of the VBE on the right-hand side is chosen for derivation of the out-of-plane buckling strength of VBE, since the compression effect in that VBE due to the HBE end shears is additive to that from the vertical component of the infill panel yield forces along that VBE. The compression at the top end of the considered VBE, P_{topi}, can be obtained as:

$$P_{topi} = \sum_{j=i}^{n_s} V_{rj} + \sum_{j=i+1}^{n_s} \omega_{ycj} \cdot h_{sj} \qquad (11)$$

where n_s is the number of stories and all other terms have been defined previously.

To ensure desirable VBE behavior, it is recommended, although slightly conservative, to neglect the reduction effects on HBE plastic moment accounting for the presence of axial force, shear force, and vertical stresses in HBE when calculating V_{rj} for determination of the VBE axial forces. In addition, it is assumed that plastic hinges form at the column face when reduced beam section (RBS) connections (ANSI/AISC 358-05) are not used in HBEs. Accordingly, the right-end shears of HBEs are obtained as:
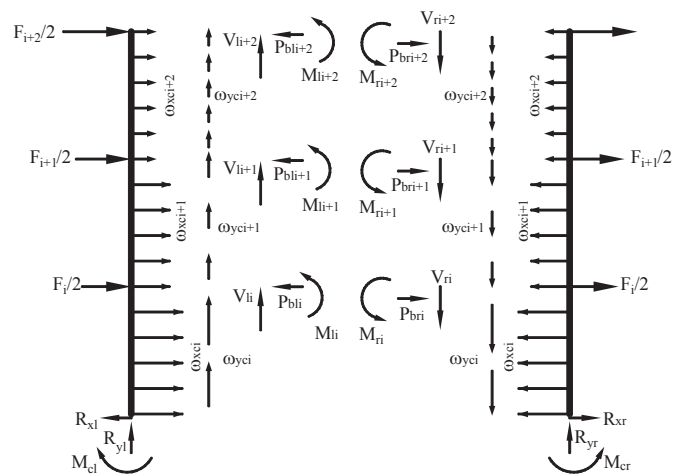

Fig. 9. VBE free body diagrams.

$$V_{ri} = \frac{\left(\omega_{ybi} - \omega_{ybi+1}\right)L}{2} + \frac{\left(\omega_{xbi} + \omega_{xbi+1}\right)d}{2} + \frac{2R_y f_y Z_{ef}}{L_h} \quad (12)$$

where

ω_{xbi}	=	horizontal component of the infill plate yield forces along HBE (Berman and Bruneau, 2008)
ω_{ybi}	=	vertical component of the infill plate yield forces along HBE (Berman and Bruneau, 2008)
d	=	HBE depth
L	=	distance between the column faces
L_h	=	distance between plastic hinge locations
Z_{ef}	=	effective plastic section modulus of HBEs

Note that Z_{ef} is equal to the plastic section modulus of a HBE when RBS connections are not used. For a HBE without RBS connections Z_{ef} should be determined according to the equations proposed by Qu and Bruneau (2008) to account for the variation of plastic hinge location in the RBS zone.

Energy Method and Boundary Conditions

Although modeling the considered VBE in some FE software packages such as ABAQUS is always possible, at the cost of computational efforts, it is relatively expedient and efficient here to illustrate important trends by using the energy method to approximately calculate the critical buckling strength of VBEs (i.e., the Euler buckling strength assuming elastic behavior and no initial imperfection in the member). It is recognized that the actual buckling strength of the member considering the previously mentioned effects would be lower and that the buckling strength calculated by this approach is optimistic. It should, therefore, not be used for design.

A rigorous derivation of the buckling strength of VBEs which takes into account inelastic behaviors and all possible boundary conditions of VBEs is complex and would be a major undertaking beyond the scope of this paper. For example, one major impediment is how to consider the boundary conditions of VBEs due to the infill panels. Note that the infill panels provide tension-only supports along the VBEs while exerting longitudinal and transverse loads along VBEs. While awaiting further research results on the buckling strength of VBEs, it is recommended to continue designing VBEs as beam-columns according to Chapter H of ANSI/AISC 360-05 for conservative combinations of maximum acting moment, shear, and axial forces, assuming conservative unsupported lengths.

However, the work presented here, even though based on elastic analysis and idealized properties, is important and included for the following reasons. First, while it is always possible to achieve conservative VBE designs (as described earlier), the objective here is to review behavior of VBEs in prior tests and attempt to see if the observed out-of-plane buckling failure can be predicted. In that perspective,

a conservative design model is of limited value. Second, if the simplified idealized elastic model considered here predicts buckling, then it is reasonably certain that the actual VBE would buckle (given that inelastic behavior and initial imperfections would reduce buckling strength). As such, a prediction of VBE buckling using the simplified approach proposed here can be helpful to confirm the case where buckling was observed in the experimental studies reviewed in this paper (recognizing that a prediction of non-buckling is not a guarantee of satisfactory performance). Finally, the results obtained using the idealized model, in spite of its own shortcomings, help bring attention to some of the important issues that must be considered in future more complex models such as boundary conditions and loads applied by the infill plate along the length of the VBEs. As such, the analytical models assuming elastic buckling behaviors of VBEs provide some of the building blocks and important perspectives necessary to derive the more advanced analytical models for calculating VBE buckling strength accounting for inelastic behavior and more complicated boundary conditions in future investigations.

The energy method considered in this paper is used in buckling problems to determine approximate values of the critical buckling strength when an exact solution of the differential equation of the deflection curve is either unknown or too complicated. In such cases, solution proceeds by assuming a reasonable shape for the deflection curve. While it is not essential for an approximate solution that the assumed curve perfectly match the deflected shape, it should satisfy the boundary conditions at the ends of the member. Using a reasonable assumed shape for the deflection curve, the energy method can give an approximate out-of-plane buckling strength of VBE, within the previously enunciated constraints (Timoshenko and Gere, 1961).

Figure 10 illustrates orientations of the VBE weak and strong axes in a typical SPSW, for which the smaller and greater moments of inertia of the VBE cross-section can be obtained. Note that VBE out-of-plane buckling develops in the plane perpendicular to the weak axis. The ends of VBEs
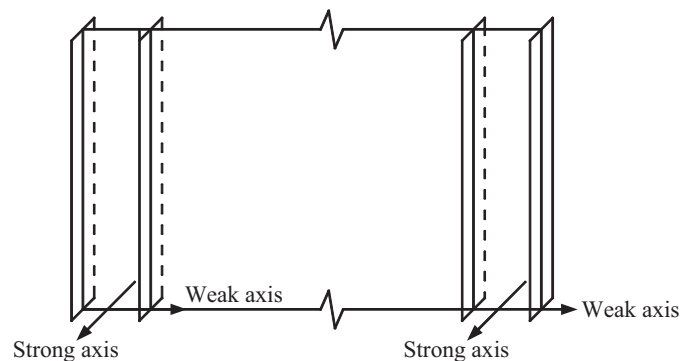

Fig. 10. Strong and weak axes of VBEs.

Table 2. Key Parameters and Criteria for Considered Boundary Conditions[a]				
Factors	Case A	Case B	Case C	Case D
Shape function	$y = \delta_i \sin\left(\dfrac{\pi x}{h_{si}}\right)$	$y = \delta_i \left[1 - \cos\left(\dfrac{2\pi x}{h_{si}}\right)\right]$	$y = \delta_i \left[2x^4 + 3x^2 h_{si}^2 - 5x^3 h_{si}\right]$	$y = \delta_i \left[2x^4 - 3x^3 h_{si} + x h_{si}^3\right]$
External work	$\dfrac{\pi^4 \delta_i^2 EI_{yi}}{4h_{si}^3}\left(m + \dfrac{n}{2}\right)$	$\dfrac{\pi^4 \delta_i^2 EI_{yi}}{h_{si}^3}\left(m + \dfrac{n}{2}\right)$	$\dfrac{6\pi^2 \delta_i^2 EI_{yi} h_{si}^5}{35}\left(m + \dfrac{3n}{8}\right)$	$\dfrac{6\pi^2 \delta_i^2 EI_{yi} h_{si}^5}{35}\left(m + \dfrac{5n}{8}\right)$
Strain energy	$\dfrac{\pi^4 \delta_i^2 EI_{yi}}{4h_{si}^3}$	$\dfrac{4\pi^4 \delta_i^2 EI_{yi}}{h_{si}^3}$	$\dfrac{18\delta_i^2 EI_{yi} h_{si}^5}{5}$	$\dfrac{18\delta_i^2 EI_{yi} h_{si}^5}{5}$
Criterion	$m + \dfrac{n}{2} = 1$	$\dfrac{m}{4} + \dfrac{n}{8} = 1$	$\dfrac{\pi^2}{21}m + \dfrac{\pi^2}{56}n = 1$	$\dfrac{\pi^2}{21}m + \dfrac{5\pi^2}{168}n = 1$

[a] An arbitrarily selected nonzero defection factor, δ_i, is used in the shape function. Note that the magnitude of δ_i has no impact on the buckling strength of VBE.

are laterally supported by the floor system, and the first-story VBE is either fixed or pinned to ground. Under those conditions, the out-of-plane translations at the VBE ends are restrained. However, the out-of-plane rotational restraints due to the beams framing into the VBEs can vary from fully free to fully fixed and would have to be assessed on a case by case basis. The VBE end conditions considered in this paper are illustrated in Figure 11(a) and correspond to ideal cases.

Criteria for the Considered Boundary Conditions

The out-of-plane buckling strength of VBE under each case of boundary conditions can be obtained following the classic procedure of energy method and the detailed derivations are presented in Qu and Bruneau (2008). In such derivation, the internal strain energy is obtained by accounting for the curvature determined from the assumed VBE deflection curve, and the external work is obtained by combining the contribution due to the concentrated force applied at the top of the VBE and that due to the infill panel yield forces along the VBE. Setting the internal strain energy equal to the external work, one can obtain the criterion to calculate the out-of-plane buckling strength of VBE. Deflection curve, internal strain energy, external work, and criterion of each considered case are presented in Table 2.

For each case of boundary conditions, the corresponding criterion that defines the buckling limit state can be expressed as a combination of m and n equal to unity, where m and n are the generalized external forces and can be respectively obtained by normalizing the concentrated force applied at the top of the VBE (i.e., P_{topi}) and the resultant infill panel yield force along the VBE (i.e., $\omega_{yci} h_{si}$), by the Euler buckling load of a simply supported VBE without any intermediate loads along its height. Namely, m and n can be determined as:

$$m = \frac{P_{topi}}{\left[\dfrac{\pi^2 EI_{yi}}{h_{si}^2}\right]} \text{ and } n = \frac{\omega_{yci} h_{si}}{\left[\dfrac{\pi^2 EI_{yi}}{h_{si}^2}\right]} \tag{13}$$

where I_{yi} is the moment of inertia of the VBE taken from the weak axis.

Graphical versions of the criteria presented in Table 2 are shown in Figure 11(b). For a given load combination (i.e., a pair of m and n) and boundary conditions, if the left-hand side of the corresponding criterion presented in Table 2 is greater than 1, the VBE is expected to encounter out-of-plane buckling. Those combinations for which buckling failure occurs are represented by the shaded area in Figure 11(b). Incidentally, using an alternative approach based on the differential equations of beam-column theory, Timoshenko and Gere (1961) provided the critical buckling strength of the column under Case A boundary conditions for a few selected individual scenarios. Their results are also presented in Figure 11(b). As expected, a good agreement is observed. As shown, for each case, the value of m decreases when the value of n increases, which physically means that lower concentrated force needs to be applied at the top of the column to avoid column buckling when higher infill panel yield forces are applied. Note that parts of Figure 11 are presented with different vertical axes to purposely improve legibility. It also should be mentioned that the negative range of m in Criterion A is reasonable and it is consistent with the fact that, when large infill panel yield forces are applied along the column (which corresponds to large values of n), the axial force required at the top end of the member to avoid out-of-plane buckling failure should be upward (i.e., it should be a tensile force which corresponds to the negative value of m).

REVIEW OF OUT-OF-PLANE BUCKLING
OF VBES IN PAST TESTS

To better understand the VBE out-of-plane buckling behavior, performance of the VBEs in previously tested SPSWs are revisited in perspective of the criteria derived in the previous section to see whether the proposed alternative approach can shed additional light on the behavior of VBEs.
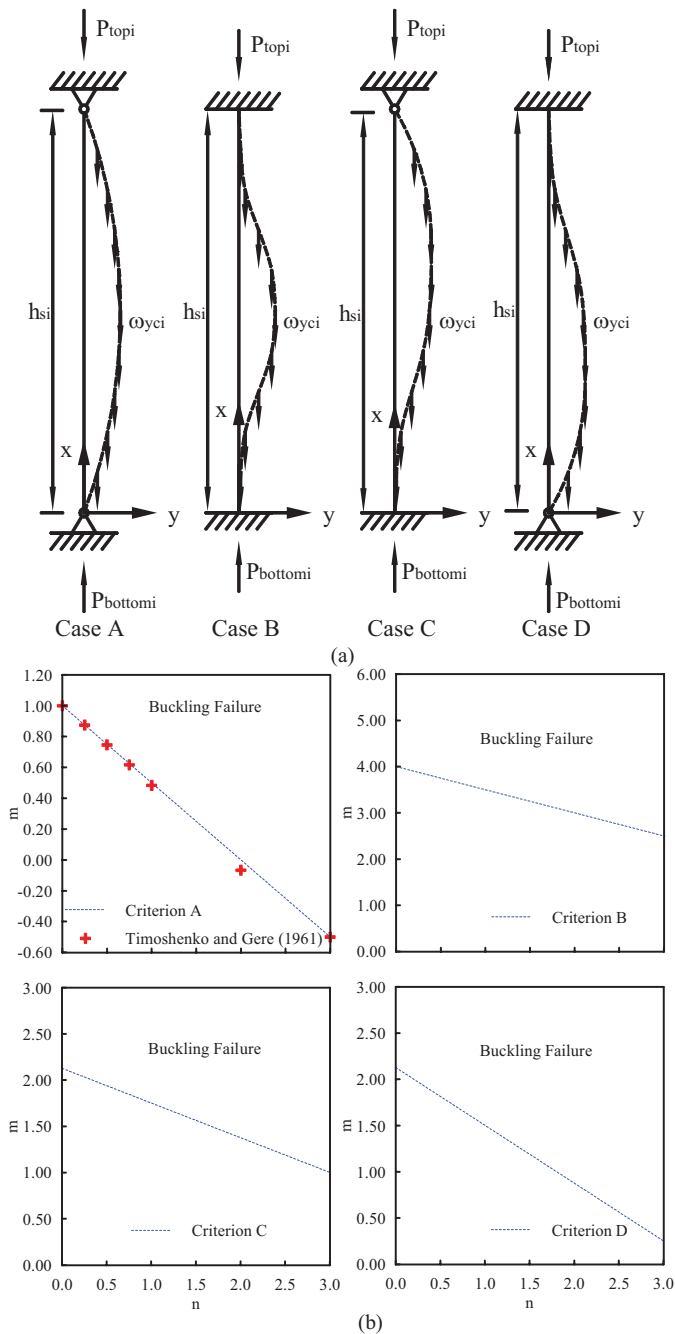

Fig. 11. Out-of-plane buckling of VBE: (a) considered boundary conditions; (b) interaction of critical loads.

The considered SPSW specimens are assessed using the criteria developed for the four boundary conditions considered since the out-of-plane restraints at the ends of the VBEs of some specimens are not provided in the available references. As shown by the results presented in Table 3, no matter what boundary conditions were applied, VBE out-of-plane buckling would not be predicted to occur in any of the SPSWs except for the Lubell et al. (2000) quarter-scale four-story SPSW. This prediction is consistent with the observations on those SPSWs obtained during tests, validating to some degree the proposed analytical models for calculating VBE out-of-plane buckling strength. Note that for this Lubell et al. specimen insignificant amounts of hysteretic energy were dissipated before instability of VBE precipitated the system failure.

A closer look at the Lubell et al. specimen and the buckled shape of its VBE reveals that Case C boundary conditions were present (i.e., bottom end of the VBE was fixed to the ground while the top end was pinned in the out-of-plane direction). To better understand this, the VBE deflection traced from the specimen is superposed to those corresponding to cases B and C boundary conditions in Figure 12. Comparing the deflected shapes confirms that the VBE end conditions correspond to those of Case C. Accordingly, applying Criterion C provides a value of 1.066 greater than 1.0 as shown in Table 3, indicating the expected occurrence of VBE out-of-plane buckling. This suggests that out-of-plane buckling of the VBEs in the Lubell et al. specimen can be rationally predicted using the out-of-plane buckling equations derived here rather than excessive VBE flexibility.

Two other interesting cases in Table 3 are the two specimens (i.e., SPSW N and SPSW S) tested by Lee and Tsai (2008). SPSW N and SPSW S, respectively, had flexibility factors of 2.53 and 3.01 (i.e., above the code-specified upper
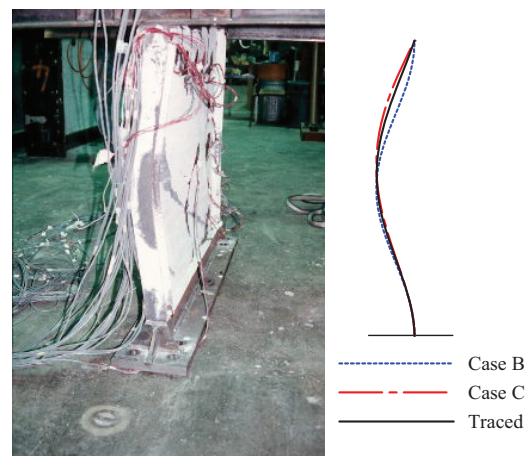

Fig. 12. Out-of-plane buckling of bottom VBE
(photo courtesy of C.E. Ventura).

Table 3. Evaluation of VBE Out-of-Plane Buckling[a]								
Case	Researcher	Specimen Identification	Number of Stories	ω_t	Criterion A	Criterion B	Criterion C	Criterion D
(i) single-story specimens								
1	Lubell et al. (2000)	SPSW2	1	3.35	0.609	0.152	0.260	0.313
2	Berman and Bruneau (2005)	F2	1	1.01	0.006	0.001	0.002	0.003
(ii) multi-story specimens								
3	Driver et al. (1998)	[b]	4	1.73	0.159	0.040	0.073	0.077
4	Lubell et al. (2000)	SPSW4	4	3.35	2.325	0.581	1.066	1.119
5	Park et al. (2007)	SC2T	3	1.24	0.051	0.013	0.024	0.024
6		SC4T	3	1.44	0.087	0.022	0.040	0.042
7		SC6T	3	1.58	0.115	0.029	0.053	0.055
8		WC4T	3	1.62	0.142	0.036	0.065	0.068
9		WC6T	3	1.77	0.188	0.047	0.086	0.090
10	Qu et al (2008)	[b]	2	1.95	0.238	0.060	0.107	0.116
11	Lee and Tsai (2007)	SPSW N	2	2.53	0.111	0.028	0.050	0.054
12		SPSW S	2	3.01	0.199	0.050	0.090	0.097

[a] For multi-story specimens, VBEs at the first story are evaluated.
[b] Not applicable.

limit of 2.5). Yet, based on the proposed analytical models, the VBEs in these two specimens are not expected to undergo out-of-plane buckling. This prediction is consistent with the experimental observations. The VBEs of these two specimens exhibited ductile behavior up to story drifts greater than 5%. The assessment on SPSW N and SPSW S further confirms that there is no correlation between the flexibility factor, ω_t, and VBE out-of-plane buckling strength.

CONCLUSIONS

In this paper, analytical work was conducted to assess the adequacy of the existing limit on the flexibility factor, ω_t, specified for VBE design by the AISC *Seismic Provisions* and CSA S16-01. Review of the derivations of this flexibility factor from plate girder theory and how that factor was incorporated into current design codes was followed by the development of analytical models for preventing VBE shear yielding and for estimating out-of-plane buckling strength of VBEs in SPSWs.

It is shown that the existing limit on ω_t is uncorrelated to satisfactory in-plane and out-of-plane VBE performance. Alternatively, the proposed analytical model for in-plane VBE shear demands, from which predicted performance correlates well with past experimental results, can be used to ensure desirable VBE behavior. Future analytical and experimental research should investigate whether in-plane buckling

equations similar to those used for out-of-plane buckling are necessary for use in the interaction equations to calculate the beam-column strength of VBEs, and whether other concerns may justify retaining the use of ω_t factor to achieve satisfactory seismic performance of VBEs in SPSWs.

REFERENCES

AISC (2005a), ANSI/AISC 358-05, *Prequalified Connections for Special and Intermediate Steel Moment Frames for Seismic Applications*, American Institute of Steel Construction, Chicago, IL.

AISC (2005b), ANSI/AISC 360-05, *Specification for Structural Steel Buildings*, American Institute of Steel Construction, Chicago, IL.

AISC (2005c), ANSI/AISC 341-05, *Seismic Provisions for Structural Steel Buildings,* American Institute of Steel Construction, Chicago, IL.

Berman, J.W. and Bruneau, M. (2003), "Plastic Analysis and Design of Steel Plate Shear Walls," ASCE, *Journal of Structural Engineering*, Vol. 129, No. 11.

Berman, J.W. and Bruneau, M. (2004), "Steel Plate Shear Walls are Not Plate Girders," AISC, *Engineering Journal* Vol. 41, No. 3.

Berman, J.W. and Bruneau, M. (2005), "Experimental Investigation of Light-Gauge Steel Plate Shear Walls," ASCE, *Journal of Structural Engineering*, Vol. 131, No. 2.

Berman, J.W. and Bruneau, M. (2008), "Capacity Design of Vertical Boundary Elements in Steel Plate Shear Walls," AISC, *Engineering Journal,* Vol. 45, No. 1.

CSA (1994), "Limit States Design of Steel Structures," CAN/CSA S16-94, Toronto, ON, Canada.

CSA (2001), "Limit States Design of Steel Structures," CAN/CSA S16-01, Toronto, ON, Canada.

Driver, R.G., Kulak, G.L., Kennedy, D.J.L. and Elwi, A.E. (1998), "Cyclic Test of a Four-Story Steel Plate Shear Wall," ASCE, *Journal of Structural Engineering*, Vol. 124, No. 2.

FEMA (2003), "NEHRP Recommended Provisions for Seismic Regulations for New Buildings and Other Structures," FEMA 450, prepared by the Building Seismic Safety Council for FEMA, Washington, D.C.

Lee, C.S. and Tsai, K.C. (2008), "Experimental Response of Four 2-Story Narrow Steel Plate Shear Walls," *Proceedings of the 2008 Structures Congress*, Vancouver, BC, Canada.

Lubell, A.S., Prion, H.G.L., Ventura, C.E. and Rezai, M. (2000), "Unstiffened Steel Plate Shear Wall Performance under Cyclic Loading," ASCE, *Journal of Structural Engineering*, Vol. 126 No. 4.

Kuhn, P., Peterson, J.P. and Levin, L.R. (1952), "A Summary of Diagonal Tension. Part I: Methods and Analysis," Technical Note 2661, National Advisory Committee for Aeronautics, Washington, D.C.

Montgomery, C.J. and Medhekar, M. (2001), "Discussion on Unstiffened Steel Plate Shear Wall Performance under Cyclic Loading," ASCE, *Journal of Structural Engineering*, Vol. 127, No. 8.

Park, H.G., Kwack, J.H., Jeon, S.W., Kim, W.K. and Choi, I.R. (2007), "Framed Steel Plate Wall Behavior under Cyclic Lateral Loading," ASCE, *Journal of Structural Engineering*, Vol. 133, No. 3.

Qu, B., Bruneau. M., Lin, C.H. and Tsai, K.C. (2008), "Testing of Full Scale Two-story Steel Plate Shear Walls with RBS Connections and Composite Floor," ASCE, *Journal of Structural Engineering*, Vol. 134, No. 3.

Qu, B. and Bruneau. M. (2008), "Seismic Behavior and Design of Boundary Frame Members of Steel Plate Shear Walls," Technical Report MCEER-08-0012, Multidisciplinary Center for Earthquake Engineering Research, Buffalo, NY.

Sabelli, R. and Bruneau, M. (2007), *AISC Design Guide 20, Steel Plate Shear Walls,* American Institute of Steel Construction, Chicago, IL.

Sabouri-Ghomi, S. (2005), "Discussion of Plastic Analysis and Design of Steel Plate Shear Walls," ASCE, *Journal of Structural Engineering*, Vol. 131, No. 4.

Timoshenko, S.P. and Gere, J.M. (1961), *Theory of Elastic Stability*, 2nd edition, McGraw-Hill Book Company, Inc., New York, NY.

Vian, D. and Bruneau M. (2005), "Steel Plate Shear Walls for Seismic Design and Retrofit of Building Structure," Technical Report MCEER-05-0010, Multidisciplinary Center for Earthquake Engineering Research, Buffalo, NY.

Wagner, H. (1931), "Flat Sheet Metal Girders with Very Thin Webs, Part III: Sheet Metal Girders with Spars Resistant to Bending—The Stress in Uprights—Diagonal Tension Fields," Technical Memorandum No. 606, National Advisory Committee for Aeronautics, Washington, D.C.

Current Steel Structures Research

REIDAR BJORHOVDE

After more than five years of assembling and evaluating structural steel research projects at universities and other institutions around the world, it has become very clear to me that significant efforts are taking place in a number of countries. Although American steel research for buildings and bridges was preeminent for many years, and especially during the period from 1930 to 1980, it is amply evident that the developments in many countries have produced wide-ranging results with major implications for engineering and the construction industry. Most importantly, the worldwide community of researchers and engineers exchange ideas and findings to ensure that advances will continue to take place. Differences occur in interpretations and developments in the form of design criteria and construction practices, but by and large, the end results are effectively the same.

As a result, a new feature is being introduced for these steel structures research papers. In addition to the regular project descriptions from individual institutions, each paper will highlight the work at two or three major steel research universities—the "steel schools" of the world. The descriptions will not discuss all of the current projects at the school. Rather, a selection of studies will provide a representative picture and demonstrate the school's importance to the efforts of industry and the profession.

This issue of *Engineering Journal* provides the first in this new series, featuring the work at two North American universities. It reflects their ongoing, central roles in the research activities of the United States and Canada and their long-time impact on the design standards of the two countries. Both schools are well known: Lehigh University in Bethlehem, Pennsylvania, and the University of Alberta in Edmonton, Alberta. Researchers at the two universities have been very active for many years, as evidenced by their participation and leading roles in the standards development committees and by large numbers of outstanding technical papers, reports and conference presentations.

References are provided throughout the paper, whenever such are available in the public domain. However, much of the work is still in progress, and in some cases reports or publications have not yet been prepared for public dissemination.

Reidar Bjorhovde, Research Editor for *Engineering Journal,* 5880 E. Territory Ave., Suite 202, Tucson, AZ 85750-1803. E-mail: rbj@bjorhovde.com

LEHIGH UNIVERSITY

Development of Improved Welded Moment Connections for Earthquake-Resistant Design: This study was conducted with the sponsorship of the SAC Joint Venture and the Pennsylvania Infrastructure Technology Alliance. Steel shapes for the test specimens were donated by the Technical Committee on Structural Shapes. Professor James M. Ricles has been the director of the project.

The project was undertaken as a major assessment of the effects on the cyclic (seismic) ductility of welded unreinforced moment connections of the weld metal, the geometry of the weld access hole, the form of the beam web attachment to the column, the continuity plates, and the panel zone strength. Using finite element evaluations as well as full-scale physical tests, the results of the former were used to develop 11 connections for the testing program (Ricles et al., 2003). As illustrations of some of the findings, Figure 1 shows the setup for the connection tests and Figure 2 shows the effective plastic strain contours in the vicinity of the weld access hole.

Commenting on some of the key findings, the researchers note that:

1. Several studies have shown that the geometry of the weld access hole is critical to the performance of the connections. The difference between the original configuration and the modified access hole is emphasized by a short, flat portion on the beam flange. Figure 2 shows that the modified shape allows for a larger portion of the flange to develop plastic strains, hence an increased ductility for the connection as a whole.
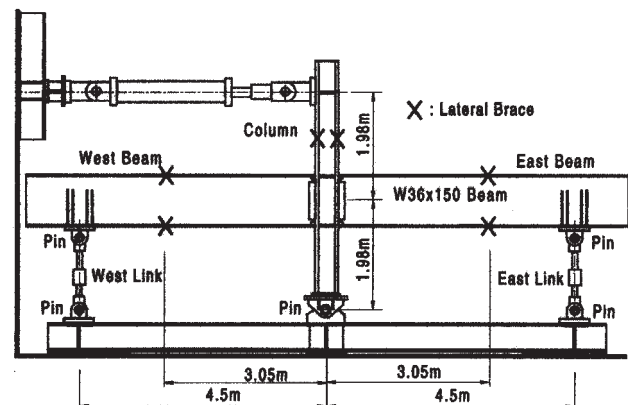

Fig. 1. Test setup for connections
(Courtesy of Professor James M. Ricles).

2. A panel zone designed on the basis of the column web yield capacity gives a connection that performs better than specimens that also incorporate the contribution of the column flanges.

3. Shear studs should not be placed in the plastic hinge region of the beam, since this reduces the fracture toughness of the beam flange material.

4. Continuity plates are not always needed. The connections that were tested without such plates and without shear studs in the plastic hinge region of the beam performed very well, developing plastic story drifts larger than 0.04 radian.

Seismic Behavior of Reduced Beam Section Moment Connections to Deep Columns: This study was conducted with the sponsorship of AISC and the Pennsylvania Infrastructure Technology Alliance. Materials for the test specimens were donated by Arcelor International America, Nucor Vulcraft Group and Lincoln Electric Company. Professor James M. Ricles has been the director of the project.

A number of other projects have addressed the issues of reduced beam section (RBS) connections and the performance of frames with such connections. This project focused on frames using deep beam shapes as columns, which is not an uncommon feature of certain structures in seismic areas. Finite element analyses were used to perform parametric studies with three-dimensional RBS models in special perimeter moment-resisting frames subjected to inelastic monotonic and cyclic loading (Zhang and Ricles, 2006a; 2006b). The parameters were (1) the beam-to-column connection type, (2) the column shape, (3) the composite floor slab, (4) the strength of the panel zone, and (5) the beam web

slenderness. Six full-scale frame subassemblages were tested; the general appearance of the test setup is similar to what is illustrated in Figure 1.

Among the unique performance characteristics of these types of frames is the fact that under certain conditions and for some of the parameters, the column will exhibit significant twisting. Figure 3 illustrates this phenomenon. Specifically, the twisting occurs as a result of out-of-plane movement of the RBS compression flange. But it was also demonstrated that the composite slab has a very significant influence on the response of the subassemblage, to the effect that it restrains the top flange of the beam and therefore reduces the lateral displacement of the RBS connection and consequently the magnitude of the column twist. In addition, the slenderness of the beam web is an important contributor to the lateral displacement of the beam flange in the connection. Figure 4 shows the finite element results for the column twist as a function of the beam web slenderness and the influence of the slab, using a range of beam shape sizes. Thus, the amount of twist is small and essentially constant for all magnitudes of beam slenderness when the slab effect is taken into account. In the absence of the slab, the twist is quintupled as the beam slenderness goes from that of a W36×135 to that of a W36×256.

Horizontally Curved Tubular Flange Girders: This project has been sponsored by the Federal Highway Administration and the Pennsylvania Infrastructure Technology Alliance, with High Steel Structures, Inc., Lancaster, Pennsylvania, as a project partner. The project director has been Professor Richard Sause.

Recognizing the fact that complex highway geometries offer significant challenges for the bridges that have to be built, curved girder bridges have become very common over
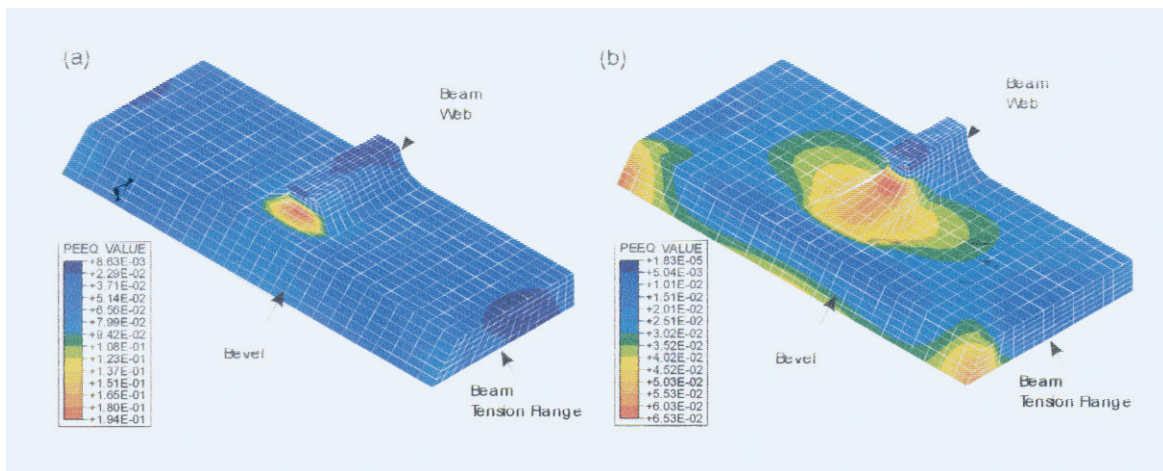

Fig. 2. Plastic strain contours for (a) traditional weld access hole and (b) modified weld access hole (Courtesy of Professor James M. Ricles).

the past several years. One of the major issues for curved girders is the lateral stability during construction as well as during service. Traditional rolled beams and plate girders have flanges that offer low torsional stiffness. The concept of built-up girders with tubular flanges was developed in recognition of the stiffness offered by the tubular shape, in addition to the fact that such flanges could add strength as well as bending stiffness for the girders. Figure 5 illustrates the concept.

Recent analytical studies have demonstrated the potential of such girders (Dong and Sause, 2009, 2010). A testing program for curved tubular flange girders is now under way, focusing first on one-half scale individual girders and now also on a two-thirds scale two-girder bridge, as shown in Figure 6. The two-girder bridge test aims at determining the behavior and strength under simulated construction and service conditions; the response characteristics of individual girder will be assessed in comparison to regular curved plate
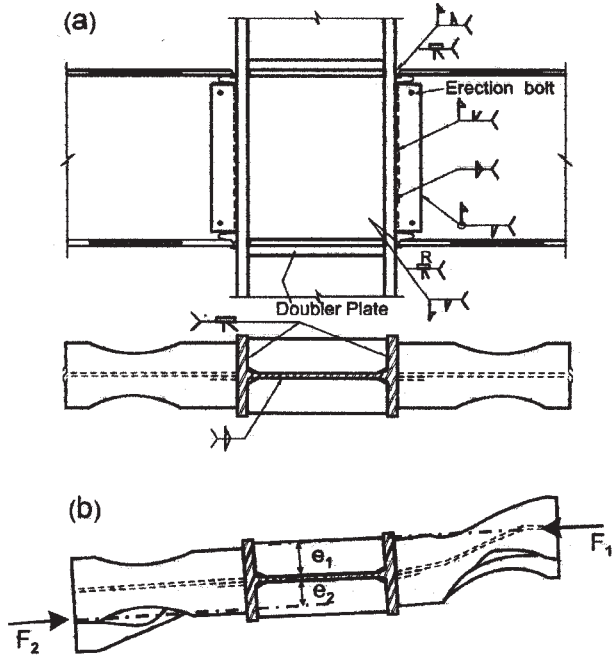

Fig. 3. (a) Details of the RBS connection; (b) column twisting that occurs when a plastic hinge forms in the RBS (Courtesy of Professor James M. Ricles).
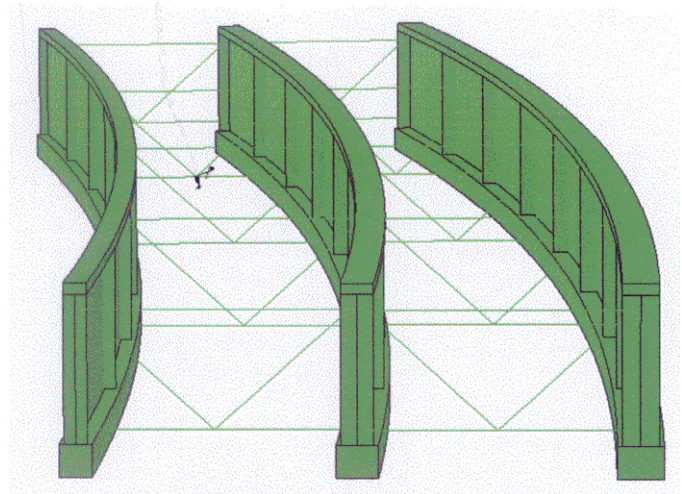

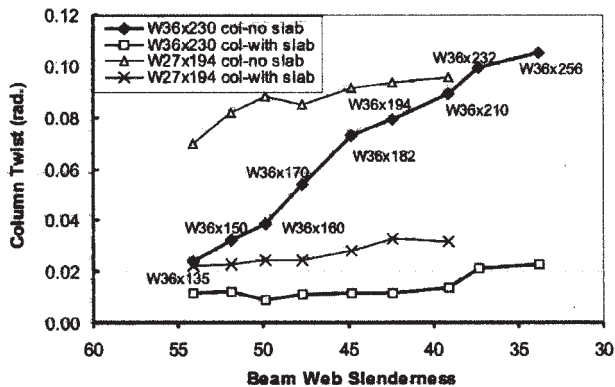Fig. 5. Curved hollow flange girder system (Courtesy of Professor Richard Sause).

Fig. 4. Influence of slab, beam size and web slenderness on the magnitude of the column twist. Column sizes are shown in top left corner. (Courtesy of Professor James M. Ricles).

Fig. 6. Test specimen for a two-thirds scale curved tubular flange bridge structure (Courtesy of Professor Richard Sause).

girders. The results to date confirm the predicted stiffness and strength, with substantially smaller stresses, deflections and cross-sectional rotations than those of curved plate girders. Further, a multi-girder tubular flange bridge requires fewer cross frames and smaller frame members.

Damage-Free Seismic-Resistant Self-Centering Concentric Braced Frames: This project has been sponsored by the NEES Program of the National Science Foundation and by AISC. Professors James M. Ricles and Richard Sause have been the project directors.

Concentrically braced frames (CBF) offer relatively simple and economical structural systems. However, in view of the limited drift capacity of such types of frames and their tendency to suffer seismic damage, the self-centering CBF system was developed to provide structures that would undergo limited damage. At the same time the system offers the opportunity for improved repair and restoration after an earthquake (Sause et al., 2006; Roke et al., 2009).

The unique behavior of these self-centering frames (SC-CBF) is represented by the rocking of the frame at the base. The structure is stabilized by vertical high-strength post-tensioning (PT) bars that extend over the full height of the frame. Under low-level earthquakes the frame behaves as traditional CBF; under high lateral loads the PT bars provide a stabilizing, restoring system that limits the frame displacements and the damage that otherwise would occur.
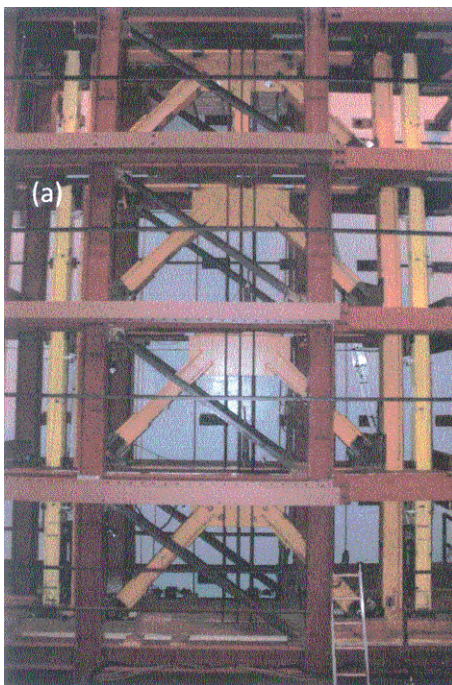
Extensive nonlinear dynamic analyses have been performed to assess the behavior of the frame, and at this time a large-scale frame test is under way. Figure 7 shows the multistory frame (yellow elements within the test setup), and Figure 8 shows the uplift that takes place at the base. The physical response therefore mirrors the analytical predictions.

The researchers have developed an improved design method that also incorporates nonlinear dynamic procedures. It takes into account the internal forces associated with yielding of the post-tensioning bars as well as the forces associated with higher modes of dynamic response.

UNIVERSITY OF ALBERTA

Steel Plate Shear Walls with Partially Encased Composite Columns: This project has been sponsored by the Natural Sciences and Engineering Research Council (NSERC) of Canada and the Canam Group. Professor Robert G. Driver has been the project director.

Steel plate shear walls are now being used in a number of structures in seismic areas. One of the problems of these otherwise very efficient and ductile lateral load-resisting systems has been the stability and strength of the columns (boundary elements) of the walls. Studies have demonstrated that partially encased composite columns, with concrete placed between relatively thin flanges and web of built-up H-shapes (Chicoine et al., 2002; Prickett and Driver, 2006), may offer a suitable solution for the columns of the shear walls. It is noted that the thin flanges are connected by closely spaced steel bars to prevent local buckling. These bars can be seen in Figure 9.

A series of three large-scale shear wall tests are in the process of being conducted. The intent is to establish the behavior, ductility and failure mode of the shear wall and the columns. The second of the test walls utilized a modular system, omitting the moment connections to have a more

Fig. 7. SC-CBF test setup. Yellow elements in the picture represent the braced frame (Courtesy of Professors James M. Ricles and Richard Sause).

Fig. 8. Rocking displacement at the base of a column of the SC-CBF (Courtesy of Professors James M. Ricles and Richard Sause).

economical solution. Figure 9 shows this test specimen before the concrete has been placed between the flanges of the columns.

The first test used the regular solution with beam-to-column moment connections; it demonstrated very ductile response characteristics but also identified certain connection detailing issues. Figure 10 shows this test in progress, with the usual buckling shape of the shear wall.

Design recommendations are currently being developed. In particular, special attention is paid to the detailing needs of the walls.

Repair of Fatigue Cracks in Steel Structures: This project has been sponsored by the Natural Sciences and Engineering Research Council (NSERC) of Canada and Syncrude Canada Ltd. Professor Gilbert Y. Grondin has been the project director.

Fatigue cracks occur regularly in structures such as bridges, industrial structures, offshore structures and mining equipment. Downtime due to repair efforts can be long and costly, and the repairs are not always effective. Under the best of circumstances, the designer should be in a position to specify what repair method and procedures should be followed, and even whether repairs should be attempted in the first place. The latter is recognition of the fact that such repairs often make the situation worse. Nevertheless, practical repairs need to be done, with a realistic expectation that they will be successful. Very often the designer will evaluate what was done in the past for similar cracking details, but such an approach is neither effective nor fully reliable.

Various repair techniques are being evaluated by the researchers at the University of Alberta, including assessments by fracture mechanics, reliability methods and similar advanced approaches. The variables include material properties, detail geometries, initial flaw conditions and loading conditions. Possibly two of the most common repair methods involve hole drilling and hole drilling with hole expansion. For the case of hole drilling alone, a hole is placed at the crack tip, on the assumption that this will arrest the crack propagation. Such has been successfully used in many cases. On the other hand, hole drilling and a small amount of hole expansion has been found to be very effective. Thus, expanding the hole at the crack tip by a mere 3% increases the fatigue life by a factor of 4 to 5. This is illustrated in Figure 11, where fatigue life versus stress range has been determined for holes with and without expansion. The correlation with reliability analyses of various forms is very good (Josi, 2010).

SWISS FEDERAL INSTITUTE OF LAUSANNE

Crack Propagation in Tubular Joints under Compressive Loading: This project has been sponsored by the Swiss National Science Foundation (SNF) with test materials provided by Vallourec & Mannesmann. Professor Alain Nussbaumer has been the project director.
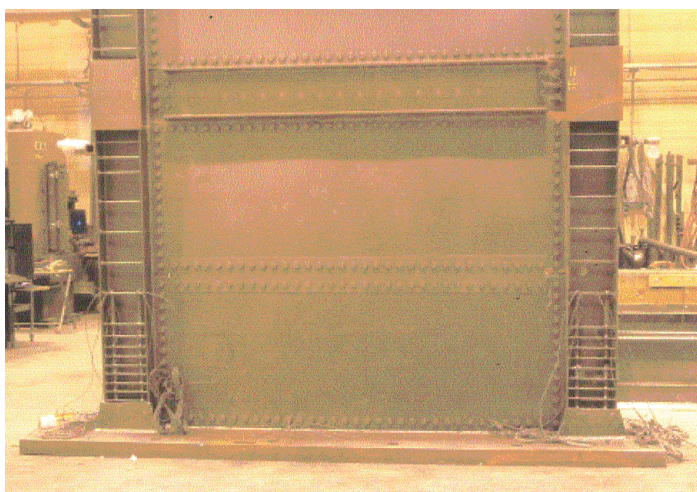
Fig. 9. Modular shear wall specimen before concrete placement in between the flanges of the columns (Courtesy of Professor Robert G. Driver).
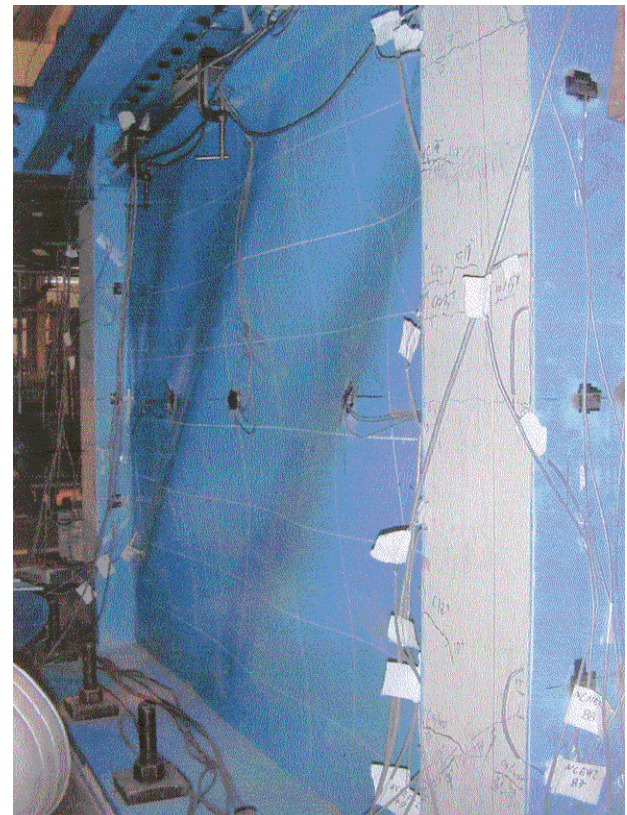
Fig. 10. Shear wall with partially composite columns (Courtesy of Professor Robert G. Driver).

Large scale tubular truss beams have been tested under constant amplitude fatigue loading. The trusses were 30 ft (9 m) long and 6 ft 8 in. (2 m) high, as shown in Figure 12. The truss members were circular hollow sections (CHS) in S355 steel (50 ksi yield stress). The truss itself was planar only, and the connections to be tested were all of the K-configuration. The primary aim was to evaluate the fatigue behavior of compression-loaded joints; specifically, where the chord is in compression, one diagonal is in compression and one diagonal is in tension.

As found in other studies, fatigue cracks developed in the compression joints as a result of the high tensile residual stress that was produced by the welding of the connection. The cracks started at the weld toe and their propagation was monitored by checking the alternating current potential drop. The residual stress measurements were made by hole drilling as well as neutron diffraction. Additional observations have been made regarding the crack initiation location,

the crack propagation speed, and the formation of additional (secondary) cracks. As expected, the final failure took place when the tension member cracked. Further tests and analyses are being conducted, with the aim of providing improved fatigue design criteria and fatigue life predictions (Acevedo and Nussbaumer, 2009).

UNIVERSITY OF LJUBLJANA

Bending-Shear Interaction in Plate Girders: This project has been conducted at the University of Ljubljana in Ljubljana, Slovenia, with Professor Darko Beg as the director.

Studies have shown that the interaction between bending and shear may not be significant. As a result, the design criteria of Eurocode 3 (EC3) appear to be very conservative (CEN, 2005). The key question is whether it is correct to use the same moment-shear interaction approach for longitudinally stiffened and unstiffened plate girders. A major parametric study was conducted to arrive at a realistic approach. At this stage it has been determined that the interaction is negligible for girders with high web slenderness; the opposite is correct for girders with low slenderness. Further, the EC3 criteria are shown to be safe for high slenderness girders; the opposite is true for girders with low slenderness. Figure 13 demonstrate these observations, with the left portion showing the results for girders with a web thickness of 6 mm (¼ in.) and the right portion for girders with a web thickness of 10 mm (⅜ in.). All of these girders had a web slenderness of 1,500. The flange *b/t* value was 300 with a thickness of 20 mm (¾ in.). The vertical stiffener spacing was 1,500 mm (5 ft). There was one longitudinal stiffener.

An extensive investigation is currently under way to determine the importance of web imperfections. The initial results show very limited influence in the context of moment-shear interaction.
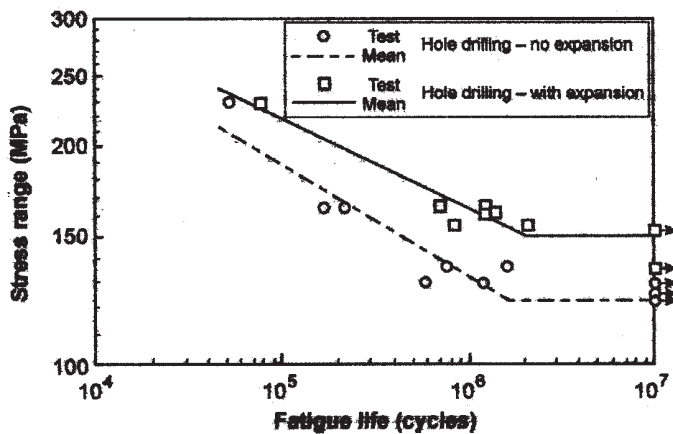

Fig. 11. Fatigue life test data for hole drilling with and without hole expansion (Courtesy of Professor Gilbert Y. Grondin).
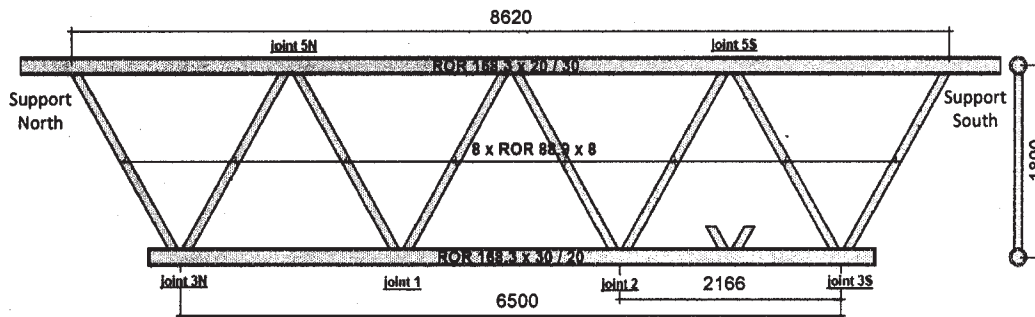

Fig. 12. Planar truss with circular hollow section members for fatigue testing of K-joints (Courtesy of Professor Alain Nussbaumer).

REFERENCES

Acevedo, C. and Nussbaumer, A. (2009), "Study on Crack Propagation in Tubular Joints under Compressive Fatigue Loadings," *Fatigue Design 2009*, Cetim, Senlis, France.

CEN (Comité Européen de Normalisation) (2005a), *Eurocode 3—Design of Steel Structures—EN 1993-1*, CEN, Brussels, Belgium.

Chicoine, T., Tremblay, R., Massicotte, B., Ricles, J.M. and Lu, L.-W. (2002), "Behavior and Strength of Partially-Encased Composite Columns with Built-Up Shapes," *Journal of Structural Engineering*, ASCE, Vol. 128, No. 3, pp. 279–288.

Dong, J. and Sause, R. (2009), "Flexural Strength of Tubular Flange Girders," *Journal of Constructional Steel Research*, Vol. 65, No. 3, pp. 622–630.

Dong, J. and Sause, R. (2010), "Finite Element Analysis of Curved Tubular Flange Girders," *Engineering Structures*, Vol. 32, No. 1, pp. 319–327.

Josi, Georg (2010), "Reliability-Based Management of Fatigue Failures," Ph.D. dissertation, Department of Civil Engineering, University of Alberta, Edmonton, Alberta, Canada.

Prickett, B.S. and Driver, R.G. (2006), "Behaviour of Partially Encased Composite Columns Made with High Performance Concrete," *Structural Engineering Report No. 262,* Department of Civil Engineering, University of Alberta, Edmonton, Alberta, Canada.

Ricles, J.M., Mao, C., Lu, L.-W. and Fisher, J.W. (2003), "Ductile Details for Welded Unreinforced Moment Connections Subject to Inelastic Cyclic Loading," *Engineering Structures*, Vol. 25, pp. 667–680.

Roke, D., Sause, R., Ricles, J.M. and Gonner, N. (2009), "Damage-Free Seismic-Resistant Self-Centering Steel Concentrically Braced Frames," in *STESSA 2009, 6th International Conference on Behavior of Steel Structures in Seismic Areas*, Philadelphia, Pennsylvania, August, pp. 3–10.

Sause, R., Ricles, J.M., Roke, D., Seo, C.-Y. and Lee, K.-S. (2006), "Self-Centering Seismic-Resistant Steel Concentrically Braced Frames," in *STESSA 2006, 5th International Conference on Behavior of Steel Structures in Seismic Areas*, Yokohama, Japan, August, pp. 85–90.

Zhang, X. and Ricles, J.M. (2006a), "Experimental Evaluation of Reduced Beam Section Connections to Deep Columns," *Journal of Structural Engineering*, ASCE, Vol. 132, No. 3, pp. 346–357.

Zhang, X. and Ricles, J.M. (2006b), "Seismic Behavior of Reduced Beam Section Moment Connections to Deep Columns," *Journal of Structural Engineering*, ASCE, Vol. 132, No. 3, pp. 358–367.
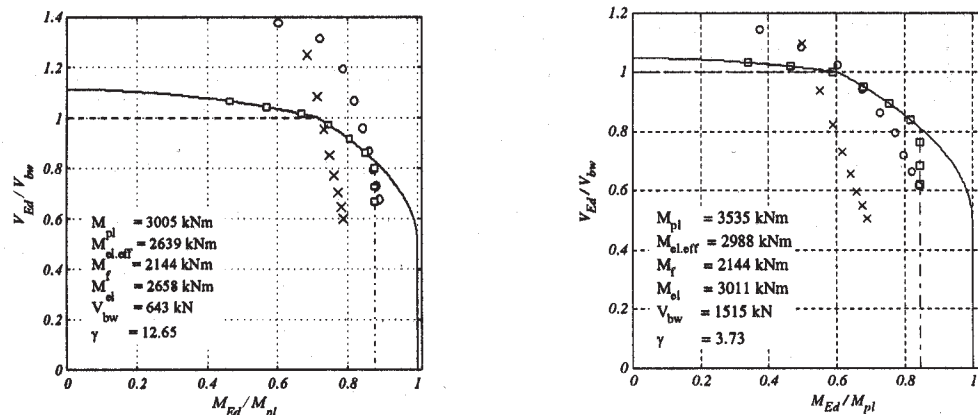
Fig. 13. Moment-shear interaction data for longitudinally stiffened plate girders (Courtesy of Professor Darko Beg).

DISCUSSION

Limit State Response of Composite Columns and Beam-Columns Part II: Application of Design Provisions for the 2005 AISC Specification

Paper by ROBERTO T. LEON and JEROME F. HAJJAR
(First Quarter, 2008)

Discussion by LOUIS F. GESCHWINDNER

The authors discuss the application of a set of equations for analysis and design of composite columns subjected to combined compression and bending. These equations were presented in the CD that accompanied the 13th edition *Steel Construction Manual* (AISC, 2005). The CD presents, in Figures I-1a through I-1d, sets of equations to be used to determine specific points on a simplified interaction diagram for encased W-shapes with bending about either the strong or the weak axes and filled rectangular and round HSS. These figures are used as the basis for Tables 2 through 5 in the paper. However, the authors have altered the figures from the CD for presentation in their paper.

The most significant difference between the authors' tables and the AISC figures occurs for the round HSS. The authors correctly point out a typographical error in Figure I-1d in the equation for θ where the terms $f'_c A_c$ should be removed. Clearly, if these variables were included in a calculation, the units, as well as the value, would be incorrect. The authors also point to "a discrepancy in the computation of Z_{sB}." However, the two equations that the authors provided for the plastic section modulus of the steel, Z_{sB}, appear to contain approximations that can be replaced with simple derivations that provide better accuracy. The paper does not include derivations for these equations.

In this discussion, three equations for use in determining Z_{sB} are developed and compared to those of the authors. The first equation is developed using the segment of a circle; the second, considered as a usable lower bound representation,

is developed using the sector of a circle; and the third solution is developed as an exact solution.

Figure 1 shows the geometry of a concrete-filled round HSS. The plastic neutral axis is shown in the location that would result if the member were to undergo pure bending. This is point B in Table 5 of the paper and this figure is similar to that shown for point B in Table 5. The development of the flexural strength of the composite member requires the determination of several different properties of portions of the steel and concrete. One is the plastic section modulus, Z_{sB}, of that portion of the steel beyond the plastic neutral axis on the compression side and the symmetrically placed steel section on the tension side. These areas are shown shaded in Figure 1. The different solutions for Z_{sB} result from different approaches to modeling these two areas.

CIRCULAR SEGMENT

Figure 2(a) shows the geometric properties of a circular segment. Using these properties, the moment of the area of this circular segment taken about the circle center is
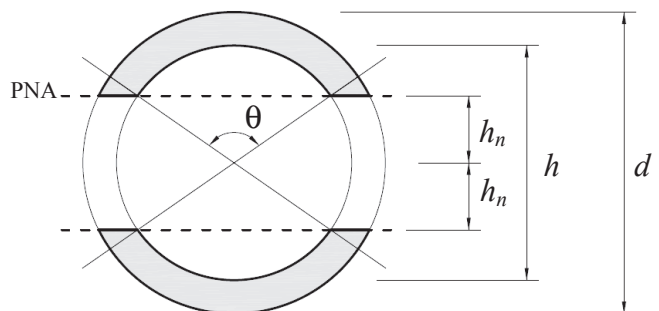

Fig. 1. Plastic neutral axis of concrete-filled round HSS in pure bending.

Louis F. Geschwindner, P.E., Ph.D., Vice President, American Institute of Steel Construction, 1 E. Wacker Dr., Suite 700, Chicago, IL 60601. E-mail: lfg@psu.edu

$$(\text{area})(\text{arm}) = \frac{r^2}{2}(\theta - \sin\theta)\left(\frac{4r}{3}\right)\left(\frac{\sin^3(\theta/2)}{(\theta-\sin\theta)}\right) \qquad (1)$$
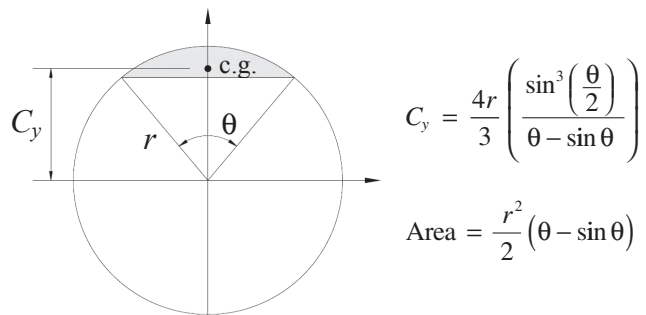
$$= \left(\frac{2r^3}{3}\right)\sin^3(\theta/2)$$

Using $R = d/2$, the plastic section modulus for the pair of circular segments in tension and compression is twice the moment of the area of one circular segment. Thus,

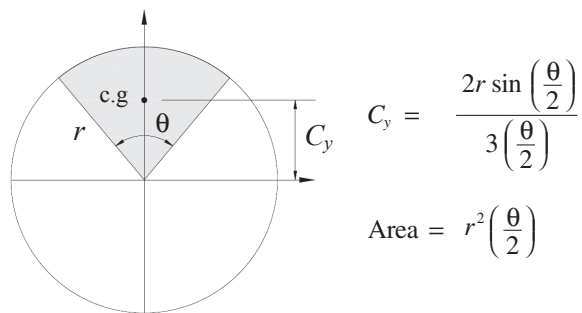$$Z_{\text{seg}} = 2\left(\frac{2(d/2)^3}{3}\right)\sin^3(\theta/2) = \frac{d^3}{6}\sin^3(\theta/2) \qquad (2)$$

Similarly, the plastic section modulus for the matching segments of concrete with diameter, h, is

$$Z_{cB} = \frac{h^3}{6}\sin^3(\theta/2) \qquad (3)$$

The plastic section modulus of the steel areas shown shaded in Figure 1, Z_{sB}, can then be determined as the plastic section modulus of the segment minus the plastic section modulus of the concrete. Thus,

$$Z_{sB} = Z_{\text{seg}} - Z_{cB} = \frac{\left(d^3 - h^3\right)}{6}\sin^3(\theta/2) \qquad (4)$$

Equation 4 is the equation given in AISC Figure I-1d. This is not an exact solution since the two circle segments are not properly aligned. Figure 3 shows the areas that are used to determine Z_{seg} and Z_{cB} and where they are located with respect to each other. It also shows the area of steel that should have been included but is not, $A_{s,\text{missing}}$, and the area of concrete that was subtracted that should not have been, $A_{c,\text{extra}}$. As the thickness of the steel section gets smaller or the angle, θ, approaches π, Equation 4 approaches the correct value.

CIRCULAR SECTOR

Figure 2(b) shows the geometric properties of a circular sector. The moment of the area of the circular sector about the circle center is

$$(\text{area})(\text{arm}) = r^2\left(\frac{\theta}{2}\right)\left(\frac{2r\sin(\theta/2)}{3(\theta/2)}\right) = \frac{2}{3}r^3\sin(\theta/2) \qquad (5)$$

Using $r = d/2$, the plastic section modulus for the pair of circular sectors in tension and compression is twice the moment of the area of one circular sector. Thus,

$$Z_{\text{sec}} = \frac{d^3}{6}\sin(\theta/2) \qquad (6)$$

Similarly, the plastic section modulus for the matching sectors of concrete with diameter, h, is

$$Z_{\text{conc}} = \frac{h^3}{6}\sin(\theta/2) \qquad (7)$$

(a) Circular segment

$$C_y = \frac{4r}{3}\left(\frac{\sin^3\left(\frac{\theta}{2}\right)}{\theta-\sin\theta}\right)$$

$$\text{Area} = \frac{r^2}{2}(\theta - \sin\theta)$$

(b) Circular sector

$$C_y = \frac{2r\sin\left(\frac{\theta}{2}\right)}{3\left(\frac{\theta}{2}\right)}$$

$$\text{Area} = r^2\left(\frac{\theta}{2}\right)$$
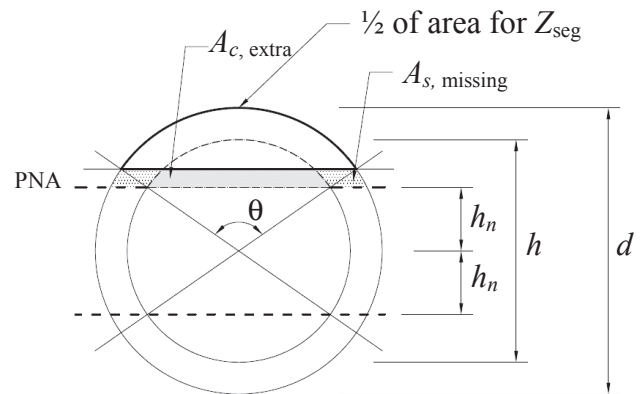
Fig. 2. Properties of a circle.

Fig. 3. Geometry for circular segment solution.

Subtracting the Z_{conc} from Z_{sec} will give the plastic section modulus of the steel. Thus,

$$Z_{sB} = \frac{\left(d^3 - h^3\right)}{6}\sin\left(\theta/2\right) \tag{8}$$

As was the case with the derivation of Equation 4, this is not an exact solution. Figure 4 shows the areas that are used to determine Z_{sec} and Z_{conc}. It also shows the area of steel that has not been included in the final calculation for Z_{sB}. Since the only approximation included in this derivation is the steel that has been ignored, this approach can be considered a "lower bound" solution.

EXACT SOLUTION

An exact solution is possible using the geometry of the circular segment and properly accounting for the two angles needed to describe the steel and concrete geometry. Figure 5(a) shows the concrete-filled round HSS with two circular segments defined by the angles, θ and θ_s. The angle, θ, is the same angle as defined for the earlier two derivations. The angle, θ_s, is the angle that defines the location of the plastic neutral axis at the outer face of the steel. Using the plastic section modulus as defined by Equation 2 and θ_s, yields

$$Z_{seg} = \frac{d^3}{6}\sin^3\left(\theta_s/2\right) \tag{9}$$

For the concrete segment, using Equation 2 and θ, yields

$$Z_{cB} = \frac{h^3}{6}\sin^3\left(\theta/2\right) \tag{10}$$

The exact plastic section modulus for the steel is then
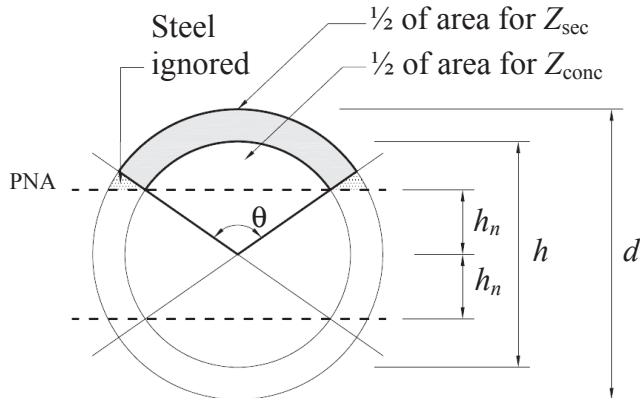
$$Z_{sB} = Z_{seg} - Z_{cB} \tag{11}$$

In order to combine Equations 9 and 10, the relationship between θ and θ_s is needed. From Figure 5(b), the following relationship is seen
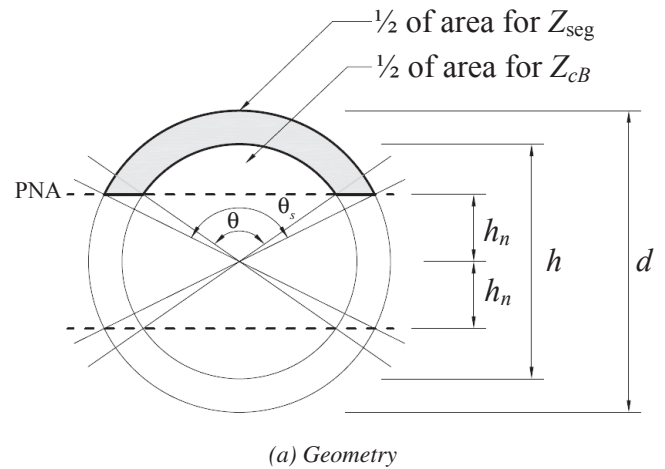
$$\frac{h}{2}\cos\left(\theta/2\right) = \frac{d}{2}\cos\left(\theta_s/2\right) \tag{12}$$

and combined with the basic trigonometric relationship, $\sin A = \sqrt{1 - \cos^2 A}$, yields

$$\sin\left(\theta_s/2\right) = \left(1 - \frac{h^2}{d^2}\cos^2\left(\theta/2\right)\right)^{1/2} \tag{13}$$

Substituting Equation 13 into Equation 9 yields

$$Z_{seg} = \frac{d^3}{6}\left(1 - \frac{h^2}{d^2}\cos^2\left(\theta/2\right)\right)^{3/2} \tag{14}$$

(a) Geometry

Fig. 4. Geometry for circular sector solution.

(b) Relationship between θ and θ_s

Fig. 5. Geometry for exact solution.

and substituting Equations 10 and 14 into Equation 11 yields

$$Z_{sB} = \frac{d^3}{6}\left(1 - \frac{h^2}{d^2}\cos^2\left(\theta/2\right)\right)^{3/2} - \frac{h^3}{6}\sin^3\left(\theta/2\right) \qquad (15)$$

Unlike the two previous derivations given for the circular segment and the circular sector, this derivation gives the exact solution for Z_{sB}.

AUTHORS' EQUATIONS

The two equations presented in the paper for Z_{sB} are:

a "correct" formulation

$$Z_{sB} = \left(\frac{d^3 - h^3}{12}\right)\sin^3\left(\theta/2\right)$$
$$\times\left[\frac{\theta}{\theta - \sin\theta} + \frac{\left(2\pi - \theta\right)}{\left(2\pi - \theta\right) - \sin\left(2\pi - \theta\right)}\right] \qquad (16)$$

and a simplified approximation

$$Z_{sB} \approx \frac{\left(d^3 - h^3\right)}{6}\sin^{4/3}\left(\theta/2\right) \qquad (17)$$

COMPARISON OF RESULTS

Five equations for the plastic section modulus of the steel for point B, pure bending, of a concrete-filled round HSS have been presented. The results from these five equations are plotted in Figure 6 for an HSS 16.000×0.250 over the full range of angle, θ, from 0 to π.

Equation 4, the original AISC equation, is the least accurate of the equations derived in this discussion. Equation 8,

the "lower bound" solution is closer to the exact solution than all of the other equations shown. The two equations presented by the authors, Equations 16 and 17, appear to be unrelated to those derived in this discussion. Although they give values closer to the exact solution than Equation 4, they do not provide a better solution than Equation 8, the "lower bound" solution. The origins of Equations 16 and 17 are not discussed in the paper.

The difference between Equations 8 and 15 is greatest for the lower values of θ. Thus, it would be helpful to know the approximate range of θ for realistic round HSS and acceptable values of concrete strengths. As concrete strength increases, the angle, θ, decreases. Thus, a check was made for all of the concrete filled round HSS listed in the Composite Column Tables of the 13th edition *Steel Construction Manual* (AISC, 2005b) but with a concrete strength, $f_c' = 10.0$ ksi. For these shapes, with $F_y = 42$ ksi, the HSS 16.000×0.250 required the smallest angle, $\theta = 1.77$ rad. As seen in Figure 6 for this shape, Equations 4, 8, 15, 16 and 17 give the following values for Z_{sB}:

Eq. No.	Model	Z_{sB} (in.^{3})
4	Circular segment	26.9
8	Circular sector	44.8
15	Exact	45.3
16	Paper "correct"	41.1
17	Paper simplified	41.2

In addition to using the Z_{sB} equations for determining moment strength for the pure bending case, the same basic formulation is used by the authors, with θ_2 to determine Z_{sE}, for moment strength at point E. The realistic range for θ_2 is π to 0 as points between C and somewhere close to A are determined. Thus, the error in not using Equation 15 with
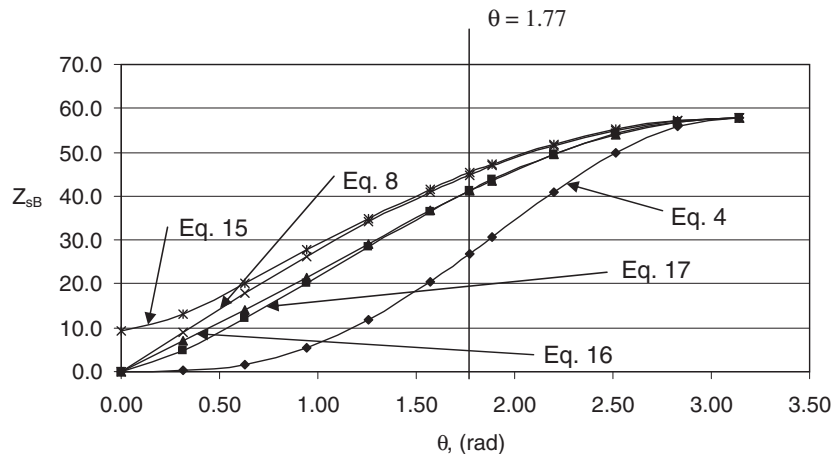

Fig. 6. Comparison of five equations for Z_{sB} for an HSS 16.000×0.250.

θ_2 for these points can be quite substantial. However, the lowest value of θ_2 for point E as defined by the authors for the HSS 16.000×0.250 discussed earlier is 1.23 rad and the error in computing Z_{sE} using the "lower bound" equation is approximately 5%.

RECOMMENDATIONS

Based on the derivations presented in this discussion, it is recommended that either the exact solution, Equation 15, or the circular sector solution, Equation 8, be used in calculations for pure bending, Point B, for a concrete-filled round HSS. Considering the simplicity of the latter and its ability to closely represent the correct value for Z_{sB}, it is further recommended that Equation 8 be adopted for use in place of the currently listed equation in Figure I-1d of the 13th edition companion CD.

In the rare case where point E is to be determined, it is recommended that the lower bound equation, Equation 8 with θ_2, be used. If more points on the interaction curve are to be determined, the exact solution, Equation 15, should be used.

In addition, revised versions of Figures I-1a through I-1d from the CD Companion V.13.0 are presented as Tables A through D of this Discussion. Note that Tables A through D also correspond to Figures 2 through 5 of the Leon and Hajjar paper, but with corrections.
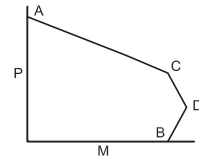
In summary the revisions incorporated are:

1. No changes to Figure I-1a (Table A).
2. Two editorial changes in Figure I-1b (Table B).
3. Several editorial changes and the inclusion of equations for point E in Figure I-1c (Table C).
4. Several editorial changes, the inclusion of equations for point E, and updated equations for Z_{sB} and Z_{sE} in Figure I-1d (Table D).

REFERENCE

AISC (2005), *Steel Construction Manual,* 13th Edition, American Institute of Steel Construction, Chicago, IL.
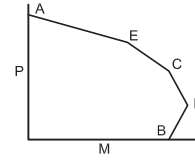
Editor's Note: AISC's Committee on Manuals and Textbooks has decided to incorporate Dr. Geschwindner's recommendations in revisions that will be made with the 14th edition AISC Steel Construction Manual.

Table A.
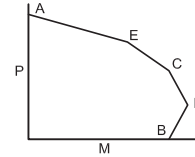## Plastic Capacities for Rectangular, Encased W-Shapes Bent About the X-X Axis

Section	Stress Distribution	Point	Defining Equations
(A)	$0.85f'_c$ F_y F_{yr}	A	$P_A = A_s F_y + A_{sr} F_{yr} + 0.85 f'_c A_c$ $M_A = 0$ A_s = area of steel shape A_{sr} = area of all continuous reinforcing bars $A_c = h_1 h_2 - A_s - A_{sr}$
(C)		C	$P_C = 0.85 f'_c A_c$ $M_C = M_B$
(D)		D	$P_D = \dfrac{0.85 f'_c A_c}{2}$ $M_D = Z_s F_y + Z_r F_{yr} + \dfrac{Z_c}{2}\left(0.85 f'_c\right)$ Z_s = full x-axis plastic section modulus of steel shape A_{srs} = area of continuous reinforcing bars at the centerline $Z_r = \left(A_{sr} - A_{srs}\right)\left(\dfrac{h_2}{2} - c\right)$ $Z_c = \dfrac{h_1 h_2^2}{4} - Z_s - Z_r$
(B)		B	$P_B = 0$ $M_B = M_D - Z_{sn} F_y - \tfrac{1}{2} Z_{cn}\left(0.85 f'_c\right)$ $Z_{cn} = h_1 h_n^2 - Z_{sn}$ For h_n below the flange $\left(h_n \le \dfrac{d}{2} - t_f\right)$ $h_n = \dfrac{0.85 f'_c\left(A_c + A_{srs}\right) - 2 F_{yr} A_{srs}}{2\left[0.85 f'_c\left(h_1 - t_w\right) + 2 F_y t_w\right]}$ $Z_{sn} = t_w h_n^2$ For h_n within the flange $\left(\dfrac{d}{2} - t_f < h_n \le \dfrac{d}{2}\right)$ $h_n = \dfrac{0.85 f'_c\left(A_c + A_s - d b_f + A_{srs}\right) - 2 F_y\left(A_s - d b_f\right) - 2 F_{yr} A_{srs}}{2\left[0.85 f'_c\left(h_1 - b_f\right) + 2 F_y b_f\right]}$ $Z_{sn} = Z_s - b_f\left(\dfrac{d}{2} - h_n\right)\left(\dfrac{d}{2} + h_n\right)$ For h_n above the flange $\left(d_n > \dfrac{d}{2}\right)$ $h_n = \dfrac{0.85 f'_c\left(A_c + A_s + A_{srs}\right) - 2 F_y A_s - 2 F_{yr} A_{srs}}{2\left(0.85 f'_c h_1\right)}$ $Z_{sn} = Z_{sx}$ = full x-axis plastic section modulus of steel shape

Table B.
Plastic Capacities for Rectangular, Encased W-Shapes Bent About the Y-Y Axis

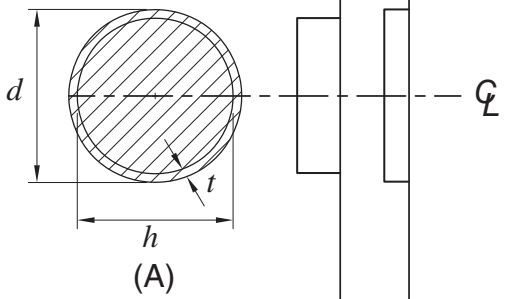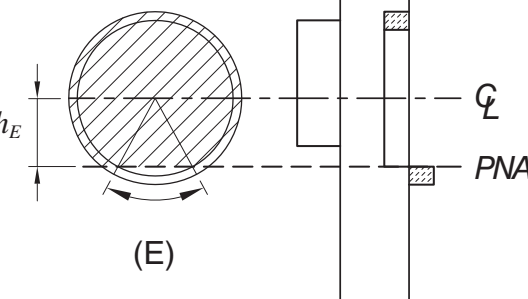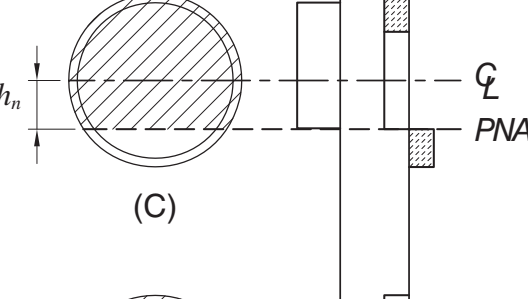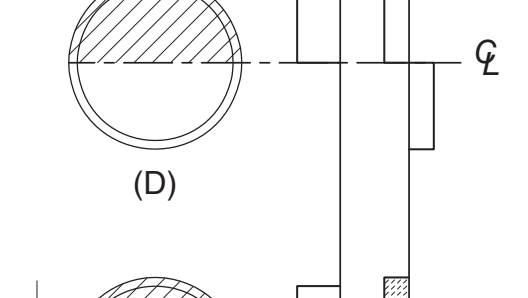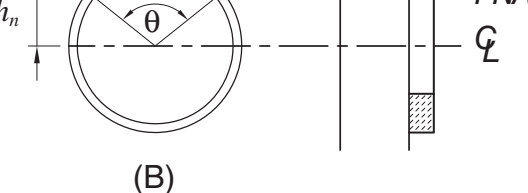| Section	Stress Distribution	Point	Defining Equations
(A)	$0.85f'_c$ F_y F_{yr}	A	$P_A = A_sF_y + A_{sr}F_{yr} + 0.85f'_cA_c$ $M_A = 0$ A_s = area of steel shape A_{sr} = area of continuous reinforcing bars $A_c = h_1h_2 - A_s - A_{sr}$
		E	$P_E = A_sF_y + (0.85f'_c)\left[A_c - \dfrac{h_1}{2}(h_2 - b_f) + \dfrac{A_{sr}}{2}\right]$ $M_E = M_D - Z_{sE}F_y - \frac{1}{2}Z_{cE}(0.85f'_c)$ $Z_{sE} = Z_{sy}$ = full y-axis plastic section modulus of steel shape $Z_{cE} = \dfrac{h_1b_f^2}{4} - Z_{sE}$
(E)		C	$P_C = 0.85f'_cA_c$ $M_C = M_B$
		D	$P_D = \dfrac{0.85f'_cA_c}{2}$ $M_D = Z_sF_y + Z_rF_{sr} + \frac{1}{2}Z_c(0.85f'_c)$ Z_s = full y-axis plastic section modulus of steel shape $Z_r = A_{sr}\left(\dfrac{h_2}{2} - c\right)$ $Z_c = \dfrac{h_1h_2^2}{4} - Z_s - Z_r$
(C) (D) (B)		B	$P_B = 0$ $M_B = M_D - Z_{sn}F_y - \frac{1}{2}Z_{cn}(0.85f'_c)$ $Z_{cn} = h_1h_n^2 - Z_{sn}$ For h_n below the flange $\left(\dfrac{t_w}{2} < h_n \le \dfrac{b_f}{2}\right)$ $h_n = \dfrac{0.85f'_c(A_c + A_s - 2t_fb_f) - 2F_y(A_s - 2t_fb_f)}{2\left[4t_fF_y + (h_1 - 2t_f)0.85f'_c\right]}$ $Z_{sn} = Z_s - 2t_f\left(\dfrac{b_f}{2} + h_n\right)\left(\dfrac{b_f}{2} - h_n\right)$ For h_n above the flange $\left(h_n > \dfrac{b_f}{2}\right)$ $h_n = \dfrac{0.85f'_c(A_c + A_s) - 2F_yA_s}{2\left[0.85f'_ch_1\right]}$ $Z_{sn} = Z_{sy}$ = full y-axis plastic section modulus of steel shape

Table C.
Plastic Capacities for Composite, Filled HSS
Bent About the X-X Axis

Section	Stress Distribution	Point	Defining Equations
(A)	$0.85f'_c$ F_y	A	$P_A = F_y A_s + 0.85 f'_c A_c$ $M_A = 0$ A_s = area of steel shape $A_c = h_1 h_2 - 0.858 r_i^2$ $h_1 = b - 2t$ $h_2 = d - 2t$
(E)		E	$P_E = \frac{1}{2}\left(0.85 f'_c A_c\right) + 0.85 f'_c h_1 h_E + 4F_y t h_E$ $M_E = M_D - F_y Z_{sE} - \frac{1}{2}\left(0.85 f'_c Z_{cE}\right)$ $Z_{cE} = h_1 h_E^2$ $Z_{sE} = 2t h_E^2$ $h_E = \dfrac{h_n}{2} + \dfrac{d}{4}$
(C)		C	$P_C = 0.85 f'_c A_c$ $M_C = M_B$
(D)		D	$P_D = \dfrac{0.85 f'_c A_c}{2}$ $M_D = F_y Z_s + \frac{1}{2}\left(0.85 f'_c Z_c\right)$ Z_s = full x-axis plastic section modulus of HSS $Z_c = \dfrac{h_1 h_2^2}{4} - 0.192 r_i^3$
(B)		B	$P_B = 0$ $M_B = M_D - F_y Z_{sn} - \frac{1}{2}\left(0.85 f'_c Z_{cn}\right)$ $Z_{sn} = 2t h_n^2$ $Z_{cn} = h_1 h_n^2$ $h_n = \dfrac{0.85 f'_c A_c}{2\left[0.85 f'_c h_1 + 4t F_y\right]} \le \dfrac{h_2}{2}$

Table D.
Plastic Capacities for Composite, Filled Round HSS
Bent About Any Axis

Section	Stress Distribution	Point	Defining Equations
d, t, h **(A)**	$0.95f'_c$ F_y $\mathsf{\displaystyle\frac{C}{L}}$	A	$P_A = F_y A_s + 0.95 f'_c A_c \,*$ $M_A = 0$ $A_s = \pi(dt - t^2)$ $A_c = \dfrac{\pi h^2}{4}$
h_E **(E)** $\mathsf{\frac{C}{L}}$ PNA		E	$P_E = P_A - \frac{1}{4}\left[F_y\left(d^2 - h^2\right) + \frac{1}{2}\left(0.95 f'_c\right)h^2 \right]\left(\theta_2 - \sin\theta_2\right)$ $M_E = F_y Z_{sE} + \frac{1}{2}\left(0.95 f'_c Z_{cE}\right)$ $Z_{cE} = \dfrac{h^3}{6}\sin^3\!\left(\dfrac{\theta_2}{2}\right)$ $Z_{sE} = \dfrac{\left(d^3 - h^3\right)}{6}\sin\!\left(\dfrac{\theta_2}{2}\right)$ $h_E = \dfrac{h_n}{2} + \dfrac{h}{4}$ $\theta_2 = \pi - 2\arcsin\!\left(\dfrac{2h_E}{h}\right)$
h_n **(C)** $\mathsf{\frac{C}{L}}$ PNA		C	$P_C = 0.95 f'_c A_c$ $M_C = M_B$
(D) $\mathsf{\frac{C}{L}}$		D	$P_D = \dfrac{0.95 f'_c A_c}{2}$ $M_D = F_y Z_s + \frac{1}{2}\left(0.95 f'_c Z_c\right)$ $Z_s = \text{plastic section modulus of steel shape} = \dfrac{d^3}{6} - Z_c$ $Z_c = \dfrac{h^3}{6}$
h_n, θ **(B)** PNA $\mathsf{\frac{C}{L}}$		B	$P_B = 0$ $M_B = F_y Z_{sB} + \frac{1}{2}\left(0.95 f'_c Z_{cB}\right)$ $Z_{sB} = \dfrac{\left(d^3 - h^3\right)}{6}\sin\!\left(\dfrac{\theta}{2}\right)$ $Z_{cB} = \dfrac{h^3 \sin^3\!\left(\dfrac{\theta}{2}\right)}{6}$ $\theta = \dfrac{0.0260 K_c - 2K_s}{0.0848 K_c}$ $\quad + \dfrac{\sqrt{\left(0.0260 K_c + 2K_s\right)^2 + 0.857 K_c K_s}}{0.0848 K_c}$ (rad) $K_c = f'_c h^2$ $K_s = F_y\left(\dfrac{d-t}{2}\right)t$ ("thin" HSS wall assumed) $h_n = \dfrac{h}{2}\sin\!\left(\dfrac{\pi - \theta}{2}\right) \le \dfrac{h}{2}$

*$0.95f'_c$ may be used for concrete filled round HSS.

CLOSURE

Limit State Response of Composite Columns and Beam-Columns Part II: Application of Design Provisions for the 2005 AISC Specification

Paper by ROBERTO T. LEON and JEROME F. HAJJAR

Closure by ROBERTO T. LEON, TIZIANO PEREA and JEROME F. HAJJAR

The authors thank Dr. Geschwindner for his comments on the derivation of the plastic section modulus, Z_s, of circular HSS as shown in Table 5 of the original paper. (Equation numbers referenced in this Closure are the same as those used in the Discussion, for clarity.)

The derivation of Equation 16 of the Discussion was omitted from the original paper for brevity. It is shown in the attached Appendix. Equation 17 was intended as a straightforward lower-bound curve fit to Equation 16; many similar expressions are possible. The primary assumption that was made in Equation 16 is that the wall of the circular HSS is assumed to be thin (i.e., that $\theta \approx \theta_s$ using the nomenclature of the Discussion). As noted by Dr. Geschwindner, this assumption results in the area of the steel being underestimated and that for the concrete being overestimated.

The authors appreciate Dr. Geschwindner's efforts in developing new exact and approximate equations for Z_s, represented by Equations 15 and 8, respectively, in the Discussion. The authors agree that his equations are applicable to thick-walled circular CFTs ($\theta \neq \theta_s$) and provide results with better accuracy than those stated in the original paper.

The authors agree that Equation 8 in the Discussion is a reasonable replacement for both the original equation for Z_{sB} in Table I-1d on the CD companion to the 13th edition

AISC *Manual* (Equation 4 in the Discussion) and the proposed equation for Z_{sB} in our original paper (Equation 17 in the Discussion). Finally, the authors will like to note that Equation 8 is the same as those given by the Architectural Institute of Japan (AIJ) in their provisions for composite members once a number of geometric transformations are made.

APPENDIX

Derivation of the Plastic Section Modulus of a Circular HSS Thin Tube (Equation 16 in the Discussion)

This appendix derives the equation to get the plastic section modulus (Z_s) of a circular HSS stated in Table 5 in the original paper (Equation 15 in this appendix). The derivation assumes a thin-walled HSS cross section as shown in Figure A.1b.

The area and the centroidal distance of a circular segment (Figure A.1a) including both concrete and steel sections are given by:
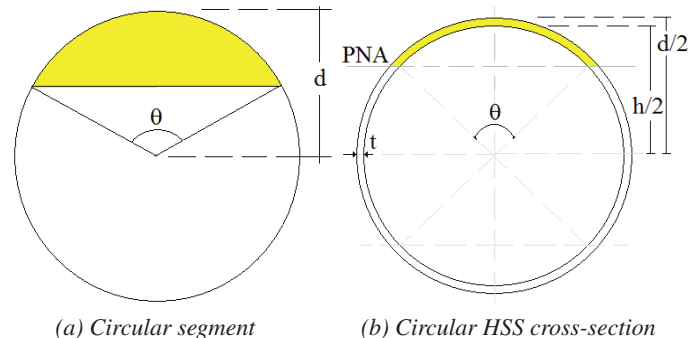

(a) Circular segment   *(b) Circular HSS cross-section*

Fig. A.1. Variables used in the derivation.

Roberto T. Leon, Professor, School of Civil and Environmental Engineering, 790 Atlantic Dr., Georgia Institute of Technology, Atlanta, GA 30332, corresponding author. E-mail: rl58@ce.gatech.edu

Tiziano Perea, Graduate Research Assistant, School of Civil and Environmental Engineering, 790 Atlantic Dr., Georgia Institute of Technology, Atlanta, GA 30332. E-mail: tperea@gatech.edu

Jerome F. Hajjar, Professor and Chair, Department of Civil and Environmental Engineering, 400 Snell Engineering Center, 360 Huntington Ave., Northeastern University, Boston, MA 02115. E-mail: jf.hajjar@neu.edu

$$A_d = \frac{d^2}{8}\left(\theta - \sin\theta\right) \tag{A.1}$$

$$Y_d = \frac{2d \sin^3\left(\theta/2\right)}{3\left(\theta - \sin\theta\right)} \tag{A.2}$$

Note in Figure A.1 that the angle θ in (a) is not the same as the angle θ in (b). This difference is small for thin-walled sections. Assuming the steel wall is thin enough that the difference can be neglected, the area and centroidal distance of the circular segment in the concrete only can be approximated as:

$$A_h = \frac{h^2}{8}\left(\theta - \sin\theta\right) \tag{A.3}$$

$$Y_h = \frac{2h \sin^3\left(\theta/2\right)}{3\left(\theta - \sin\theta\right)} \tag{A.4}$$

Thus, the area and the first moment of the area of the shaded ring segment in Figure A.1b are as follows:

$$A_r = A_d - A_h \tag{A.5}$$

$$Q_r = A_d Y_d - A_h Y_h \tag{A.6}$$

Then, the centroidal distance of a ring segment (i.e., only the steel) is given by:

$$Y_r = \frac{Q_r}{A_r} = \frac{2\left(d^3 - h^3\right)\sin^3\left(\theta/2\right)}{3\left(d^2 - h^2\right)\left(\theta - \sin\theta\right)} \tag{A.7}$$

The last equation can be adjusted for the complement ring segment when θ is changed by $2\pi - \theta$. Thus:

$$Y_r = \frac{Q_r}{A_r} = \frac{2\left(d^3 - h^3\right)\sin^3\left(\theta/2\right)}{3\left(d^2 - h^2\right)\left(2\pi - \theta + \sin\theta\right)} \tag{A.8}$$

The compression and tension forces on the steel ring segments, their respective centroidal distances, and the total bending moment are given by the following equations.

For the compression zone defined by the angle θ, where $r_m = (d - t)/2$ and $t = (d - h)/2$:

$$C_s = 2\pi r_m t\left(\frac{\theta}{2\pi}\right)F_y = \left(\frac{d - t}{2}\right)\left(t\right)\left(\theta\right)F_y$$
$$= \frac{\left(d^2 - h^2\right)\left(\theta\right)F_y}{8} \tag{A.9}$$

$$Y_{cs} = \frac{2\left(d^3 - h^3\right)\sin^3\left(\theta/2\right)}{3\left(d^2 - h^2\right)\left(\theta - \sin\theta\right)} \tag{A.10}$$

For the tension zone defined by the complement of the angle θ, where $r_m = (d - t)/2$ and $t = (d - h)/2$:

$$T_s = \left(\frac{d - t}{2}\right)\left(t\right)\left(2\pi - \theta\right)F_y = \frac{\left(d^2 - h^2\right)\left(2\pi - \theta\right)F_y}{8} \tag{A.11}$$

$$Y_{ts} = \frac{2\left(d^3 - h^3\right)\sin^3\left(\theta/2\right)}{3\left(d^2 - h^2\right)\left(2\pi - \theta + \sin\theta\right)} \tag{A.12}$$

Then, the nominal moments in the steel cross section can be summed as:

$$C_s Y_{cs} + T_s Y_{ts} = F_y Z_{s\theta} \tag{A.13}$$

From Equation A.13, the plastic modulus of the steel cross-section for any angle theta is given by:

$$Z_{s\theta} = \frac{\theta\left(d^3 - h^3\right)\sin^3\left(\theta/2\right)}{12\left(\theta - \sin\theta\right)}$$
$$+ \frac{\left(2\pi - \theta\right)\left(d^3 - h^3\right)\sin^3\left(\theta/2\right)}{12\left(2\pi - \theta + \sin\theta\right)} \tag{A.14}$$

In the denominator of the second term of Equation A.14, the $\sin(\theta)$ term may be taken as its trigonometric equivalent, $-\sin(2\pi - \theta)$. With all like terms based upon the same angle, $2\pi - \theta$, Equation A.14 can be restated as:

$$Z_{s\theta} = \frac{\left(d^3 - h^3\right)\sin^3\left(\theta/2\right)}{12}$$
$$\times \left[\frac{\theta}{\left(\theta - \sin\theta\right)} + \frac{\left(2\pi - \theta\right)}{\left(2\pi - \theta\right) - \sin\left(2\pi - \theta\right)}\right] \tag{A.15}$$

Equation A.15 is the one shown in Table 5 (Point B) in the original paper to get the plastic section modulus (Z_s) of a circular HSS.

GUIDE FOR AUTHORS

SCOPE: The ENGINEERING JOURNAL is dedicated to the improvement and advancement of steel construction. Its pages are open to all who wish to report on new developments or techniques in steel design, research, the design and/or construction of new projects, steel fabrication methods, or new products of significance to the uses of steel in construction. Only original papers should be submitted.

GENERAL: Papers intended for publication may be submitted by mail to the Editor, Keith Grubb, ENGINEERING JOURNAL, AMERICAN INSTITUTE OF STEEL CONSTRUCTION, One East Wacker Drive, Suite 700, Chicago, IL, 60601, or by email to grubb@aisc.org.

The articles published in the *Engineering Journal* undergo peer review before publication for (1) originality of contribution; (2) technical value to the steel construction community; (3) proper credit to others working in the same area; (4) prior publication of the material; and (5) justification of the conclusion based on the report.

All papers within the scope outlined above will be reviewed by engineers selected from among AISC, industry, design firms, and universities. The standard review process includes outside review by an average of three reviewers, who are experts in their respective technical area, and volunteers in the program. Papers not accepted will not be returned to the author. Published papers become the property of the American Institute of Steel Construction and are protected by appropriate copyrights. No proofs will be sent to authors. Each author receives three copies of the issue in which his contribution appears.

MANUSCRIPT PREPARATION: Manuscripts must be provided in Microsoft Word 2003 format. A laser-quality proof or high quality PDF must accompany your submittal. Download our complete author guidelines at **www.aisc.org/ej**.

There's always a solution in steel.